PET/MRT in der onkologischen Diagnostik

mit dem Schwerpunkt Kopf-Hals-Tumoren

Der Medizinischen Fakultät

der Universität Leipzig

eingereichte

H A B I L I T A T I O N S S C H R I F T

zur Erlangung des akademischen Grades

Doctor medicinae habilitatus

(Dr. med. habil.)

vorgelegt

von Dr. med. Patrick Stumpp, MME

geboren am 31.08.1973 in Ravensburg.

Leipzig, den 01.06.2016

Beschluss der Verleihung vom 22.11.2016.

Für Laura

Bibliographische Beschreibung:

Stumpp, Patrick

PET/MRT in der onkologischen Diagnostik mit dem Schwerpunkt Kopf-Hals-Tumoren

Universität Leipzig, Habilitation

105 Seiten inklusive 6 Originalarbeiten, 143 Literaturstellen, 3 Abbildungen, 2 Tabellen

Referat:

Erst seit 2010 sind kombinierte Positronenemissionstomographie-Magnetresonanztomographie-Geräte (PET/MRT) zur hybriden Bildgebung verfügbar. Die mit der Entwicklung der Geräte verbundenen Hoffnungen bezüglich der onkologischen Diagnostik lagen zunächst auf einer verbesserten Genauigkeit in der Tumordetektion im Vergleich zur PET/CT. Rasch wurde jedoch deutlich, dass insbesondere die Möglichkeit der non-invasiven, multiparametrischen Charakterisierung von Tumorerkrankungen einen wesentlichen Vorteil der PET/MRT gegenüber der PET/CT darstellt.

Der im Universitätsklinikum Leipzig AöR 2011 installierte PET/MRT-Scanner war einer der ersten weltweit und in dieser Habilitationsschrift sind die ersten Erfahrungen mit dieser Methode auf dem Gebiet der onkologischen Diagnostik zusammengefasst. Schwerpunkt ist dabei die Diagnostik von Kopf-Hals-Tumoren, da in diesem Bereich die CT aufgrund des im Vergleich zur MRT schlechteren Weichteilkontrastes Einschränkungen aufweist.

In dieser Schrift werden zunächst die unterschiedlichen Konzepte im Gerätedesign der PET/MRT und die Besonderheiten der PET/MRT im Vergleich zur PET/CT erläutert. Auch die kritischen Punkte, die bei der Implementierung eines PET/MRT-Scanners zu beachten sind, werden detailliert dargestellt. Hierbei werden besonders die baulichen und organisatorischen Aspekte berücksichtigt, es werden aber auch Hinweise zur Qualitätskontrolle und zur Entwicklung von Untersuchungsprotokollen gegeben.

In der ersten klinischen Studie zur Anwendung der PET/MRT mit 18F-Fluorodesoxyglucose (18F-FDG) bei Patienten mit Kopf-Hals-Tumoren konnten wir hinsichtlich Sensitivität und Spezifität noch keine Unterschiede zur PET/CT nachweisen. Allerdings war hier die untersuchte Patientengruppe heterogen und enthielt sowohl Primär- als auch Rezidivtumore.

Aktuell konzentriert sich die onkologische Forschung am PET/MRT auf die Möglichkeiten der multiparametrischen Bildgebung zur Detektion und vor allem Charakterisierung von Tumorerkrankungen. Hier konnten wir signifikante Korrelationen von Glukosestoffwechsel und verschiedenen Perfusionsparametern bei Patienten mit Kopf-Hals-Tumoren nachweisen. Bei Patientinnen mit Zervixkarzinom konnte ein inverser Zusammenhang zwischen Glukosestoffwechsel und Diffusionsrestriktion nachgewiesen werden. Die letzte aufgeführte Arbeit zeigt die Korrelationen zwischen der bildgebenden Tumorcharakterisierung und histopathologischen Ergebnissen bei Kopf-Hals-Tumoren, wo wir Zusammenhänge von Kernfläche und dem Proliferationsmarker Ki-67 mit Diffusionseigenschaften bzw. Glukosestoffwechsel im Tumorgewebe nachweisen konnten.

Inhalt

Abbildungsverzeichnis

Abkürzungsverzeichnis

ADC - apparent diffusion coefficient (scheinbarer Diffusionskoeffizient)
APD - Avalanche Photo Dioden
CE - Contrast-Enhanced (kontrastverstärkt)
CT- Computertomographie
CUP - cancer of unknown primary (Karzinom unbekannten Primums)
DCE-MRT - dynamic contrast-enhanced MRI (dynamische kontrastverstärkte MRT)
DOTA - Tetraazacyclododecantetraessigsäure
DFG - Deutsche Forschungsgemeinschaft
DWI - diffusion weighted imaging (diffusionsgewichtete Bildgebung)
EPI - echoplanar imaging (echoplanare Bildgebung)
18F-FDG - 18Fluor-Fluorodesoxyglucose
FLASH - fast low angle shot (spezielle T1-Gradientenechosequenz)
Gd-EOB-DTPA - Gadolinium-Ethoxybenzyl-Diethylentriamin-Pentaazetatsäure
HASTE - half-fourier acquisition single-shot turbo spin echo (spezielle T2-Sequenz)
HNO - Hals-Nasen-Ohrenheilkunde
kV - Kilovolt
MR - Magnetresonanz
MRT - Magnetresonanztomographie
mSv - Millisievert
PET - Positronenemissionstomographie
PET/CT - Positronenemissionstomographie/Computertomographie
PET/MRT - Positronenemissionstomographie/Magnetresonanztomographie
PIRADS - prostate imaging reporting and data system (standardisiertes System zur Bewertung von multiparametrischen MRT-Untersuchungen der Prostata)
PSMA - prostataspezifisches Membranantigen
SUV - standardized uptake value (standardisierter Aufnahmewert)
TA - Akquisitionszeit
TE - Echozeit
TIRM - Turbo Inversion Recovery Magnitude
TR - Repetitionszeit
TSE - Turbo Spin Echo

1. Einführung in die Thematik

1.1. Entwicklung der hybriden Bildgebung

Hybride Bildgebungssysteme wurden im Jahr 1998 eingeführt, als die Positronenemissionstomographie (PET) mit der Computertomographie (CT) zur PET/CT verbunden wurde. Diese Kombination brachte insbesondere in der onkologischen Bildgebung deutliche Fortschritte. Auch wenn in Deutschland derzeit im Wesentlichen nur zwei Indikationsspektren von den Krankenkassen anerkannt und vergütet werden [1], so ist diese Methode doch bei zahlreichen Tumorerkrankungen von großem diagnostischem Nutzen. Bei den beiden aktuell von der gesetzlichen Krankenversicherung bezahlten Indikationen handelt es sich einerseits um Lungentumore (u.a. zum Staging des Bronchialkarzinoms oder zur Abklärung von Lungenrundherden) und andererseits um die Detektion von Vitalität bei CT-morphologischen Restbefunden nach Therapie des Hodgkin-Lymphoms [2]. Doch auch beim kolorektalen Karzinom, Ösophaguskarzinom, Mammakarzinom, malignen Melanom, Kopf-Hals-Tumor, cancer of unknown primary (CUP), Ovarialkarzinom, neuroendokrinen Tumor, muskuloskelettalen Tumor und nicht zuletzt beim Prostatakarzinom ist die PET/CT unter Verwendung verschiedener Tracer von großem Nutzen bei Tumordetektion und –staging [3–19].

Der große Benefit der PET/CT gegenüber der alleinigen CT-Diagnostik ist der Nachweis biochemischer Auffälligkeiten bei verschiedenen Tumorarten durch die PET (meist im Sinne der Detektion von erhöhtem Glukosestoffwechsel) in Verbindung mit der exakten anatomischen Zuordnung dieser Auffälligkeiten in der CT. Schon bald wurden jedoch auch Schwächen in diesem System deutlich, insbesondere in anatomischen Bereichen, in denen die CT aufgrund von geringen Kontrasten oder Bewegungs- bzw. Aufhärtungsartefakten Schwierigkeiten in der Darstellung hat, so z.B. im Hirnparenchym, bei Kopf-Hals-Tumoren, bei Leberherden und an Organen im Bereich des kleinen Beckens. Teilweise können diese Schwächen schon durch eine nachträgliche Bildfusion mit separat akquirierten MRT-Daten überwunden werden [20–27], jedoch ist dabei die Problematik der unterschiedlichen Patientenpositionierung in den beiden separat akquirierten Datensätzen zu beachten. Eine solche post-hoc Bildfusion ist für intrakranielle Strukturen aufgrund der festen Begrenzung durch den Hirnschädel relativ einfach durchzuführen. Für atembewegliche Organe und

Regionen, in denen Lageänderungen eine große Rolle spielen (wie z.B. in der Halsregion), ist diese nachträgliche Fusion schon deutlich erschwert.

Vor diesem Hintergrund wurde bald postuliert, dass eine Verbindung der Magnetresonanztomographie (MRT) mit der PET weitere diagnostische Fortschritte bringen könnte [28–32]. Brendle et al. konnten 2013 an einem der ersten simultanen PET/MRT-Systeme zeigen, dass eine simultane Datenakquisition Vorteile hinsichtlich der Genauigkeit der Bildfusion gegenüber der retrospektiven Fusion aufweist [33].

Vor der Einführung von Ganzkörper-PET/MRT-Systemen wurde jedoch zunächst im Jahr 2006 ein PET-Insert vorgestellt, das innerhalb eines 3T-MRT positioniert werden konnte und eine kombinierte, simultane PET/MRT-Diagnostik des Gehirns und der oberen Halsregion erlaubte [34–36]. Ab 2010 wurden dann kombinierte Ganzkörpersysteme angeboten, wobei die drei Marktführer unterschiedliche Wege in der Realisierung gingen, welche im folgenden Kapitel kurz dargestellt werden.

1.2. Technische Konzepte zur Kombination von PET und MRT

Grundsätzlich sind große technische Herausforderungen bei der Konstruktion eines integrierten PET/MRT-Gerätes zu bewältigen, da in einem Gehäuse PET- und MR-Technik kombiniert werden müssen. Einerseits dürfen die zusätzlich im MRT eingebrachten Bauteile des PET-Systems nicht das Magnetfeld bzw. die Gradientenfelder stören, weil dadurch Bildartefakte in den MRT-Bildern entstehen würden. Andererseits ist sicherzustellen, dass das starke B0-Feld des MRT, die während der Sequenzen eingestrahlten Hochfrequenzsignale und die zur Bildgebung nötigen Oberflächenspulen keine Effekte auf die Detektion und Verarbeitung des PET-Signals haben. In der Entwicklung der PET/MRT-Systeme wurden verschiedene Konzepte getestet [37–40]. Die wichtigsten Charakteristika werden hier noch einmal kurz zusammengefasst.

1.2.1. Separate Geräte – räumlich getrennt

Der Medizintechnikhersteller General Electrics entwickelte initial eine am PET/CT- und am MRT-Gerät ankoppelbare Patientenliege, auf welcher der Patient einmalig positioniert wird, um dann nacheinander an zwei separaten Geräten in zwei getrennten Räumen untersucht werden zu können. Dieses Vorgehen wurde vom Hersteller als „Trimodality Imaging" vermarktet, da bei der sequentiellen Untersuchung Daten aus CT, MRT und PET anfallen. Wesentlich ist hierfür außer der bimodal nutzbaren Liege auch eine effiziente Software für die post-hoc Fusion der MRT-Daten mit den PET-Daten aus dem PET/CT.

Idealerweise sollten die beiden Untersuchungsräume bei diesem System unmittelbar benachbart sein, so dass auch beim Patiententransport zwischen PET/CT und MRT keine wesentlichen Lageveränderungen stattfinden. Es ist jedoch offensichtlich, dass diese Kombination die oben genannten Probleme für eine post-hoc-Bildfusion zwar reduzieren, jedoch nicht vollständig ausschließen konnte. Aus betriebswirtschaftlicher Sicht vorteilhaft erscheint hingegen die Tatsache, dass keine teuren technischen Neuentwicklungen nötig waren und die Geräte auch getrennt voneinander nutzbar sind. Es können also jederzeit PET/CT und MRT separat betrieben werden, wenn Patienten mit entsprechenden Indikationen untersucht werden sollen. Zudem kann die beim PET erforderliche Schwächungskorrektur der akquirierten Daten weiterhin mit den CT-Daten erfolgen, während für kombinierte

PET/MRT-Geräte neue Ansätze zur Schwächungskorrektur erforderlich wurden (siehe Abschnitt 1.3).

Nachdem die integrierten Geräte (siehe Abschnitt 1.2.3) sich in den letzten Jahren verstärkt am Markt etabliert haben, wurde im Jahr 2014 von GE eine zweite PET/MRT Generation vorgestellt, in der beide Bildgebungen ebenfalls in einem Gerät kombiniert sind. Hierfür wurde unter anderem ein für die Detektion des PET-Signals erforderlicher Silicon-Photomultiplier-Detektor neu entwickelt. Dies kann als Signal dafür gewertet werden, dass die Diskussion um die Notwendigkeit einer simultanen Bildgebung abgeschlossen ist [41] und sich der integrierte Ansatz bei der PET/MRT durchsetzt.

1.2.2. Separate Geräte - in einem Raum kombiniert

Die ersten in einer Anlage kombinierten PET/MRT-Systeme wurden von der Firma Philips im Jahr 2010 ausgeliefert. Auch hier waren die beiden Komponenten PET und MRT jedoch nicht in einem Gerät kombiniert, vielmehr wurden beide Geräte *in einem Raum* einander gegenüber aufgestellt und durch den drehbaren Patiententisch verbunden. Hierfür waren lediglich kleinere bauliche Modifikationen zur Abschirmung der beiden Modalitäten nötig [42].

Abbildung 1: Foto des PET/MRT-Systems von Philips Healthcare (Philips Ingenuity TF). Im linken Bildanteil ist der PET-Scanner erkennbar, rechts das 3T-MRT. Beide Systeme sind verbunden durch eine um 180 Grad drehbare Patientenliege. (Quelle: Philips GmbH Market DACH)

Bei diesem System bleibt der Patient ebenfalls auf dem in diesem Falle zentralen Untersuchungstisch gelagert, welcher zwischen den beiden Untersuchungen um 180° gedreht wird, so dass der Patient jeweils in derselben Richtung in das Bildgebungsgerät gefahren wird (siehe Abbildung 1). Aufgrund des fehlenden Transports von einem Raum zum nächsten ist hier eine weitere Reduzierung von Bewegung zwischen den beiden Untersuchungsschritten PET/CT und MRT möglich. Es handelt sich jedoch weiterhin um eine sequentielle Untersuchung. Aufgrund des in diesem Konzept fehlenden CT-Datensatzes musste Philips eine neue Methode zur Schwächungskorrektur der PET-Daten entwickeln.

1.2.3. Integrierte Geräte

Die Firma Siemens setzte als einziger Hersteller von Beginn an auf eine integrierte Lösung der beiden Bildgebungsmodalitäten, um damit eine simultane Darstellung von Stoffwechsel und MR-Charakteristika zu ermöglichen. Hierfür wurde in die Gantry eines aktuellen 3 Tesla-MRT-Scanners ein zusätzlicher PET-Detektor eingebaut (siehe Abbildung 2 und Abbildung 3). Da ein Magnetfeld bei den üblicherweise in PET/CT-Systemen verwendeten Silicon-Photomultipliern einen starken Störeffekt verursacht [32], mussten für die Anwendung im MRT neue Detektoren entwickelt werden. Hierfür kommen bei Siemens aktuell Avalanche Photo Dioden (APD) zur Anwendung, die bei deutlich geringerer Größe relativ unempfindlich sind gegenüber dem äußeren Magnetfeld [36]. Im direkten Vergleich zu einem PET/CT-System mit Silicon Photomulitpliern war die räumliche Auflösung vergleichbar, die Sensitivität bei den APDs sogar höher [43].

Zugleich mussten die MRT-Spulen neu entwickelt werden, um möglichst wenig Störeffekte auf dem Weg vom zerfallenden Positron zum Detektorring zu verursachen. Die im PET/MRT eingesetzten Spulen sind im Vergleich zu denen des normalen MRT technisch etwas anders aufgebaut und insgesamt dünner und leichter, so dass sie das emittierte Signal aus dem Betazerfall weniger beeinflussen.

Mit diesen technischen Innovationen war es nun möglich, PET- und MRT-Signale simultan zu messen. Jedoch war auch für diese Lösung eine neue Methode zur Schwächungskorrektur der PET-Daten nötig (siehe Abschnitt 1.3).
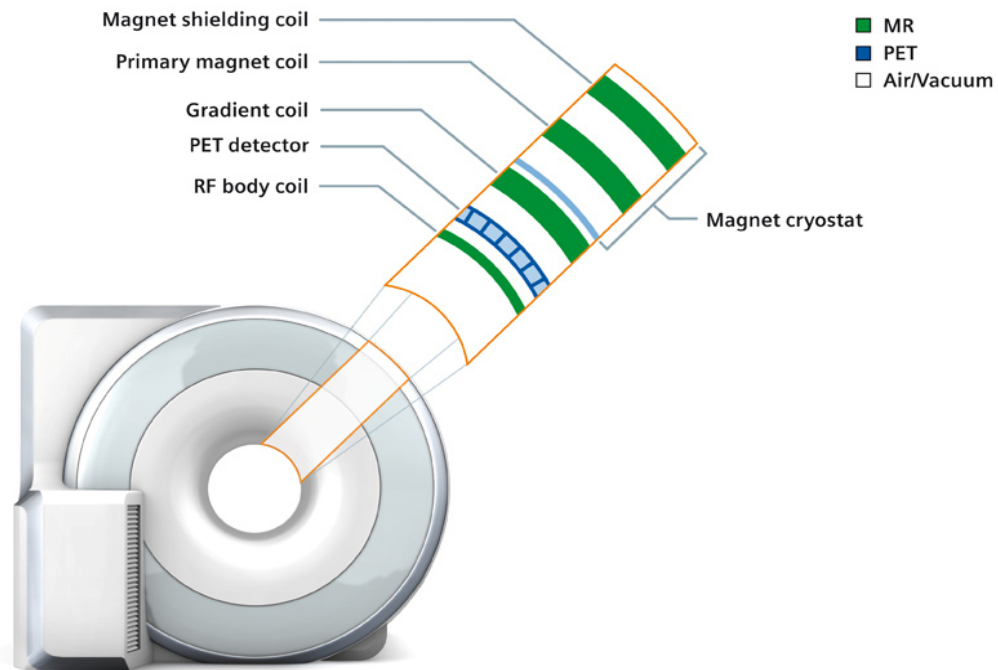
Abbildung 2: Schematische Darstellung des PET/MRT-Aufbaus mit dem PET-Detektorring zwischen den Gradientenspulen und der Körperspule (RF body coil). (Quelle: Siemens Healthcare).

Abbildung 3: PET/MRT-Scanner am Universitätsklinikum Leipzig AöR (Siemens Biograph mMR). Der PET-Detektorring ist in die Bohrung des 3T-MRT integriert.

1.3. Schwächungskorrektur

Während die Umrechnung der detektierten und im k-Raum aufgezeichneten MRT-Signale in interpretierbare Grauwertbilder in üblicher Weise vorgenommen werden kann, ist für die korrekte Abbildung eines aufgezeichneten PET-Datensatzes noch eine Schwächungskorrektur nötig. Nicht schwächungskorrigierte PET-Datensätze zeigen eine sehr hohe Aktivität an der Körperoberfläche und eine relativ schwache Aktivität aus dem Körperinneren, wodurch im Extremfall sogar pathologische Befunde unerkannt bleiben und so zu einer falsch-negativen Interpretation führen können. Um die unterschiedlich starke Schwächung der Positronenzerfallsstrahlung auszugleichen, wurden in den ersten PET-Systemen Transmissionsmessungen vorgenommen, mit welchen die Schwächungswerte der einzelnen Körperpartien ermittelt wurden [44–47].

Die Kombination mit der Computertomographie erlaubte eine deutliche Beschleunigung der Untersuchung, da der zeitaufwändige Transmissionsscan entfallen konnte. Stattdessen wurden die CT-Daten zu Hilfe genommen, die eine unmittelbare Beschreibung des Schwächungsverhaltens durch die einzelnen erfassten Voxel darstellen. Zwar ist der an den Hounsfield-Einheiten ablesbare Schwächungswert des einzelnen Voxels auf die Photonenenergie bei 120 kV bezogen, doch daraus lässt sich der Schwächungswert desselben Voxels bei der im PET vorliegenden Zerfallsstrahlung mit 511 kV berechnen bzw. abschätzen [44, 45, 48–50].

Diese Möglichkeit ist bei der Kombination eines PET-Scanners mit dem MRT nicht mehr gegeben. Hier entwickelten die Hersteller unterschiedliche Lösungen. Während GE zunächst beim klassischen Ansatz der PET/CT bleiben konnte und nur die post-hoc Bildfusion der mittels CT-Daten schwächungskorrigierten PET-Bilder mit den MRT-Sequenzen vollziehen musste, war bei den beiden anderen Herstellern ein neuer technischer Ansatz erforderlich. Die beteiligten Ingenieure verwendeten dazu eine spezielle Sequenz, die als m-Dixon bekannt ist [51] und bei der aus einem T1-gewichteten Datensatz vier verschiedene Parameterbilder berechnet werden können: in-Phase-Bilder, Gegenphase-Bilder, Fettbilder und Wasserbilder. Die Kombination der verschiedenen Parameter erlaubt dann die Differenzierung von verschiedenen „Gewebsklassen", wobei hier Umgebungsluft, Fett, Weichgewebe und Lungen unterschieden werden [52]. Es fällt auf, dass die relativ stark zur Strahlenschwächung beitragenden Knochen in diesem System nicht erfasst werden. Dieser Nachteil wurde bislang

in Kauf genommen, da die durchgeführten Vergleichsrechnungen eine sehr gute Korrelation der PET-Daten aus PET/MRT und PET/CT zeigten. Insbesondere im Bereich der ossären Strukturen wird jedoch die mit dem standardized uptake value (SUV) beschriebene Zerfallsaktivität systematisch unterschätzt [52–55].

Der SUV-Wert dient der Quantifizierung von im PET detektierten Zerfallsereignissen und erlaubt in einem gewissen Maße zwischen benignen und malignen Veränderungen zu differenzieren [56–62]. Vor allem hilft der SUV-Wert jedoch dabei, einen intraindividuellen Vergleich zweier Untersuchungen an demselben Patienten durchzuführen, um z.B. ein Therapieansprechen frühzeitig nachweisen zu können [63–66].

Untersuchungen zum Vergleich der SUV-Werte aus PET/MRT und PET/CT zeigen, dass die Korrelation der Werte aus den beiden hybriden Bildgebungsmodalitäten sehr hoch ist. Dabei liegen allerdings die Werte in der PET/MRT in einigen Untersuchungen systematisch höher als in der PET/CT [52, 55], in anderen hingegen systematisch niedriger [67–69]. Ein direkter Vergleich von Werten, die zwar am selben Patienten, jedoch an PET/CT einerseits und PET/MRT andererseits erhoben wurden, ist damit nicht möglich.

1.4. Einsatzgebiete

Schon während der Entwicklung der PET/MRT-Geräte wurde über mögliche Vorteile der neuen Technik spekuliert [28, 29, 31, 32, 70]. Erwartungen bezüglich einer genaueren bzw. besseren Diagnose wurde insbesondere für die Bereiche der Tumordiagnostik geäußert, in denen die CT aufgrund des geringen Weichgewebskontrastes Einschränkungen aufweist. Dies gilt insbesondere für Kopf-Hals-Tumoren und Tumoren im Beckenbereich, aber auch für die Detektion von Lebermetastasen.

Während im Bereich der Hirndiagnostik eine retrospektive Fusion von MRT-Daten mit Bilddaten aus der PET/CT unter Nutzung aktueller Fusionssoftware relativ einfach möglich ist, bereitet diese post-hoc Fusion in den drei oben genannten Bereichen größere Schwierigkeiten. Bei Halsuntersuchungen ist die identische Lagerung des Kopfes nicht immer einfach zu bewerkstelligen. Die Leber ist atemverschieblich und es kann durch unterschiedliche Atemlagen während des PET-Scans und des CT-Scans zu Verschiebungen kommen. Im Becken schließlich spielen der Füllungsstand der Harnblase und die Darmmotilität eine zusätzliche Rolle. Insbesondere am Hals können aufgrund der engen anatomischen Verhältnisse kleine Verschiebungen in der Fusion rasch zu Fehlzuordnungen des PET-Signals bezüglich des anatomischen Korrelats führen.

In der PET/CT werden die Bilddaten grundsätzlich sequentiell akquiriert. In der integrierten PET/MRT hingegen ist eine simultane Bilddatenakquisition möglich, die eine höhere Genauigkeit in der Bildfusion mit sich bringt [33].

Ein häufig zitierter Vorteil der PET/MRT gegenüber der PET/CT ist die verringerte Exposition des Patienten gegenüber ionisierender Strahlung. Die Strahlenexposition hängt bei der PET/CT von beiden verwendeten Modalitäten ab. Für die PET erhält der Patient eine gewichtsadaptierte Dosis des Radiotracers, woraus je nach Tracer eine effektive Strahlungsdosis von ca. 2-10 mSv resultiert [71–73].

Der zweite Strahlungsanteil bei der PET/CT resultiert aus der CT und ist stark abhängig von der Patientenkonstitution mit den bildtechnisch nötigen Parameterkombinationen aus Röhrenspannung und –strom sowie dem gewählten Untersuchungsprotokoll. Je nachdem, ob lediglich eine low-dose-CT zur Schwächungskorrektur durchgeführt wird oder eine gegebenenfalls auch mehrphasige, voll diagnostische CT, schwankt die effektive Dosis des CT-Protokolls für die Patienten zwischen 7 und >30 mSv [73].

Es sind also bei Ersatz des CT-Anteils durch die Verwendung der MRT Dosiseinsparungen von ca. 50-90% möglich. Dies ist sicherlich ein gewichtiges Argument bei der Untersuchung besonders strahlensensibler Patientengruppen wie Kinder und Jugendliche bzw. bei Patienten mit benignen Erkrankungen. Das wird auch in der weltweit ersten Publikation zur PET/MRT bei Kindern und Jugendlichen von Prof. Hirsch aus der Abteilung für Pädiatrische Radiologie an der Klinik und Poliklinik für Diagnostische und Interventionelle Radiologie des Universitätsklinikums Leipzig hervorgehoben [74]. Er berichtet dabei über die ersten Erfahrungen an einem Kollektiv von 15 Patienten, bei denen insgesamt 21 PET/MRT-Untersuchungen mit 18F-FDG als Radiotracer erfolgreich durchgeführt werden konnten mit einer Reduktion der effektiven Strahlendosis von ca. 80%. Dies ist der Grund, weshalb auch in anderen Einrichtungen, die über eine PET/MRT verfügen, inzwischen die pädiatrischen PET-Untersuchungen nahezu ausschließlich mittels PET/MRT durchgeführt werden.

Auch im Bereich der neurologischen Diagnostik bestehen große Erwartungen an die PET/MRT, insbesondere bezüglich einer integrativen Diagnostik von Hirntumoren, aber auch bei neurodegenerativen Erkrankungen [75–81]. Auch dieser Bereich wird an der Universität Leipzig intensiv beforscht [78, 82, 83], soll jedoch nicht Gegenstand dieser Arbeit sein.

Weitere Einsatzgebiete der PET/MRT sind die Kardiodiagnostik [84–87] sowie andere benigne Erkrankungen wie zum Beispiel entzündliche Skeletterkrankungen [88]. Auch hierzu wurden von unserer Arbeitsgruppe inzwischen Ergebnisse publiziert [89]. Hierfür wurde eine Gruppe von 30 konsekutiven Patienten mit Verdacht auf Spondylodiscitis untersucht, bei denen jedoch Klinik und Paraklinik nicht eindeutig waren und auch das initiale MRT keine sichere Differenzierung zu einer aktivierten Arthrose erlaubte. Der Einsatz einer simultanen 18F-FDG-PET/MRT erlaubte in dieser Situation mit einer Sensitivität von 100% und einer Spezifität von 88% die Diagnose einer Spondylodiscitis. In dieser Habilitationsschrift werden im Folgenden jedoch die Ergebnisse zur onkologischen Diagnostik vorgestellt.

1.5. Untersuchungsprotokoll am PET/MRT

1.5.1. Allgemeine Überlegungen zum Untersuchungsablauf

Nach der Installation des kombinierten Scanners an der Universität Leipzig im September 2011 musste der genaue Ablauf der Patientenuntersuchungen festgelegt werden. Die Vorerfahrungen auf diesem Gebiet waren sehr begrenzt, so dass hier Diskussionen zwischen den beiden beteiligten Fächern - der Radiologie und der Nuklearmedizin - hinsichtlich der Untersuchungsprotokolle geführt wurden.

Bei PET/CT-Untersuchungen bestimmt die Akquisition der PET-Daten im Wesentlichen die Untersuchungszeit. Die anatomische Bildgebung mit der CT ist in sehr kurzer Zeit möglich (je nach Untersuchungsregion und verwendetem CT-Scanner wenige Sekunden bis maximal ca. 1 Minute). Für eine ausreichende Detektion des radioaktiven Zerfalls in einer Bettposition ist meist eine Zeit zwischen eineinhalb und vier Minuten erforderlich (Bettposition = Bereich entlang der Gerätelängsachse, der während einer einzelnen PET-Messung erfasst werden kann, meist ca. 15-20 cm). Typischerweise werden die PET/CTs als sogenannte Ganzkörperbildgebung vom Schädel bis zu den Oberschenkeln durchgeführt, wofür die Messung an mehreren Bettpositionen erforderlich ist. Bei speziellen Fragestellungen / Tumoren wird aber auch eine zusätzliche Untersuchung der unteren Extremitäten durchgeführt, so dass eine echte Ganzkörperuntersuchung resultiert. Klassische Indikationen für die „echte" Ganzkörperdiagnostik sind die Detektion bzw. Lokalisation von systemischen Entzündungen, aber auch die Ausbreitungsdiagnostik bei systemischen Tumorerkrankungen wie dem multiplen Myelom beziehungsweise anderer Lymphome oder Tumoren mit häufig an Extremitäten auftretenden Filiae wie z.B. dem malignen Melanom [14, 90–92]. Für die häufiger durchgeführte „normale" Ganzkörperuntersuchung sind 5-6 Bettpositionen für die Datenakquisition des PET-Signals typisch, so dass eine Gesamtuntersuchungszeit von ca. 15-30 Minuten resultiert.

Im Unterschied dazu bestimmt bei der PET/MRT die MRT die Untersuchungszeit. Zwar zeigten Hartung-Knemeyer et al., dass bereits 2 Minuten Datenakquisition für die zuverlässige Detektion hypermetaboler Läsionen an dem von uns verwendeten PET/MRT-Scanner ausreichen [93]. In den simultanen Geräten findet jedoch während der PET-Datenakquisition auch die Messung der verschiedenen MRT-Sequenzen statt, inklusive der

teilweise zusätzlich nötigen Shims zur Homogenisierung des Magnetfeldes im Messbereich. Somit hängt die Dauer der Messung pro Bettposition davon ab, wie viele verschiedene MRT-Sequenzen akquiriert werden sollen.

1.5.2. MRT-Sequenzen

Die MRT stellt eine sehr vielfältige Methode mit zahlreichen zur Verfügung stehenden Sequenzen dar. Neben der reinen anatomischen Darstellung ist mit der MRT inzwischen auch eine funktionelle Beurteilung von Gewebe möglich, wobei aktuell vor allem die diffusionsgewichtete Bildgebung (DWI) und die dynamische, kontrastmittelverstärkte Perfusionsbildgebung (dynamic contrast-enhanced MRI: DCE-MRT) in der onkologischen Diagnostik verwendet werden [94–99]. Zusätzlich können auch Parameterkarten erstellt werden zur Gewebecharakterisierung hinsichtlich verschiedener Relaxationszeiten, wie z.B. T1-, T2-, T2*-mapping [100, 101]. Diese Techniken finden derzeit allerdings vorwiegend in der Forschung auf dem Gebiet der kardialen und muskuloskelettalen Bildgebung ihre Anwendung.

Für jede einzelne Sequenz ist in der MRT zusätzliche Messzeit nötig, so dass für die Anwendung in der PET/MRT ein Kompromiss hinsichtlich der verwendeten Sequenzen gefunden werden musste. Übereinstimmend sollte – im Interesse einer ausreichenden Akzeptanz bei den Patienten einerseits und einer relativen Zeiteffizienz andererseits – die Untersuchungszeit pro Patient unter einer Stunde gehalten werden.

Die Grundidee bei der Erstellung der Protokolle war es, die Stärken der Ganzkörperbildgebung beizubehalten und mit den Stärken der MRT hinsichtlich der lokalen Tumordetektion und –differenzierung zu ergänzen. Umgesetzt wurde dies, indem zunächst eine „typische" Ganzkörperbildgebung mit 5 Minuten Untersuchungszeit pro Bettposition erfolgte. In dieser Zeit konnten die folgenden MRT-Sequenzen durchgeführt werden:
1. Dixon-Sequenz - zur Schwächungskorrektur
2. schnelle T2-gewichtete single-shot Sequenz (HASTE) – zur anatomischen Darstellung
3. diffusionsgewichtete Messung (DWI) – zur Detektion von Molekularbewegung
4. fettgesättigte T2-gewichtete Spinecho-Sequenz (TIRM) – bisheriger Standard in der onkologischen Ganzkörperdiagnostik im MRT [102, 103].

Eine genaue Übersicht über die Meßparameter dieser Sequenzen gibt die Tabelle 1.

Sequenz	Orientierung	TR [ms]	TE [ms]	FA [°]	Schicht-anzahl	Schichtdicke [mm]	Voxelgröße [mm]	TA [min]
Dixon	Koronar	3,6	1,23	10	128	2,6	4,1x2,6x2,6	0:19
Haste	Axial	800	89	120	40	4	1,8x1,4x4,0	0:32
DWI	Axial	6800	73	n.a.	30	6	4,3x3,5x6,0	1:15
TIRM	Koronar	2090	47	120	40	5	3,1x1,6x5,0	1:00

Tabelle 1: MR-Sequenzparameter für die Ganzkörperbildgebung. Jede der aufgeführten Sequenzen wurde pro Bettposition des PET akquiriert. TR = Repetitionszeit, TE = Echozeit, FA = Flipwinkel, TA = Akquisitionszeit, mDixon = T1-gewichtete Sequenz zur Schwächungskorrektur, Haste = half-Fourier acquisition single-shot turbo spin-echo, DWI = diffusion weighted imaging, TIRM = turbo inversion recovery magnitude.

Diese Ganzkörperbildgebung wurde dann ergänzt um ein an die entsprechende Tumorfragestellung angepasstes MRT-Protokoll, wofür die klassischen Sequenzen aus dem schon am Klinikum existenten 3T-MRT adaptiert wurden.

Entsprechend der in Leipzig verfolgten Fragestellungen (siehe Abschnitt 1.6) wurden dafür zunächst Protokolle für die Kopf-Hals-Bildgebung, für die Beckenregion und für die Leber implementiert. Die Parameter für die Kopf-Hals-Bildgebung können der Tabelle 2 entnommen werden.

Halsuntersuchung								
Sequenz	Orientie-rung	TR [ms]	TE [ms]	FA [°]	Schicht-anzahl	Schicht-dicke [mm]	Voxelgröße [mm]	TA [min]
T1w TSE	Axial	780	12	140	42	4	1,1x0,5x4,0	2:34
T2w fs TSE	Axial	5640	105	140	42	4	0,8x0,5x4,0	4:15
T2w TIRM	Koronar	3500	44	150	38	3	1,0x0,8x3,0	4:07
EPI-DWI	Axial	8620	73	n.a.	30	4	3,2x2,6x4,0	1:35
T1w-3D FLASH DCE	Axial	2,47	0,97	8	40	5	1,2x1,0x5,0	4:00
T1w fs TSE CE	Axial	996	12	140	42	4	1,1x0,5x4,0	3:16
T1w fs TSE CE	Koronar	817	19	150	38	3	1,0x0,6x3,0	3:20
T1w-3D VIBE CE	Axial	3,35	1,14	10	72	3	0,9x0,9x3,0	0:34

Tabelle 2: MR-Sequenzparameter für die spezielle Kopf-Hals-Bildgebung. TR = Repetitionszeit, TE = Echozeit, FA = Flipwinkel, TA = Akquisitionszeit, T1w-/T2w-TSE = T1-/T2-gewichtete Turbo-Spin-Echo, fs = fettgesättigt, TIRM = turbo inversion recovery magnitude EPI-DWI = echoplanar imaging diffusion weighted imaging, FLASH = fast low angle shot, CE = contrast enhanced.

Diese Untersuchungsstrategie wird von den meisten anderen Betreibern von PET/MRTs ebenfalls verfolgt, wenngleich die verwendeten MRT-Sequenzen von Standort zu Standort variieren. Es gibt inzwischen auch erste Studien zur Frage, welche Sequenzen überhaupt nötig sind bzw. ob wirklich eine Kombination aus Ganzkörperbildgebung und dedizierten Protokollen nötig ist. Allerdings werden diese Fragen vorwiegend von den Kollegen in Zürich aufgeworfen, welche die Trimodality-Strategie nutzen [104–110]. Für diese Gerätekombination sind jedoch sicherlich andere Untersuchungsstrategien sinnvoll als für integrierte PET/MRTs. Wenn im Trimodality-Ansatz bei der Akquisition der PET-Daten ein CT-Datensatz zum anatomischen Ganzkörperstaging angefertigt wird, kann die anschließende

MRT-Untersuchung auf die Primärtumorregion fokussiert werden, um hier die Vorteile der MRT hinsichtlich des Gewebekontrastes auszunutzen.

Bei den integrierten Geräten ist jedoch die Anfertigung eines Ganzkörper-MRTs aus zwei Gründen erforderlich. Zum einen muss hier die zur Schwächungskorrektur und damit zur SUV-Quantifizierung nötige Sequenz durchgeführt werden. Zum anderen sind auch weitere Sequenzen zur Tumordetektion sinnvoll. Welche dies sind, wird in den nächsten Jahren sicher weiter diskutiert werden. Eine aktuelle Arbeit von Schaarschmidt et al. stellt zumindest die Sinnhaftigkeit einer nativen T1-gewichteten Sequenz in Frage [110].

In der praktischen Anwendung für onkologische Fragestellungen wird es aus diesen Gründen bei integrierten PET/MRT-Geräten vermutlich auf absehbare Zeit bei einer Kombination aus einer Ganzkörperuntersuchung und einer dedizierten Darstellung der Primärtumorregion bleiben.

1.5.3. Angewendete PET-Tracer

18Fluor-Fluorodesoxyglucose (18F-FDG) ist der Standardtracer in der onkologischen PET-Diagnostik und wird für sehr viele Tumoren eingesetzt. Der radioaktiv markierte Zucker wird dabei in die Körperzellen aufgenommen, jedoch nur unvollständig verstoffwechselt und damit in der Zelle gefangen. In Regionen mit einem hohen Glukoseumsatz zeigt sich dann ein intensiveres Signal, das vom ß-Zerfall der Positronen ausgeht [50]. In unseren Studien wurde 18F-FDG für die Detektion von Kopf-Hals-Tumoren und von Zervixkarzinomen verwendet.

Bei Prostatakarzinomen wurde in Leipzig im Laufe der vergangenen vier Jahre der Tracer gewechselt. Zu Beginn wurde noch C11-markiertes Cholin verwendet, das in die Zellmembran eingebaut wird und hierdurch einen gesteigerten Zellumsatz anzeigt. Seit 2014 wird das 68Ga-markierte prostataspezifische Membranantigen (PSMA) genutzt, welches aber nicht alleinig an Prostatagewebe, sondern auch an Zellen der Speicheldrüsen und Nieren bindet, geringer an Tränendrüsen, Leber und Milz [111–114].

Auch für die Detektion von differenziertem neuroendokrinem Tumorgewebe werden Antikörper verwendet, welche in diesem Falle gegen Untereinheiten des Somatostatinrezeptors gerichtet sind. Diese Antikörper sind mit 68Ga-markierter Tetraazacyclododecantetraessigsäure (DOTA) gekoppelt und werden – je nachdem, an

welchem Rezeptorsubtyp sie bevorzugt binden – als 68Ga-DOTATOC, -DOTANOC oder – DOTATATE bezeichnet [115]. An unserem Klinikum kommt dabei bevorzugt das DOTATOC zum Einsatz.

Während sich bei der Diagnostik von Kopf-Hals-Tumoren und Beckentumoren die Region der dedizierten Diagnostik von alleine ergibt, wurde bei der Suche nach neuroendokrinen Tumoren die Ganzkörperdiagnostik mit einer speziellen MRT-Untersuchung des Oberbauches bzw. der Leber kombiniert. Hierfür wurde ein leberspezifisches Kontrastmittel verwendet (Gd-EOB-DTPA), von welchem bekannt ist, dass es die höchste Genauigkeit in der Diagnostik von Leberfiliae aufweist [116–119].

1.6. Eigene Studien

Bei der Beantragung von Fördermitteln der DFG zur Anschaffung eines PET/MRT-Gerätes wurden vom Leipziger Expertengremium onkologische Fragestellungen formuliert, die bearbeitet werden sollten. Nach dem erfolgreichen Antrag und dem Votum der DFG für den Standort Leipzig konnten die Fragestellungen genauer definiert und die Patientengruppen klarer festgelegt werden. In Übereinstimmung mit den in Abschnitt 1.1 genannten Bereichen wurden Studien konzipiert, die die diagnostische Wertigkeit der PET/MRT im Vergleich zur PET/CT evaluieren sollten. Diese bezogen sich vornehmlich auf:

- Kopf-Hals-Tumore (Primärdiagnostik, Rezidivdiagnostik, CUP)
- Beckentumore (Primärdiagnostik und Rezidivdiagnostik bei Zervixkarzinom und Prostatakarzinom)
- Neuroendokrine Tumore

Die Untersuchungsstrategien der Teilbereiche waren hinsichtlich der verwendeten nuklearmedizinischen Tracer und der dedizierten MRT-Protokolle unterschiedlich (siehe Abschnitt 1.5).

Das wissenschaftliche Interesse galt nun vorrangig dem Nachweis von möglichen Vorteilen dieser innovativen Diagnostik-Modalität vor dem Hintergrund des apparativen und kostspieligen Aufwands dieser Untersuchungsverfahren. Am Ende sollte ein signifikanter Benefit für den Patienten resultieren und Argumente für die Indikationserweiterung auf andere Anwendungsbereiche gesammelt werden.

Im folgenden Abschnitt sind die eigenen Publikationen dargestellt, die diese Fragestellungen bearbeitet haben.

2. Originalarbeiten

2.1. Physikalische und organisatorische Maßnahmen für Installation, regulatorische Anforderungen und Implementierung eines simultanen hybriden PET/MR-Bildgebungssystems in Forschung und klinischer Versorgung

Ehe all diese Fragestellungen jedoch angegangen werden konnten, waren zahlreiche technische Besonderheiten zu berücksichtigen. Bereits bei der Planung des Neubaus der Klinik und Poliklinik für Nuklearmedizin, wo der PET/MRT-Scanner inzwischen betrieben wird, wurden die erforderlichen baulichen Maßnahmen zur Abschirmung hinsichtlich des starken Magnetfeldes, der Positronenzerfallsstrahlung und der hochfrequenten elektromagnetischen Impulse berücksichtigt. Weitere zu beachtende Aspekte waren die Zuführung der Versorgungsleitungen bzw. der Verlauf des Quenchrohres für das MRT. Ebenfalls vor Inbetriebnahme des Gerätes mussten Qualitätschecks und Konstanzprüfungen der beiden Komponenten durchgeführt werden. Wie schon vorher beschrieben, mussten dann die Untersuchungsprotokolle für verschiedene Indikationen bzw. Forschungsbereiche festgelegt werden.

Die Erfahrungen, die am Universitätsklinikum Leipzig zu diesen Themen gesammelt wurden, sind in einem 2012 erschienenen Artikel von Sattler et al. zusammengefasst, welcher im Folgenden als erste Arbeit dieser Habilitationsschrift aufgeführt wird [120].

Sattler, Bernhard; Jochimsen, Thies; Barthel, Henryk; Sommerfeld, Kerstin; ***Stumpp, Patrick***; Hoffmann, Karl-Titus; Gutberlet, Matthias; Villringer, Arno; Kahn, Thomas; Sabri, Osama (2013):
Physical and organizational provision for installation, regulatory requirements and implementation of a simultaneous hybrid PET/MR-imaging system in an integrated research and clinical setting.
Magma 26 (1), S. 159–171.

REVIEW ARTICLE

Physical and organizational provision for installation, regulatory requirements and implementation of a simultaneous hybrid PET/MR-imaging system in an integrated research and clinical setting

Bernhard Sattler · Thies Jochimsen · Henryk Barthel · Kerstin Sommerfeld · Patrick Stumpp · Karl-Titus Hoffmann · Matthias Gutberlet · Arno Villringer · Thomas Kahn · Osama Sabri

Abstract The implementation of hybrid imaging systems requires thorough and anticipatory planning at local and regional levels. For installation of combined positron emission and magnetic resonance imaging systems (PET/MRI), a number of physical and constructional provisions concerning shielding of electromagnetic fields (RF- and high-field) as well as handling of radionuclides have to be met, the latter of which includes shielding for the emitted 511 keV gamma rays. Based on our experiences with a SIEMENS Biograph mMR system, a step-by-step approach is required to allow a trouble-free installation. In this article, we present a proposal for a standardized step-by-step plan to accomplish the installation of a combined PET/MRI system. Moreover, guidelines for the smooth operation of combined PET/MRI in an integrated research and clinical setting will be proposed. Overall, the most important preconditions for the successful implementation of PET/MRI in an integrated research and clinical setting is the interdisciplinary target-oriented cooperation between nuclear medicine, radiology, and all referring and collaborating institutions at all levels of interaction (personnel, imaging protocols, reporting, selection of the data transfer and communication methods).

Bernhard Sattler and Thies Jochimsen contributed equally.

B. Sattler (✉) · T. Jochimsen · H. Barthel · O. Sabri
Department of Nuclear Medicine, University Hospital Leipzig,
Liebigstrasse 18, 04103 Leipzig, Germany
e-mail: Bernhard.sattler@medizin.uni-leipzig.de

K. Sommerfeld
Department of Project Development and Technical Planning,
University Hospital Leipzig, Leipzig, Germany

P. Stumpp · T. Kahn
Department of Diagnostic and Interventional Radiology,
University Hospital Leipzig, Leipzig, Germany

K.-T. Hoffmann
Department of Neuroradiology, University of Leipzig,
Leipzig, Germany

M. Gutberlet
Department of Radiology, Heart Center Leipzig, University
Hospital, University of Leipzig, Leipzig, Germany

A. Villringer
Max Planck Institute for Human Cognitive and Brain Sciences,
Leipzig, Germany

Introduction

In general, the implementation of hybrid imaging systems requires long-term, thorough and anticipatory planning. These arrangements are particularly important for cross modality PET/MRI systems. Several physical, constructional, radiation-protection, and safety regulatory provisions have to be met. In this article, we focus on a hybrid system which for the first time allows for simultaneous whole-body PET and 3 T MRI measurements, the SIEMENS Biograph mMR. However, to be as complete as possible, we have integrated some information for sequential PET/MRI systems that are also available.

Constructional requirements

The facility in which a PET/MRI system will be installed should consist of at least five parts: the examination

(scanning) room, a technical room, patient changing cabin(s), a patient preparation room and the control room. It is advisable to have the scanning room located in the center of these rooms and to have all the other rooms, except the patient changing cabin(s), next door. For convenience, the patient changing cabin(s) should connect the aisle directly to the patient preparation room. Depending on the expected patient throughput, more peripheral rooms for patient waiting, radionuclide application and patient relaxation may be needed. The rooms close to the scanning room must be protected against magnetic influences by the high static magnetic field (3 T) and ionizing gamma radiation resulting from radionuclides used for PET. Moreover, the scanner room must be shielded against radio frequency (RF) influences from its environment and vice versa. A principle example layout of such a facility is shown in Fig. 1. These three essential properties are realized by a room-in-room construction consisting of steel, lead and copper constructions, the latter of which forms a Faraday cage or RF chamber which encloses the imaging system. All doors and windows need to be included in these measures. Doors require special opening and closing mechanisms to be moved smoothly (heavy, lead and copper interior) and electrically connected to their RF shielding material with the RF chamber while closed. A double-door setup (outer door for radiation shielding, inner for RF shielding) is worth considering. The walls between the scanner, control and technical rooms must have openings for filter panels for RF shielding to permit the connection of power, signals, gases, etc., as well as wave-guide openings to feed through connections to medical equipment to be located apart from the influence of the RF and the static magnetic field, respectively. These openings need to be located above the radiation shielding construction (above 2.2 m) or at locations where personnel have no direct access. It is advisable to provide at least one spare filter panel, since retrofitting of filter panels in case of later upgrades is almost impossible. Above the RF cabin construction, there is about 1.5 m extra room height needed for installations, and it is strongly advisable to have this walkable for service, accessible from the control or technical room. So the scanner room shell construction should have at least 40 m^2 (non-square!) and be about 4.5–5.0 m high. Non-integrated PET/MRI-systems with separated PET- and MRI-gantries and a unique patient handling (or shuttle) system need a larger footprint or even a separate room for each of the gantries. To guarantee correct registration of the images acquired by both of the modalities, the patient is kept in the same position on the patient handling system and is moved from MRI to PET or vice versa. Moreover, such systems allow for a bigger bore to insert the patient at both modalities, since there is no space consumed inside the MR-gantry by PET-detectors.

Windows need to be made of lead glass to ensure ionizing radiation shielding and should have a translucent metal grid as part of the RF shield. Again, a multilayer design (i.e., inner and outer window) is most feasible. The radiation shielding needs to be specified to meet the regulatory requirements of the maximal level of the radiation dose rate outside the scanning room. The radiation shield needs to ensure that the occupational radiation exposure of a person does not exceed 6 or 20 millisievert per year (mSv/yr) and 1 m Sv/yr for members of the public [1–3]. The maximal amount of radioactivity, the mean time of stay at certain points in the control room (PET/MRI staff) or the public area (members of the public), the distance to the radiation source, and the shielding material properties (mostly lead, steel or barite-concrete) need to be taken into account for the calculation of the thickness of the radiation shielding/walls.

Moreover, the scanning room floor must be able to support the weight of the system, which totals about 9,000 kg, and be conductive for electrical safety. The central part of the integrated system consists of the helium-cooled magnet and the gradient system fully integrated with the PET detector ring and the patient handling system. Its dimensions require a thorough planning of the pathway that will be used to bring the system into its final location. In existing buildings, normal pathways cannot be used because of the weight and dimensions of the central system unit. Normally, a transport opening needs to be prepared in the façade of the building. This can be a large door or one-time opening of about 3.0 by 3.0 m. Figure 2 shows the transport of the central system through such an opening. Constructional precautions also need to be taken for the running of the quench pipe that—in case of a quench of the magnet—safely guides the expanding helium out of the building. In most cases, this pipe ends at the roof of the building. In special constructional situations, however, a quench pipe ending in the façade is also adequate.

Additionally, provision for the supply with electrical energy and cooling capacity for the magnet and the facility must be made. A constant electrical power of about 110 kVA and a short-time power consumption of about 150 kVA should be available (400 V ± 10 %). Usually, this cannot be supplied from the existing building feed and, thus, needs to be planned for in advance. The same applies to the cooling capacity of about 80 kW that is mediated by cooled water. The electricity needs to be brought to the system by cables of at least 4 × 70 mm^2, and the cooled water needs to be guided by 2 × 2″ steel (V2A or V4A) lines from the central building cooling unit to the PET/MRI system and back. Peripheral constructional and technical provisions are pre-specified by the manufacturer. These provisions, which are to be ordered, conducted and supervised by the customer, include main electrical and
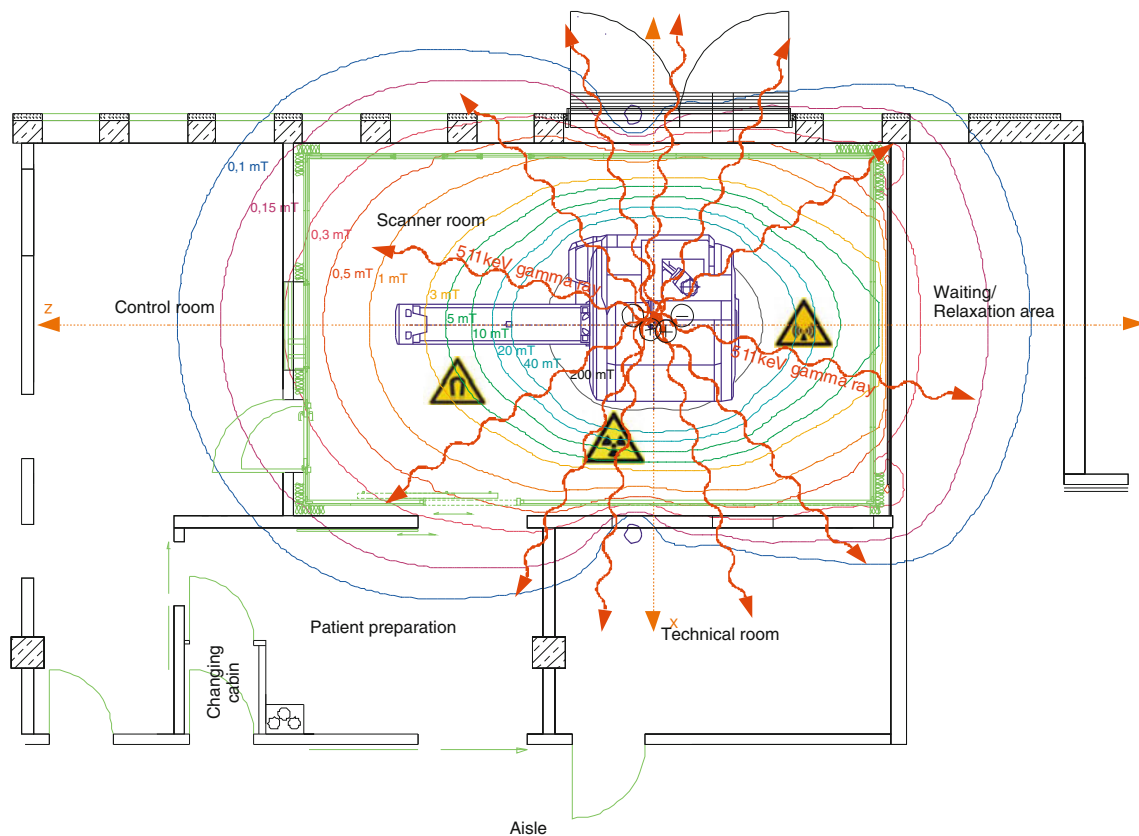
Fig. 1 Principle layout of a PET/MRI-facility consisting of the examination (scanning) room, technical room, patient changing cabin(s), patient preparation room, control room and the waiting and patient relaxation area. The isomagnetic field lines are also displayed. All the walls are equipped with 4 mm lead or are of barite-concrete to 2.2 m height. The *green* construction is part of the inner RF-Faraday cabin

Fig. 2 Transport of the central system unit consisting of the magnet, the gradient system fully integrated with the PET detector ring and the patient handling system. (Photos courtesy of Frank Koschewski, Telekine TV Productions [36])

cooling feed lines, air conditioning, general building construction, facility preparations including the RF cabin, high magnetic field shielding and radiation shielding.

Essential for the efficient optimal of PET investigations is a seamless connection to the production site of the PET radiopharmaceuticals. Standard ^{18}F-marked radiotracers can be obtained from a radiopharmaceutical supplier due to the relatively long physical half-life of ^{18}F (109.8 min). If the use of tracers marked with radionuclides of a shorter physical half-life, such as ^{11}C (20.4 min), ^{13}N (9.9 min) or ^{15}O (2.0 min), is intended, however, a direct and close connection to the cyclotron unit and radiochemistry facility is mandatory. Ideally, the radiotracers are transferred from the production site to the PET/MRI imaging facility with a pneumatic tube system or direct product lines from the cyclotron/radiochemistry to the imaging facility. Additional radiation protection precautions are to be taken depending on the pathway of the tubes/lines. For research and also clinical routine, it is mandatory that the radiopharmaceutical production site is built and run following Good Manufacturing Practice (GMP) rules [4, 5] and regulations specific for one's own country, respectively [6].

Moreover, if anesthesia or subject sedation is necessary, a medical gas supply such as oxygen, air, vacuum, N_2O (combined with used N_2O scavenging) needs to be considered.

Safety precautions

To prevent imaging-related adverse events or accidents, and to guarantee safety of the patients and the staff, some more technical and organizational measures are mandatory in addition to the static high-field magnetic and radiation shielding. First, all personnel must be adequately trained to handle radioactivity in medicine and to work under conditions of a high-field MR system. This is regulated by the relevant radiation safety legislation [1, 3] and the European Council Directives concerning medical devices [7, 8], as well as by the country based Medical Devices Act (in Germany the "Medizinproduktegesetz" [9]). For handling radioactivity in a medical setting, physicians, physicists and technologists need to have legally documented vocational skills in radiation protection (in Germany, for instance, special training courses must be attended every 5 years). Persons who have not completed/actualized that training yet are allowed to work under the guidance and responsibility of persons who are trained and licensed as described. The PET/MRI system must be protected against access by unauthorized personnel or persons who are not aware of the potential risks. This is due to the possible risk of contamination with radioactivity, possible harm by the static magnetic field that is always present, and the risk of

damaging the system, for instance by ferromagnetic material accidentally attracted by the system. Special care must be taken if third party companies are involved, i.e., for room cleaning during off-duty hours.

Medical engineering equipment

The medical engineering equipment that is brought to the scanning room must obviously be compatible with the influence of the high static magnetic field. The fringe field in the scanning room presents a magnetic flow density outside the scanning aperture, ranging from about several hundred milli-Tesla very close to the aperture of the system down to less than 0.5 mT at the doors and walls of the scanning room (Fig. 1). A value of 0.5 mT is the upper limit given by manufacturers of technical or other equipment for safe functionality. This limit is of special importance for persons with cardiac or neurostimulating systems. All equipment brought close to the magnet must be antimagnetic and fully functional under the influence of a high static magnetic field. If the equipment remains in the room while the imaging is performed, it must not emit radiofrequency fields which disturb the reception of the MR signal. Such equipment includes, for instance, a MR-contrast agent pump, anesthesia equipment, general syringe pumps, systems for neural activation or an automated blood sampling system to draw blood samples for radioactivity analysis. Moreover, electronic or film personnel radiation dosimeters also need to fulfill these requirements, since radioactivity—either already in the patient or to be injected at the beginning of the PET-acquisition on the scanner—needs to be handled in the area of the influence of the high static magnetic field. By legislation, such equipment must be worn continuously while handling radioactivity and being exposed to ionizing radiation, respectively. Film dosimeters (with a plastic clip!) fulfill these requirements, current electronic staff dosimeters so far don't.

The patient preparation room needs to be equipped with all medical equipment required for anesthesia preparation and radioactivity handling. In addition to the mobile equipment as mentioned above, this includes a calibrated dose calibrator to assay the radiotracer dose dispensed as required for the particular investigation. Moreover, radiation-shielded (2–5 cm lead) storage locations for the product, radioactive waste and for the radioactive phantoms (mostly with ^{68}Ge) that are used to calibrate the PET system should be available in the preparation room. Equipment for visual stimulation in functional MRI (fMRI) needs special consideration, as ordinary solutions are not compatible with PET/MRI: LCD goggles are not accounted for in the MR attenuation correction (AC) of PET data and, therefore, may lead to errors in its quantification.

Projection onto a screen from the outside (viewed by the subject using a mirror on the head coil) is also problematic, since the required hole in the wall of the scanner room would disrupt the radiation shield. Therefore, other solutions must be used, such as an MR-compatible LCD screen inside the scanner room.

Staffing requirements

If a cross-modality hybrid imaging system is taken into operation, the availability of adequately trained personnel must also be planned in advance. This obviously refers to both the PET and the MRI components of the integrated system and to all professional groups involved (physicians, physicists, and technologists). From our experience, it is reasonable to operate a combined PET/MRI system with one physician, one physicist, and two technologists (all full-time). Depending on the workload in the research and clinical setting, however, more personnel may be necessary.

IT environment and data connections

The system is equipped with an internal network which connects the different components of the system (console, PET and MRI control/reconstruction units). This internal network must remain undisturbed and not be connected to the Local Area Network (LAN) of the facility. Only the operator console system has both a network connection to the internal systems and the LAN. This connection to the LAN is used to connect the PET/MRI system to the remote support system of the manufacturer and to the network of the hospital. The imaging communication uses the DICOM standard [10–12]. First of all, the system should be integrated into the picture archiving and communication system (PACS) of the department. To receive administrative patient data, the system should also be integrated into the radiological information system (RIS) to ensure consistent patient data transfer to the system as a worklist [13]. Departmental PACS systems offer not only adequate image data archiving and communication, they also have applications that allow for data analysis, post-processing and visualisation. Firstly, displaying a "Fused Display" of the PET and MRI data is essential. Secondly, 2D and 3D region-based quantitative analysis—like standardized uptake value (SUV) determination—of the data is available in most systems. In cases when the console system, which hosts some of the applications, is usually not available for data analysis (i.e., during data acquisition), it is essential to run an extra local post-processing system. This should be connected to the console system via the LAN and should receive the desired data via a DICOM connection and an automatic transfer. Depending on the intention of further use of the data, only relevant data has to be archived to prevent overload of the PACS' storage capacity. For instance, a standard whole-body PET/MRI data set comprises the non–attenuation-corrected PET emission data (NAC-PET), the attenuation-corrected PET emission data (AC-PET), the MRI data used to calculate the attenuation map, and data for several diagnostic MRI sequences. Usually this set of data will amount to some 3 GB/subject, but the requirement for data storage will increase if special sequences for fMRI or dynamic PET acquisitions are desired. Such data sets can reach a storage use in the order of 8 GB/subject, and even up to 20 GB/subject if the MRI signal and PET raw event data is included. If storing such data is necessary for research purposes, additional local storage and post processing capacity may be necessary and has to be planned separately. To ensure for security of the networked data interchange and the data itself, data should be communicated only in a restricted, firewall protected local area network (LAN). If data need to be communicated across firewalls, virtual private network (VPN) tunnels or dedicated IP ports and appropriate data encryption/decryption should be used. Here, it needs to be considered that the protection of patient-specific data is subject to regulatory issues that can vary significantly from country to country.

A local Wiki system [14] has proven useful as a collaborative platform to collect important data, instructions and procedures pertaining to the PET/MRI system. For instance, the results of the quality tests (Figs. 3, 4) are shown together with step-by-step instructions on how to perform these tests.

Basic acceptance testing and quality control

After completion of the physical installation of the system, including filling the magnet with helium, ramping it up to full magnetic field strength, final magnet shimming and establishing all network connections to the uptime service centre (UPC), the system is taken into operation guided by the manufacturer's personnel on site and by the UPC at the manufacturer's site. PET and MRI calibration measurements are performed, followed by acceptance testing. The basic parts of the acceptance tests as adapted from [15] are listed in Table 1. Some of the tests suggested by the National Electrical Manufacturers Association (NEMA) for the PET system [16] serve as a reference for the subsequent routine quality control measurements. However, these tests are not part of the standard acceptance testing that is covered in the delivery of the system. If the phantoms are available, the user can perform these tests or charge specialized consultants. The basic routine quality check measures are listed in Table 2 as adapted from [17].

Fig. 3 Trend of the PET calibration factor as a result of the daily quality check of the PET component of the integrated PET/MRI system
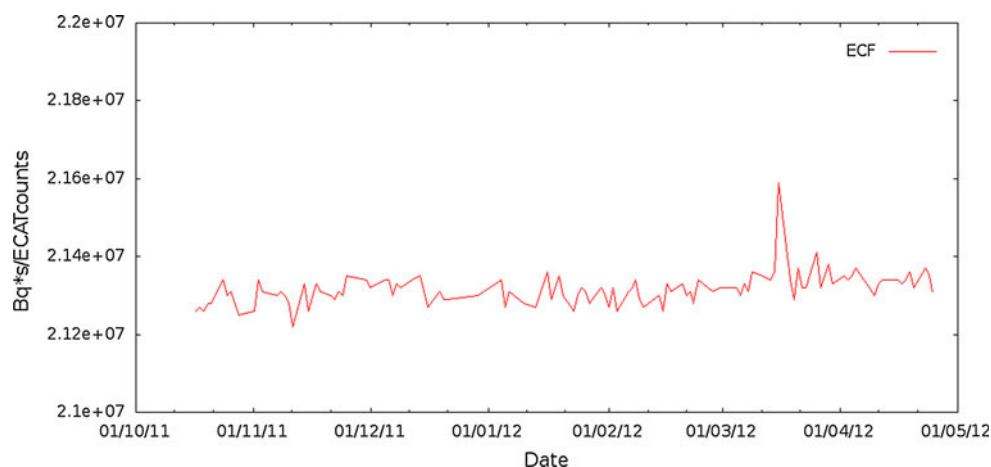
Fig. 4 Parameter trends for the MR component of the integrated PET/MRI system: (**a**) Temporal stability quantified by the fluctuation-noise-to-signal ratio as described in Friedman et al. [38] measured over time using a spherical water phantom. **b** Resonance frequency of the MR system over time. These tests are particularly advisable if a high temporal stability is crucial, e.g., if the system is used for functional studies
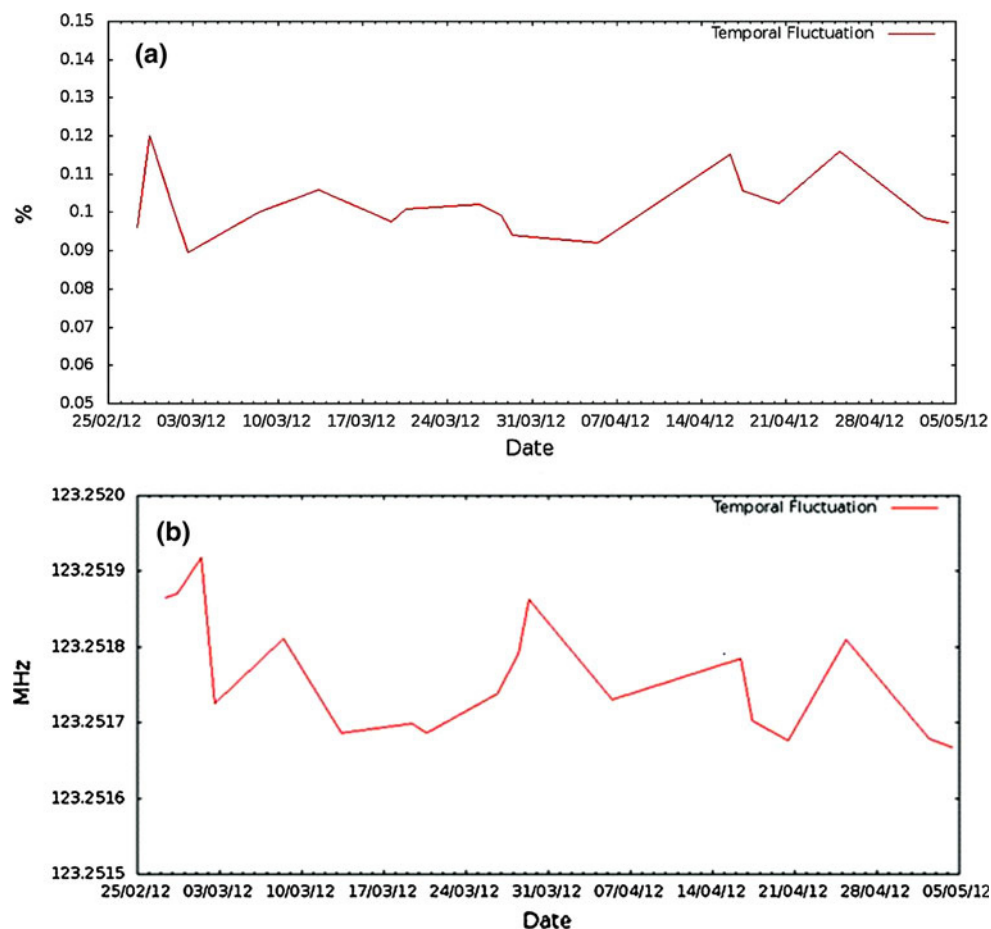
Acceptance and control checks of the PET system are mandatory by radiation safety regulatory requirements in some countries. However, the procedures for the MRI system are not required by regulation but represent good imaging practice such as we would propose for state of the art hybrid PET/MRI imaging.

An important precondition for the clinical use is the approval of the Conformité Européenne (CE) for medical engineering products [7] for Europe and by the Food and Drug Administration (FDA) for the United States.

Imaging protocols

In the following paragraphs, we briefly describe the routine interdisciplinary investigational protocols for oncologic,

Table 1 Basic procedures for acceptance testing of a hybrid PET/MRI system, Acc = acceptance tests

Acceptance testing for PET/MRI
Equipment type: whole-body positron emission tomograph integrated with an MRI-tomograph

Test	Description	Acc	Ref
Full normalization and gantry calibration (PET/MRI) must precede the Acceptance testing!			
PET1. Physical inspection	To check the total system for shipping damage (e.g., gantry, console, computer, display devices) and production and design flaws	X	
PET2. Computer clock	To verify the correct time of day of the data acquisition and processing computer		X
PET3. PET sensitivity	Defines the rate at which coincidence events are detected in the presence of radioactive sources at activity levels where count rate losses are negligible	X [16]	X
PET4. PET uniformity	Describes the ability to measure the same activity independent of location within the imaging FOV	X [16]	X
PET5. Spatial resolution	To measure the intrinsic spatial resolution (FWHM and FWTM) according to NEMA and compare with the manufacturer's specification	X [16]	X
PET6. Count rate performance	To measure count rate as a function of (decaying) activity over a wide range of activities. Peak NEC value, and corresponding count rate, should be compared with the manufacturer's specification. True, random and scatter count rate and scatter fraction could be performed for future reference	X [16]	X
PET7. Image quality (not mandatory)	Hot and cold spot image quality of standardized image quality phantom as described in the NU 2-2007 document [16]. This test is to measure recovery coefficients and signal-to-noise ratio performance of the imaging system		X
MRI1. Physical inspection	To check the MRI scanner part of the PET/MRI system for shipping damage and production and design flaws (done by the manufacturer)	X	
MRI2. magnet acceptance	To check the correct position, current, resistance, temperature, helium level and pressure (done by the manufacturer)	X	
MRI3. MRI system acceptance	The MRI system is an electromagnetic device that must be checked according to national electromagnetic compliance legislation under the direction of the appropriate adviser and MR-physics expert.	X	X
	Acceptance tests will include those for performance as well as those for electromagnetic compliance and safety		
MRI4. MRI result accuracy	To check the accuracy of the MRAC results (i.e., fat and water separation)		X
MRI5. PET/MRI or image registration	To check that PET and MRI data are accurately superimposed for attenuation correction and image fusion and reporting		X

Results to be compared with manufacturers specifications, Ref = additional performance tests. The results provide reference data and reference values for future quality control (adapted from [15])

neurologic and cardiologic PET/MRI imaging which emerged from our experience after running the system for about 12 months. The combination of diagnostic MRI protocols with simultaneous PET acquisition is robust and standard in most cases [18–20]. Therefore, the present section focuses on the more challenging protocols.

Oncology (whole body) protocols

These protocols were designed to avoid intervention prior and during the procedure and to cover a large area of the body in a short time. For this purpose, the top of the patient's head is used as the reference position in the axial direction, and the bed positions and their MRI fields-of-View (FOVs) are adjusted to image a maximal area below this reference line. In this way, the head is always fully covered at the top of the resulting datasets, and no manual shifting of the whole block of bed positions in the axial direction is required during planning. Accordingly, the positions and FOVs in the anterior-posterior direction are adjusted in the MR protocols so that a maximal area above the patient table, suitable for most patients, is measured.

The whole-body protocol is initiated by a localizer with continuously moving table. Subsequently, each bed position is measured by a 3–5-min PET scan. During each PET scan, a transverse half-Fourier acquisition single-shot

Table 2 Basic procedures for quality control of a hybrid PET/MRI system (adapted from [17])

Routine QC tests for PET/MRI systems
Equipment type: coincidence, scintillator APD-detector system integrated with an MRI system

Test	Purpose	Frequency	Comments
PET1. Physical inspection	To check gantry covers in tunnel and patient handling system	Daily	Inspect for mechanical and other defects that may compromise safety of patient or staff
PET2. Daily QC	To test proper functioning of detector modules and check the calibration factor from image voxel intensity to true activity concentration	Daily	To be performed with the ^{68}Ge cylinder that comes with the system
PET3. Uniformity	To estimate axial uniformity across image planes 1-[max] by imaging a uniformly-filled phantom	After maintenance/ new setups/ normalization	Also to be performed after software upgrade or changes. The phantom could be a 20 cm diameter ^{68}Ge cylinder, or a re-fillable cylinder with ^{18}F covering more than (5 cm at each end) the whole axial field of view
PET4. Normalization	To determine system response to activity inside the FOV	Variable (at least 6-Monthly)	Frequency of test depends on system reliability and stability (see test PET2) and service; must be performed after firmware upgrade and hardware service
PET5. Calibration	To determine calibration factor from image voxel intensity to true activity concentration	Variable (at least 6-Monthly)	Must follow a new normalization. Follow the manufacturer's procedures
PET6. Spatial resolution	To measure spatial resolution of point source in sinogram and image space	Yearly	Use a ^{18}F-point source (non-standard) or linear source
PET7. Sensitivity	To measure the volume response of the system to a source of given activity concentration	Monthly	Perform according to NEMA NU2 standards with a set of sleeved rod sources [16]. An alternative method is given in NEMA-NU2 1994
PET8. Image quality	Hot and cold spot image quality of standardized image quality phantom	Yearly	According to NEMA NU2 image quality test [16]; required after system installation, not mandatory during clinical operation
MRI1. μ-map	To visually check the μ-map quality that is calculated and segmented out of fat and water MR images	After every study	Correct separation of water and fat images and the calculated μ-map. Correct composing of the μ-map of every bed position
MRI2. MRI-alignment	To determine 3D alignment of PET and MRI field-of-view	After major service	Manufacturer provides alignment phantom and ^{68}Ge-line sources
MRI3. MRI-performance	MR stability and resonance frequency	Weekly	Stability test advisable for fMRI [37], Fig. 4

turbo-spin-echo (HASTE) sequence (TE = 90 ms), transverse diffusion-weighted imaging (b = 800 s/mm^2) and a coronal turbo inversion recovery magnitude (TIRM) sequence (TI = 220 ms) is applied. In the bed position of the thorax, a respiratory navigator is placed manually on the diaphragm and used for the MR acquisition. Depending on the patient's size a scan of the whole body-trunk can thus be done within 20–30 min.

A slightly modified whole-body protocol is used for pediatric patients where a transverse TIRM sequence is used instead of the HASTE sequence and a belt is used for respiratory gating.

Brain protocols

Several brain imaging protocols are created "on the fly" by combining a routine diagnostic MRI protocol with a simultaneous PET acquisition [21]. One challenging protocol for simultaneous PET and MRI of the brain represents the combined perfusion PET with ^{15}O-Water and dynamic susceptibility contrast MRI. After production of $[^{15}O]O_2$ by the cyclotron and subsequent conversion to $[^{15}O]$ water, a vial filled with about 10 GBq $[^{15}O]$ water is transported in shielded containers via a pneumatic tube mail system. In our case, the transport takes approximately

210 s from radiochemistry to PET/MRI facility. For patients, the activity is measured before injection, which takes about another 2 min. Tracer injection is performed manually, and the venous line is afterwards flushed with saline solution by a power injector. After injection, the remaining radioactivity in the vial and syringe are assayed and decay-corrected. With this setup, a radioactive dose of roughly 600–1,000 MBq can be injected.

The PET/MRI preparation scans (MRAC, shimming, etc.) are performed during the transport of the vial so that the simultaneous dynamic PET and MRI scans can be started immediately upon injection. While the PET data is acquired in list mode, an MRI contrast agent (Gadovist, Bayer, Leverkusen, Germany) is injected shortly after the [^{15}O]water. The resulting dynamic susceptibility contrast is measured with a single-shot EPI sequence (TE = 28 ms, TR = 2,000 ms) to calculate maps of relative cerebral blood volume, flow and transit time.

Prior to the injections, a set of anatomic MRI scans are performed, including T1-, T2- and diffusion-weighted sequences, susceptibility-weighted imaging, fluid-attenuated inversion recovery, arterial spin labeling for additional perfusion measurements, and a time-of-flight angiography. Moreover, a post-contrast T1-weighted turbo-spin-echo sequence is acquired after the injections.

Cardiology protocols

After placing an initial MRI localizer to center the PET volume on the heart, PET acquisition is started in list mode. Meanwhile, several localizer scans and a frequency scout are executed to position and adjust the true fast imaging with steady-state precession (SSFP) cine scans, which is of special importance at higher field strengths [22, 23]. During the PET acquisition, several static or dynamic cardiac MR (CMR) sequences can be performed. As long as no combined respiratory CMR and cardiac PET gating is available, the image fusion of an MR data acquisition in the end-expiratory phase shows reasonable results. Nevertheless, even in simultaneously acquired cardiac PET and MRI data, data registration is necessary. With regard to image fusion the acquisition of ECG-gated 3D data sets should be favored in comparison to 2D data sets. For simple anatomical or viability studies, a static 3D Gradient Echo (GRE) sequence acquired during end-diastole is usually adequate. For viability assessment, 3D inversion-recovery gradient echo (IR-GRE), but also 3D phase sensitive inversion recovery (PSIR) sequences, are available [24] and should be used if possible. For PET/MRI comparisons of volumetric or functional evaluations, a stack of ECG-gated SSFP sequences in short-axis or transverse orientation covering the whole left and right ventricle is necessary. The PET data is reconstructed in triggered mode,

yielding 16 gated images. The functional, volumetric and viability assessment should initially be performed separately for PET and MRI, before the evaluation of the fused data sets is carried out.

Selected problems and approaches

From the experience which we were able to gather in the first year of use, we observe stable functionality of the system hardware. Also, the software is fully integrated in one package that runs on the system console for controlling the system and basic processing of acquired data. We want to share our first experiences with two topics that—in terms of quantitative PET measurements—are of essential importance.

Attenuation correction

One of the most important points is the AC of the PET emission data. Since MRI cannot directly yield μ-maps, a
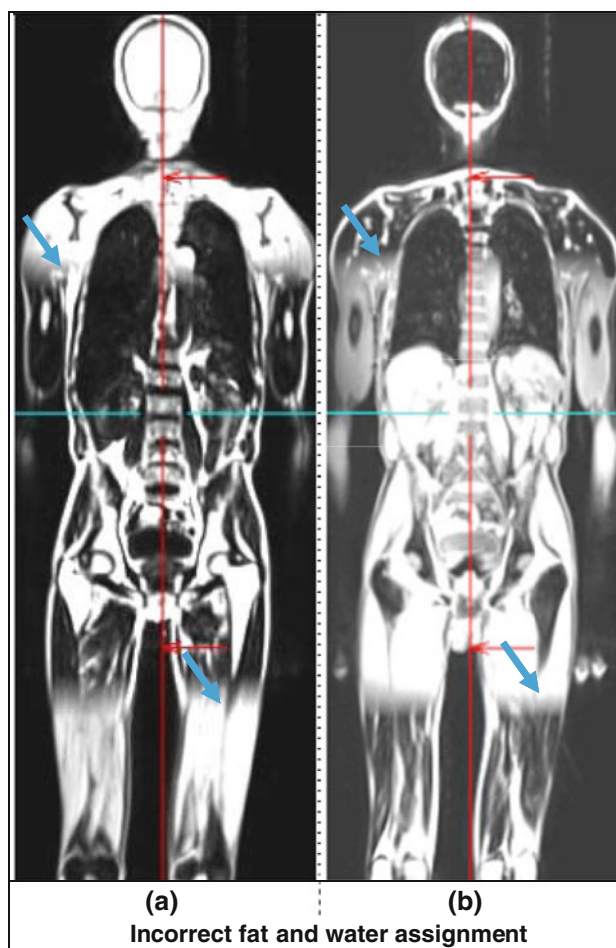
Fig. 5 Incorrect assignment of fat (**a**) and water (**b**) in the MRAC images of the *lower* and *upper* bed positions which may lead to an incorrect μ-map

two-point DIXON sequence is used to yield fat and water images from which a μ-map is estimated [25, 26]. This approach suffers from the fact that, especially in peripheral body regions, bone cannot be segmented and, thus, considered adequately. Moreover, the result of the AC-sequence must be checked visually for correct separation of fat and water images and composing of the bed positions in case more than one bed position was acquired (Table 2). An example of a faulty composition of bed-positions is shown in Fig. 5. Finally, the derived μ-map is to be visually checked for correct segmentation into water (soft tissue), air, lung tissue and fat. If this segmentation is faulty, and wrong attenuation coefficients are assigned to tissues, the interaction of the 511 keV gamma rays with the tissue during their penetration through the body (attenuation) cannot be considered adequately. This check is mandatory since, if the AC failed due to a faulty μ-map, wrong activity concentrations are assigned to voxels of the PET images and they cannot be used for quantification (i.e., Bq/ml or SUV measures). Examples of an incorrect segmentation are shown by Keller et al. [27], who gives a more in-depth insight about possible image artifacts from MR-based AC.

Here, the whole volume of the lung is not recognized as lung tissue. Some volume close to the diaphragm is obviously considered to be air. This fact projects into the AC-PET as underestimation of the activity content in that part of the lung. However, it is recommended in every case to incorporate the NAC PET images in the reporting of the study. We measured a brain phantom (HOFFMANN-phantom) filled with about 25 MBq of [18F]FDG mixed with human serum albumin to prevent sticking on the phantom inner wall and surfaces, and compared the results to measurements of the same phantom in a Biograph16 PET/CT system and ECAT HR$^+$ standalone PET system. The PET-volumes were co-registered, and activity profiles in the NAC-images were derived as displayed in Fig. 6. If the profiles through the NAC images are visually compared, there is good agreement among the different systems. Since, with this phantom, there is no fat in the FOV, and acrylic glass does not return an MR-signal, the segmentation of the μ-map may fail. Thus, a more quantitative comparison of the AC-images of that phantom may not be representative.

There are some other approaches than the DIXON sequence to yield MRI based μ-maps for the AC of the PET [26–32]. These methods, however, are not yet widely
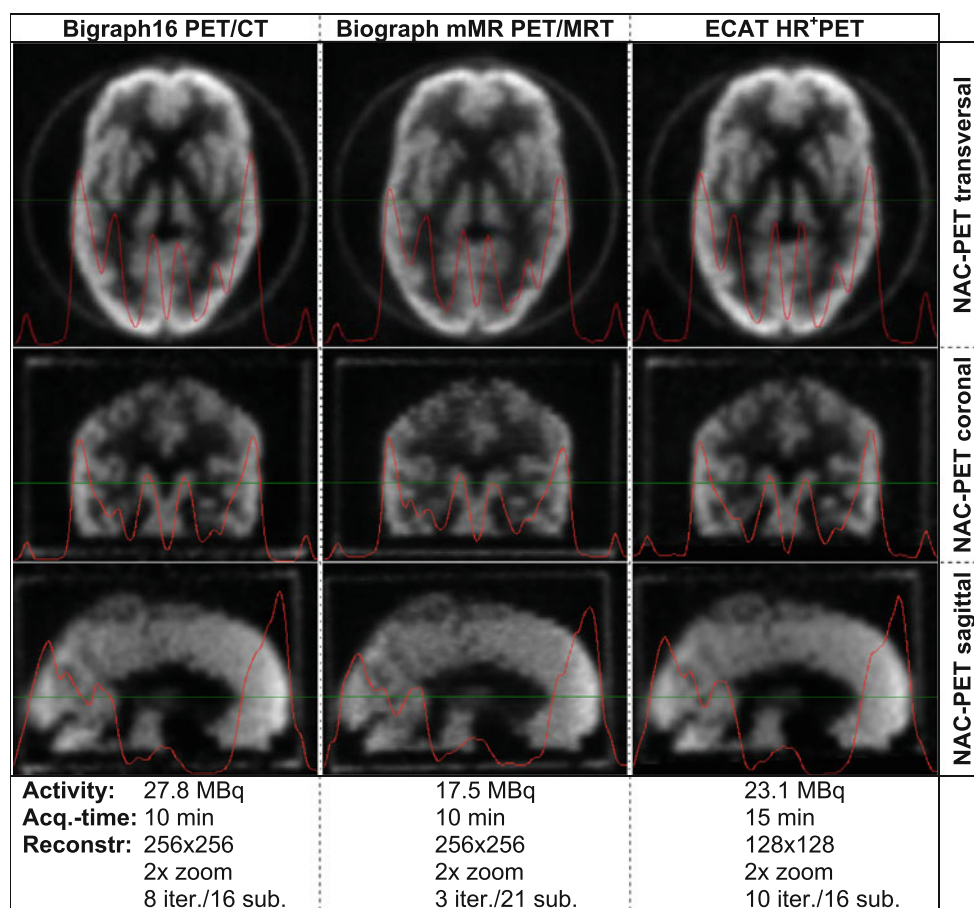

Fig. 6 Results of measurements of a HOFFMANN brain phantom on the Biograph mMR, a Biograph16 PET/CT and a ECAT HR$^+$ (all SIEMENS Healthcare). The *red line* shows the activity profile along the *green line*

available and also require further testing and regulatory approval for clinical use. Once there is enough published evidence that these methods, possibly in combination with the DIXON approach [33], are superior to the present method, they should be included by the manufacturers as described.

Arterial input function measurement

An arterial input function (AIF, radioactivity concentration in arterial blood as a function of time post injection) represents a prerequisite if absolute quantification of the pathophysiological or pathobiochemical processes measured by PET by means of kinetic modeling is intended. To characterize the in vivo behavior and metabolism of a tracer, a full kinetic modeling is necessary. For this approach, measurement of the AIF is mandatory. For obtaining an AIF, arterial blood sampling, either at certain time-points by hand or continuously by automated devices still represents the "gold standard" [34]. As a potential alternative in the future, the AIF can also be measured using the inherently co-registered PET and MRI data. This would overcome the need to do it manually and the risk of adverse events in relation to arterial cannulization or the need of having MR-compatible automated blood sampling devices available. To demonstrate the capabilities of integrated PET/MRI in this regard, in a simultaneous dynamic $[^{18}F]$ FDG brain PET/MRI, we have determined the time-dependent activity concentration in a major neck artery, fully automated. This artery was identified by an MRI-based, high-resolution ($0.52 \times 0.52 \times 0.7$ mm^3) time-of-flight (TOF) angiography covering the neck (Fig. 7a). A binary mask was created containing the one-hundred brightest voxels in the TOF data. This procedure gave a good outline of arteries, as verified by visual inspection. Subsequently, the binary mask was aligned to the PET voxels (Fig. 7b). In this way, an arterial partial volume coefficient, ε, was assigned to each PET voxel reflecting the fractional overlap with the TOF mask. To account for partial volume effects (PVEs) and the extended point-spread function (PSF) of the system, the activity was deconvolved assuming the superposition resulting from two compartments: the volume within the arteries and the volume in the vicinity outside. The corresponding geometric transformation matrix (GTM) [35] was calculated based on the known PSF of the system [26] considering all voxels with a non-zero ε. Finally, inverting the GTM and applying the inverse to the activity pattern of each time frame of the PET-data yielded the PVE-corrected AIF, as shown in Fig. 7c. This graph also shows that the image-derived AIF resembles the shape of a typical AIF [36]. Differences in peak magnitude and at later times may be attributed to the finite temporal resolution and an imperfect partial-volume correction (e.g., due to patient motion).
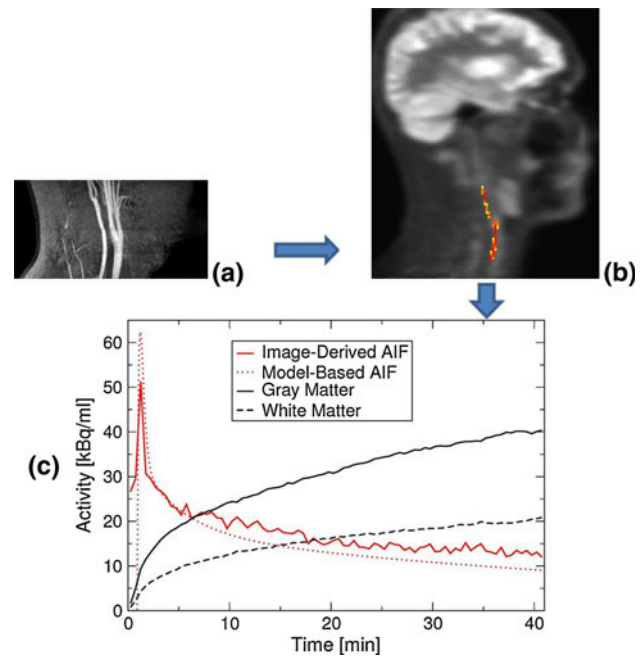
Fig. 7 Employing a high-resolution ($0.52 \times 0.52 \times 0.7$ mm^3) time-of-flight (*TOF*) angiography sequence covering the neck (**a**) registered to the corresponding dynamic PET data with superimposition of the *color-coded* partial volume coefficient of the artery (**b**) and MRI-based AIF calculation of FDG uptake (**c**). For comparison/validation, a model for the AIF is also shown (4th order model [36])

Preparatory, commissioning, operational and recurrent costs

As described, prior to installation an extensive program of preparatory constructional work is necessary to prepare the facility to house a combined PET/MRI system. Based on our experience, an additional 20–25 % of the investment costs for the system itself are required for this purpose. Moreover, a MR-contrast agent pump, anesthesia equipment, general syringe pumps, systems for neural activation, as well as an automated blood sampling system to draw blood samples, cause additional expenses at commissioning, in the order of about 5-10 % of the investment cost. Further, recurrent expenditure for personnel, energy and cooling capacity consumption, data capacity, and, after the warranty by the manufacturer has expired, also for a maintenance contract need to be considered (about 10 % of the system investment cost).

Conclusion

In case of an integrated PET/MRI system, thorough and anticipatory technical and organizational planning and financial budgeting at local and regional level prior to the installation is required. Providing this, it is possible to

setup and run such a system without major restrictions. Overall, the most important precondition for successful implementation of combined PET/MRI in an integrated research and clinical setting is the directed interdisciplinary cooperation between all partners, and in all phases of the project; from planning, through commissioning and into its initial and early phases of use.

References

1. European Parliament and Council (1996) Directive 96/29/EUR-ATOM Laying down basic safety standards for the protection of health of workers and the general public against the dangers arising from ionizing radiation. Off J Eur Un L 159:1

2. European Parliament and Council (1997) Directive 97/43/EUR-ATOM On health protection of individuals against dangers of ionizing radiation in relation to medical exposure. Off J Eur Un L 180:22

3. Strahlenschutzverordnung vom 20. Juli 2001 (BGBl. I S. 1714; 2002 I S. 1459), die zuletzt durch Artikel 5 Absatz 7 des Gesetzes vom 24. Februar 2012 (BGBl. I S. 212) geändert worden ist

4. European Commission Public Health (2009) Manufacture of Radiopharmaceuticals, The Rules Governing Medicinal Products in the European Union, EU Guidelines to Good Manufacturing Practice, Medicinal Products for Human and Veterinary Use. EudraLex, vol 4, Annex 3

5. European Commission Public Health (2010) Investigational Medicinal Products, The Rules Governing Medicinal Products in the European Union; EU Guidelines to Good Manufacturing Practice, Medicinal Products for Human and Veterinary Use. EudraLex, vol 4, Annex 13

6. Arzneimittelgesetz in der Fassung der Bekanntmachung v. 12. Dezember 2005 (BGBl I S. 3394), das zuletzt durch Artikel 13 des Gesetzes vom 22. Dezember 2011 (BGBl I S. 2983) geändert worden ist

7. European Parliament and Council (1993) Directive 93/42/EEC Concerning medical devices. Off J Eur Un L 169:1

8. European Parliament and Council (2004) Directive 2004/40/EC On the minimum health and safety requirements regarding the exposure of workers to the risks arising from physical agents (electromagnetic fields) Off Journ Eur Un L 159:1

9. Medizinproduktegesetz in der Fassung der Bekanntmachung vom 7. August 2002 (BGBl. I S. 3146), das zuletzt durch Artikel 13 des Gesetzes vom 8. November 2011 (BGBl. I S. 2178) geändert worden ist

10. National Electrical Manufacturers Association (1996) DICOM Supplement 12, Addendum to part 3, positron emission tomography image objects. http://dicom.nema.org/

11. National Electrical Manufacturers Association (2011) DICOM information object definitions. Part 3, http://dicom.nema.org/

12. National Electrical Manufacturers Association (2011) DICOM media storage and file format for media interchange. Part 10, http://dicom.nema.org/

13. National Electrical Manufacturers Association (2011). DICOM service class specifications. Part 4, http://dicom.nema.org/

14. Wikimedia Foundation (2012) Free software open source wiki package written in PHP. http://www.mediawiki.org/

15. Busemann-Sokole E, Plachcinska A, Britten A, EANM Physics Committee (2010) Acceptance testing for nuclear medicine instrumentation. Eur J Nucl Med Mol Imaging 37(3):672–681

16. National Electrical Manufacturers Association (2007) Performance measurements of positron emission tomographs. NEMA Standards Publication NU 2-2007, Rosslyn, VA

17. Busemann-Sokole E, Plachcinska A, Britten A, EANM Physics Committee (2010) Routine quality control recommendations for nuclear medicine instrumentation. Eur J Nucl Med Mol Imaging 37(3):662–671

18. Drzezga A, Souvatzoglou M, Eiber M, Beer A, Fürst S, Martinez-Möller A, Nekolla SG, Ziegler SI, Ganter C, Rummeny E, Schwaiger M (2012) First clinical experience with integrated whole-body PET/MR: comparison to PET/CT in patients with oncologic diagnoses. J Nucl Med 53:1–11

19. Schwenzer NF, Schmidt H, Claussen CD, Whole-body MR/PET (2012) Applications in abdominal imaging. Abdom Imaging 37(1):20–28

20. Ratib O, Beyer T (2011) Whole-body hybrid PET/MRI: ready for clinical use? Eur J Nucl Med Mol Imaging 38:992–995

21. Schwenzer NF, Stegger L, Bisdas S, Schraml C, Kolb A, Boss A, Müller M, Reimold M, Ernemann U, Claussen CD, Pfannenberg C, Schmidt H (2012) Simultaneous PET/MR imaging in a human brain PET/MR system in 50 patients-current state of image quality. Eur J Radiol. doi:10.1016/j.ejrad.2011.12.027

22. Gutberlet M, Noeske R, Schwinge K, Freyhardt P, Felix R, Niendorf T (2006) Comprehensive cardiac magnetic resonance imaging at 3.0 Tesla: feasibility and implications for clinical applications. Invest Radiol 41(2):154–167

23. Gutberlet M, Schwinge K, Freyhardt P, Spors B, Grothoff M, Denecke T, Lüdemann L, Noeske R, Niendorf T, Felix R (2005) Influence of high magnetic field strengths and parallel acquisition strategies on image quality in cardiac 2D CINE magnetic resonance imaging: comparison of 1.5 T vs. 3.0 T. Eur Radiol 15(8):1586–1597

24. Kellman P, Larson AC, Hsu LY, Chung YC, Simonetti OP, McVeigh ER, Arai AE (2005) Motion-corrected free-breathing delayed enhancement imaging of myocardial infarction. Magn Reson Med 53(1):194–200

25. Eiber M, Martinez-Möller A, Souvatzoglou M, Holzapfel K, Pickhard A, Löffelbein D, Santi I, Rummeny EJ, Ziegler S, Schwaiger M, Nekolla SG, Beer AJ (2011) Value of a Dixon-based MR/PET attenuation correction sequence for the localization and evaluation of PET-positive lesions. Eur J Nucl Med Mol Imaging 38(9):1691–1701

26. Delso G, Furst S, Jakoby B, Ladebeck R, Ganter C, Nekolla SG, Schwaiger M, Ziegler SI (2012) Performance measurements of the Siemens mMR integrated whole-body PET/MR scanner. J Nucl Med 52:1–9

27. Keller SH, Holm S, Hansen AE, Sattler B, Andersen A, Klausen TL, Højgaard L, A Kjær A, Beyer T (2012) Image artifacts from MR-based attenuation correction in clinical, whole-body PET/MRI. Magn Reson Mater Phy. doi:10.1007/s10334-012-0345-4

28. Hofmann M, Steinke F, Scheel V, Charpiat G, Farquhar J, Aschoff P, Brady M, Schölkopf B, Pichler BJ (2008) MRI-based attenuation correction for PET/MRI: a novel approach combining pattern recognition and atlas registration. J Nucl Med 49:1875–1883

29. Hofmann M, Pichler BJ, Schölkopf B, Beyer T (2009) Towards quantitative PET/MRI a review of MR-based attenuation correction techniques. Eur J Nucl Med Mol Imaging 36(Suppl 1):S93–S104

30. Hofmann M, Bezrukov I, Mantlik F, Aschoff P, Steinke F, Beyer T, Pichler BJ, Schölkopf B (2011) MRI-based attenuation correction for whole-body PET/MRI: quantitative evaluation of segmentation- and atlas-based methods. J Nucl Med 52:1392–1399

31. Martinez-Möller A, Souvatzoglou M, Delso G, Bundschuh RA, Chefd'hotel C, Ziegler SI, Navab N, Schwaiger M, Nekolla SG (2009) Tissue classification as a potential approach for attenuation correction in whole-body PET/MRI: evaluation with PET/CT data. J Nucl Med 50:520–526

32. Schulz V, Torres-Espallardo I, Renisch S, Hu Z, Ojha N, Börnert P, Perkuhn M, Niendorf T, Schäfer WM, Brockmann H, Krohn T, Buhl A, Günther RW, Mottaghy FM, Krombach GA (2011) Automatic, three-segment, MR-based attenuation correction for whole-body PET/MR data. Eur J Nucl Med Mol Imaging 38(1):138–152

33. Berker Y, Franke J, Salomon A, Palmowski M, Donker HC, Temur Y, Mottaghy FM, Kuhl C, Izquierdo-Garcia D, Fayad ZA, Kiessling F, Schulz V (2012) MRI-based attenuation correction for hybrid PET/MRI systems: a 4-class tissue segmentation technique using a combined ultrashort-echo-time/Dixon MRI sequence. J Nucl Med 53(5):796–804

34. Zanotti-Fregonara P, Maroy R, Comtat C, Jan S, Gaura V, Bar-Hen A, Ribeiro MJ, Trébossen R (2009) Comparison of 3 methods of automated internal carotid segmentation in human brain PET studies: application to the estimation of arterial input function. J Nucl Med 50(3):461–467

35. Rousset OG, Yilong M, Evans AC (1998) Correction for partial volume effects in PET: principle and validation. J Nucl Med 39:904–911

36. Feng D, Huang S-C, Wang X (1993) Models for computer simulation studies of input functions for tracer kinetic modeling with positron emission tomography. Int J Biomed Comput 32:95–110

37. Koschewski F (2011) PET-MRT am Universitätsklinikum Leipzig. Telekine TV Productions, www.youtube.com/watch?v=cq9sYYqtU5w

38. Friedman L, Glover GH (2006) Report on a multicenter fMRI quality assurance protocol. J Magn Reson Imaging 23:827–839

2.2. Erste klinische Ergebnisse der simultanen 18F-FDG PET/MRT im Vergleich zur 18F-FDG PET/CT bei Patienten mit Kopf-Hals-Tumoren

An vielen Einrichtungen fokussierten erste Untersuchungen auf Vergleiche des PET/MRT-Systems mit PET/CT-Systemen bezüglich der Genauigkeit in der Tumordetektion [69, 106, 121–129]. Nachdem die baulichen und gerätetechnischen Voraussetzungen gegeben waren und die Untersuchungsprotokolle für diverse Tumorfragestellungen gemeinsam festgelegt worden waren, wurden auch bei uns verschiedene Untersuchungen mit dieser Fragestellung durchgeführt. Bei Patienten mit Kopf-Hals-Tumoren erfolgte eine erste Auswertung zur Sensitivität und Spezifität anhand einer Gruppe von 17 Patienten [130]. Diese Gruppe war noch sehr heterogen und umfasste Patienten zum Primärstaging ebenso wie Patienten zur Rezidivsuche. Hier fand sich kein Unterschied bezüglich Sensitivität und Spezifität in der Tumordetektion zwischen PET/MRT und PET/CT. Der genannte Artikel wird als zweiter Teil der Habilitationsschrift eingefügt.

Kubiessa, Klaus; Purz, Sandra; Gawlitza, Matthias; Kühn, Axel; Fuchs, Jochen; Steinhoff, Karen Geva; Boehm, Andreas; Kluge, Regine; Sabri, Osama; *Stumpp, Patrick* (2014):
Initial clinical results of simultaneous 18F-FDG PET/MRI in comparison to 18F-FDG PET/CT in patients with head and neck cancer.
European journal of nuclear medicine and molecular imaging 41 (4), S. 639–648.

ORIGINAL ARTICLE

Initial clinical results of simultaneous ^{18}F-FDG PET/MRI in comparison to ^{18}F-FDG PET/CT in patients with head and neck cancer

K. Kubiessa · S. Purz · M. Gawlitza · A. Kühn · J. Fuchs ·
K. G. Steinhoff · A. Boehm · O. Sabri · R. Kluge ·
T. Kahn · P. Stumpp

Abstract

Purpose The aim of this study was to evaluate the diagnostic capability of simultaneous ^{18}F-fluorodeoxyglucose (FDG) positron emission tomography (PET)/MRI compared to ^{18}F-FDG PET/CT as well as their single components in head and neck cancer patients.

Methods In a prospective study 17 patients underwent ^{18}F-FDG PET/CT for staging or follow-up and an additional ^{18}F-FDG PET/MRI scan with whole-body imaging and dedicated examination of the neck. MRI, CT and PET images as well as PET/MRI and PET/CT examinations were evaluated independently and in a blinded fashion by two reader groups. Results were compared with the reference standard (final diagnosis determined in consensus using all available data including histology and follow-up). Sensitivity, specificity, positive predictive value (PPV) and negative predictive value (NPV) were calculated.

Results A total of 23 malignant tumours were found with the reference standard. PET/CT showed a sensitivity of 82.7 %, a specificity of 87.3 %, a PPV of 73.2 % and a NPV of 92.4 %. Corresponding values for PET/MRI were 80.5, 88.2, 75.6 and 92.5 %. No statistically significant difference in diagnostic capability could be found between PET/CT and PET/MRI. Evaluation of the PET part from PET/CT revealed highest sensitivity of 95.7 %, and MRI showed best specificity of 96.4 %. There was a high inter-rater agreement in all modalities (Cohen's kappa 0.61–0.82).

Conclusion PET/MRI of patients with head and neck cancer yielded good diagnostic capability, similar to PET/CT. Further studies on larger cohorts to prove these first results seem justified.

Keywords Simultaneous PET/MRI · Head and neck cancer · PET/CT

K. Kubiessa and S. Purz contributed equally to this work.

K. Kubiessa · M. Gawlitza · A. Kühn · J. Fuchs · T. Kahn ·
P. Stumpp (✉)
Department of Diagnostic and Interventional Radiology, University Hospital of Leipzig, Liebigstrasse 20, 04103 Leipzig, Germany
e-mail: patrick.stumpp@medizin.uni-leipzig.de

S. Purz · K. G. Steinhoff · O. Sabri · R. Kluge
Department of Nuclear Medicine, University Hospital of Leipzig, Liebigstrasse 18, 04103 Leipzig, Germany

A. Boehm
ENT Department, University Hospital of Leipzig, Liebigstrasse 10-14, 04103 Leipzig, Germany

Introduction

Computed tomography (CT), magnetic resonance imaging (MRI) and ^{18}F-fluorodeoxyglucose (FDG) positron emission tomography with combined CT (PET/CT) are well-established diagnostic imaging tools for investigation of initial staging and post-treatment settings in head and neck cancer [1–6].

The new hybrid imaging modality PET/MRI is expected to be of special use in body regions with difficult anatomy and in organs where the inherent soft tissue contrast of MRI is superior to that of CT [7, 8]. One of these regions is the head and neck area, where MRI has the additional advantage of lower susceptibility to dental filling artefacts compared to CT [9]. A general advantage of PET/MRI over PET/CT is the lower radiation exposure due to the omission of CT, especially if contrast-enhanced CT is performed. Although this might be considered to be of lower importance in tumour patients as their life expectancy is generally reduced, this effect should not be underrated, especially in younger patients who need follow-up studies.

 Springer

Especially due to the high mobility and the anatomical complexity of the head and neck region, performing simultaneous PET/MRI may result in a better alignment of both imaging data in comparison to retrospectively fused PET and MR imaging data. This is because patient movements that can occur during patient repositioning are minimized when using two separate or sequential examination approaches [10].

Two feasibility studies have already shown the possibility of PET/MRI in head and neck cancer imaging. One of them was performed with a prototype PET insert into a 3 T MRI [11], and the other one was done on a sequential PET/MRI system, showing that PET and MR image quality were not impaired [12].

This report presents the first results of a prospective clinical study, in which PET/CT and integrated PET/MRI were used to evaluate patients with suspected or known cancer of the head and neck region. Diagnostic capability of the two combined modalities as well as of the three independent components MRI, CT and PET was compared, when the same subjects were examined by PET/CT and PET/MRI on the same day.

Materials and methods

Patients

This prospective study was approved by the local Ethics Committee and all patients gave their written informed consent. A total of 22 consecutive head and neck cancer patients were investigated. Inclusion and exclusion criteria for the analysis are presented in Table 1.

Of the 22 patients, 17 fulfilled the inclusion criteria, among them 7 patients for primary staging and 10 patients for

Table 1 Inclusion and exclusion criteria

Inclusion criteria	Exclusion criteria
Age>18 years	Contraindications for iodinated CT contrast medium
Written informed consent	Pregnancy
Suspected primary head and neck tumour or cancer of unknown primary	Pacemaker or magnetic implants/ devices
Suspicion of residual tumour or recurrent tumour growth after therapy	Incomplete MRI examination without dedicated head and neck protocol
Routine follow-up after therapy	Incomplete MRI examination without whole-body exam if there were relevant findings outside the head and neck region
Blood glucose level<10 mmol/l at the time of the examination	

restaging from 6 months to 4 years after therapy (3 after radiochemotherapy, 2 after surgery and radiochemotherapy, 2 after surgery, 1 after surgery and radiotherapy, 1 after surgery and chemotherapy and 1 after chemotherapy). Of these 17 patients, 4 were female, and their mean age was 60 years (range 42–78 years). All patients underwent an ^{18}F-FDG PET/CT and subsequently a 3 T simultaneous PET/MRI on the same day without further radiopharmaceutical administration.

PET/CT acquisition

All patients underwent an ^{18}F-FDG PET/CT protocol using a Siemens Biograph 16 PET/CT scanner (Siemens Medical Solutions, Erlangen, Germany). Before the investigation, patients fasted for at least 6 h. After administration of 275–445 MBq of ^{18}F-FDG depending on body weight (5 MBq/kg) and a median uptake time of 90 min, the whole-body PET data were acquired with 3 min per bed position. Contrast-enhanced CT scan was performed after intravenous injection of 120 ml contrast agent (Imeron 300, Bracco Imaging, Constance, Germany) with a collimation of 16×0.75 mm, a tube voltage of 120 kVp and the use of angular and longitudinal dose modulation (CARE Dose4D®, Siemens Medical Solutions, Erlangen, Germany). Patients were placed in the supine position.

Depending on the clinical situation and their inclusion in radiochemotherapy studies patients underwent different (PET)/CT protocols:

– Eight patients with clinically proven tumour recurrence or suspicion of metastasized tumour were placed with their arms up and received a contrast-enhanced scan from skull base to the groins during free breathing (150 mAs per protocol), followed by a low-dose chest CT during inspiration (50 mAs per protocol).
– Nine patients with clinically suspected local tumour only or high-risk patients (former head and neck cancer International Union Against Cancer stage III or IV) underwent a dedicated CT of the neck (150 mAs per protocol, patient positioning with arms down). As three of these nine patients already had a recent CT of the chest, only six underwent an additional full-dose chest CT during inspiration (100 mAs per protocol) after a change in arm positioning. All nine received a low-dose CT scan from skull base to the groins for attenuation correction of the PET data.

PET/MRI acquisition

Subsequently, PET/MR imaging was performed on the integrated PET/MR scanner (Siemens Biograph mMR, Siemens Healthcare, Erlangen, Germany). The examination protocol

developed at our institution combined a whole-body scan with a dedicated examination of the head and neck area which resulted in an examination time of 70 min and was used for primary staging, follow-up examinations and tumour search in patients with cancer of unknown primary (CUP). Patients were placed in the supine position with arms down. Specially designed coils were placed on the patient: one head and neck coil and four body phased array coils which together covered the region from skull to thigh.

Then, whole-body PET/MR imaging without contrast medium was performed in six bed positions: head, neck, thorax, abdomen, pelvis and proximal thighs (for details see Table 2). This investigation already included a coronal Dixon-volumetric interpolated breath-hold examination (VIBE) sequence for attenuation correction. Chosen b values for diffusion-weighted imaging (DWI) were 0 s/mm^2 to allow fast scanning without the need for an additional gradient and 800 s/mm^2, in concordance with other whole-body DWI studies [13–15]. The diffusion-sensitizing gradients were applied in all three orthogonal directions. These MRI measurements took 5 min per bed position, during which PET data were acquired. Compared to PET/CT this longer acquisition time leads to a higher count rate and slightly better image quality of PET/MRI, although this effect was not separately evaluated in this study. Respiratory triggering was used in the bed positions of thorax and abdomen only, other bed positions were scanned during free breathing. Subsequently, a dedicated MRI of the neck was performed (for details see Table 3), which included a coronal Dixon-VIBE sequence for attenuation correction. For contrast-enhanced MR imaging, an axial dynamic contrast-enhanced T1-weighted fast low-angle shot (FLASH) sequence with 40 measurements over 4 min was performed immediately during intravenous administration of a single dose of 0.1 mmol/kg gadobutrol (Gadovist®, Bayer HealthCare, Leverkusen, Germany) at a rate of 3 ml/s and flushing with 10 ml of normal saline using a power injector (Spectris Solaris, Medrad/Bayer HealthCare, Leverkusen Germany). A dedicated evaluation of tumour perfusion was not performed in this study. Exemplary images of the neck protocol are shown in Fig. 1.

Image analysis

The PET/CT and PET/MRI data sets were evaluated on dedicated workstations (PET/CT and PET/MRI: syngo.via, Siemens Healthcare, Erlangen, Germany; CT only and MRI only: MagicView 1000, Siemens Medical Solutions, Erlangen, Germany; PET only: Hermes Hybrid Viewer, Hermes Medical Solutions, Stockholm, Sweden).

The reference standard was defined as the final collective diagnosis determined in consensus between an experienced board-certified radiologist, specialized in head and neck radiology, an experienced board-certified nuclear medicine physician and a head and neck surgeon. They had access to all relevant data including medical history, prior examinations, results of panendoscopy or surgery as well as all imaging data (PET/CT and PET/MRI). Histopathological correlates following surgery were available for six patients. Histological diagnosis after biopsy could be used in five patients. In the remaining six patients follow-up examinations showed tumour progression in three (two with PET/CT and one with CT), tumour regression after chemotherapy in one and confirmed the absence of tumour in two patients (CT). Follow-up time ranged between 2 and 14 months.

For image interpretation, the investigation of the CT only and MRI only was done independently and in a blinded fashion by two radiologists (radiologists A and B) with a 4-week gap between the readings of MRI and CT. The readers only took into account all images from MRI and CT without the knowledge of any findings from the corresponding PET component. Evaluation of MRI included all morphological sequences and DWI.

A lesion was considered malignant if there was a visible soft tissue mass, atypical contrast enhancement or central necrosis in a mass on CT. Lymph nodes were considered malignant if they were enlarged in their short axis above 1.5 cm, had a round shape or an unusually strong contrast enhancement. With regard to MRI, decreased diffusion in a circumscribed region on the apparent diffusion coefficient (ADC) map was also considered a sign of malignancy as well as hyperintensity on T2-weighted images.

Table 2 MRI sequence parameters for one bed position used in simultaneous whole-body PET/MRI

Sequence	Orientation	TR (ms)	TE (ms)	FA (°)	No. of slices	Slice thickness (mm)	FOV read (mm)	Resolution matrix (mm)	Voxel size (mm)	TA (min)
T1w 3D Dixon-VIBE	Coronal	3.6	1.23	10	128	2.6	500	500 × 328	4.1×2.6×2.6	0:19
T2w HASTE	Axial	800	89	120	40	4	450	450×315	1.8×1.4×4.0	0:32
T2w TIRM	Coronal	2,090	47	120	40	5	500	500×350	3.1×1.6×5.0	1:00
EPI fs DWI	Axial	6,800	73	NA	30	6	450	450×338	4.3×3.5×6.0	1:15

TR repetition time, *TE* echo time, *FA* flip angle, *FOV* field of view, *TA* acquisition time, *fs* fat saturated, *VIBE* volumetric interpolated breath-hold examination, *HASTE* half-Fourier acquisition single-shot turbo spin-echo, *TIRM* turbo inversion recovery magnitude, *EPI* echo planar imaging, *DWI* diffusion-weighted imaging

Table 3 MRI sequence parameters used for dedicated simultaneous PET/MRI in the head and neck region

Sequence	Orientation	TR (ms)	TE (ms)	FA (°)	No. of slices	Slice thickness (mm)	FOV read (mm)	Resolution matrix (mm)	Voxel size (mm)	TA (min)
T1w 3D Dixon-VIBE	Coronal	3.6	1.23	10	128	2.6	500	500×328	4.1×2.6×2.6	0:19
T1w TSE	Axial	780	12	140	42	4	280	280×223	1.1×0.5×4.0	2:34
T2w fs TSE	Axial	5,640	105	140	42	4	280	280×223	0.8×0.5×4.0	4:15
T2w TIRM	Coronal	3,500	44	150	38	3	240	240×240	1.0×0.8×3.0	4:07
EPI fs DWI	Axial	8,620	73	NA	30	4	334	334×251	3.2×2.6×4.0	1:35
T1w 3D fs FLASH DCE	Axial	2.47	0.97	8	40	5	260	260×260	1.2×1.0×5.0	4:00
T1w fs TSE CE	Axial	996	12	140	42	4	280	280×223	1.1×0.5×4.0	3:16
T1w fs TSE CE	Coronal	817	19	150	38	3	280	280×195	1.0×0.6×3.0	3:20
T1w 3D fs VIBE CE	Axial	3.35	1.14	10	72	3	280	280×254	0.9×0.9×3.0	0:34

TR repetition time, *TE* echo time, *FA* flip angle, *FOV* field of view, *TA* acquisition time, *fs* fat saturated, *VIBE* volumetric interpolated breath-hold examination, *TSE* turbo spin echo, *TIRM* turbo inversion recovery magnitude, *EPI* echo planar imaging, *DWI* diffusion-weighted imaging, *FLASH* fast low-angle shot, *DCE* dynamic contrast enhanced, *CE* contrast enhanced

The evaluation of the PET part from PET/CT and PET/MRI was also performed independently and in a blinded fashion by two nuclear medicine physicians (nuclear physicians 1 and 2), without considering any diagnostic MRI or CT images. This was done with a 4-week gap between the analysis of the two PET parts, using the whole-body exam PET data. The PET data of the head and neck scan were only used for the three PET/MRI examinations without whole-body imaging. The semi-quantitative standardized uptake value (SUV$_{max}$) was used as a tool to supplement visual
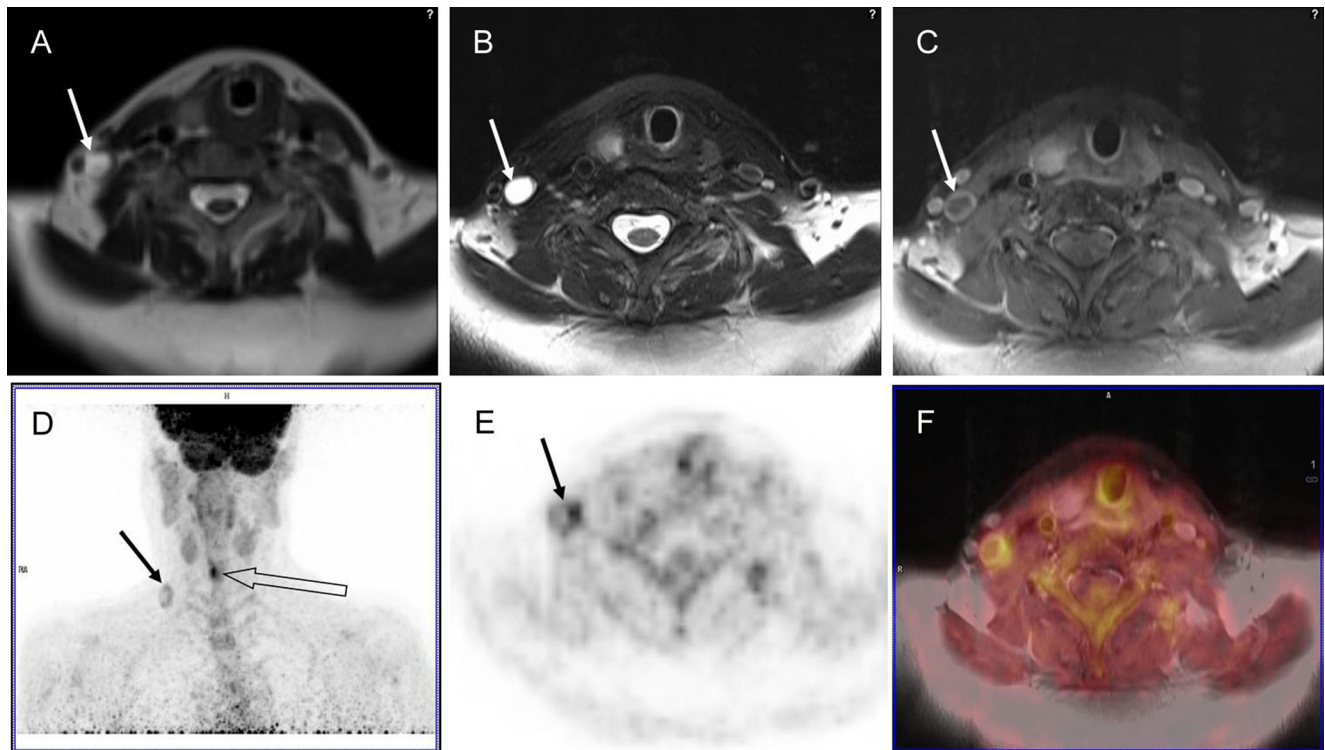
Fig. 1 A 52-year-old female patient with glottic carcinoma and a nodal metastasis at level V on the right side. Metastasis seen in all modalities. **a** T2-weighted HASTE image from whole-body MRI showing necrotic nodal metastasis (*arrow*). **b** Fat-saturated T2-weighted TSE image from dedicated neck MRI with the same metastasis better visualized (*arrow*). **c** Fat-saturated T1-weighted TSE post contrast with circular enhancement of the metastasis (*arrow*). **d** Maximum intensity projection (MIP) image of the ^{18}F-FDG PET with focally increased glucose metabolism in the vocal chord (*open arrow*) and in the outline contour of the mostly necrotic nodal metastasis (*arrow*). **e** Axial PET image in the region of the nodal metastasis (*arrow*). **f** Fused image of simultaneously acquired PET and T1-weighted TSE MR images

interpretation. Visual assessment of the PET images focused on the pattern and asymmetry of FDG distribution as well as contrast to background ratio.

Subsequently, PET/MRI and PET/CT were assessed independently, in a blinded fashion and in a randomized order by two reader groups, each composed of one radiologist and one nuclear physician (reader groups I and II). In these evaluations, all of the above-mentioned characteristics for malignant lesions of the combined modalities were used. Especially for lymph nodes, an intense and asymmetrical FDG uptake was regarded as a sign of malignancy, even in normal sized nodes. For one and the same reader there was always a 4-week gap between evaluation of the single and combined modalities.

Statistical analysis

For statistical analysis in comparison to the reference standard, evaluation was done on a lesion-by-lesion basis. Only the correct detection and classification as a malignant lesion was evaluated as positive. Failure in lesion detection, correct classification of a lesion as non-malignant or benign classification of a malignant lesion were each evaluated as negative. Thus statistical analysis was exclusively based on lesions that could be detected in at least one of the three imaging modalities.

Statistical assessment was based on sensitivity, specificity, positive predictive value (PPV) and negative predictive value (NPV) analysis of each multimodal imaging modality (PET/CT, PET/MRI) and each single part of the combined diagnostic tools (CT, MRI, PET). The McNemar test with Bonferroni correction for multiple testing was used to compare sensitivities, specificities, PPVs and NPVs between the different diagnostic modalities of a single investigator or within the same reader group (statistically significant difference in single test when $p < 0.0083$). Cohen's kappa coefficient was used to assess the inter-rater agreement between different observer groups within the corresponding single or combined diagnostic modality.

Results

All patients tolerated the PET/CT well. With regard to the PET/MRI study protocol, in three patients only dedicated sequences for the neck region were obtained and no whole-body protocol due to their constrained compliance. Another patient received his whole-body PET/MRI examination only from the liver region upwards to the head due to unknown technical problems in the two lower bed positions (MRI scans did not start, so there were no anatomical images and no possibilities to reconstruct attenuation-corrected PET images in this region). But in any case there were no relevant findings

in the uncovered body regions. All other 14 patients tolerated the whole PET/MRI protocol well.

In the study population the definitive diagnoses from the reference standard revealed 23 malignant findings. Of these, eight lesions were primary, residual or recurrent tumours. There were three carcinomas of the base of the tongue, two laryngeal carcinomas, one tonsillar carcinoma, one carcinoma of the oropharynx and one hypopharyngeal carcinoma. Furthermore, 15 foci of metastatic spread were diagnosed. In particular there were ten lesions with metastatic cervical or mediastinal lymph nodes, four pulmonary metastases and one metastasis in the chest wall. The size of the lesions ranged between 1.1 and 8.5 cm (mean 2.5 cm).

Besides these 23 positive findings, 55 benign, inflammatory or non-specific changes were established and classified as negative. These findings were rated as non-specific/inflammatory lymph nodes ($n = 23$), inflammatory/post-operative changes in pharynx, paravascular cervical space, chest and abdominal wall ($n = 16$), renal and hepatic cysts ($n = 5$), uterine fibroadenoma ($n = 2$), thyroid nodes ($n = 2$) and one case each of thrombosed carotid artery, pleomorphic adenoma, follicular nodular hyperplasia, lateral cleft branch cyst, discitis, silicoanthracosis and old focal cerebellar infarcts.

The findings of the different investigators are summarized in Table 4. In this study, PET/CT as well as PET/MRI reached comparable good specificity of 85.5–89.1 % for PET/CT and 81.8–94.5 % for PET/MRI and very good NPV of 90.7–94 % for PET/CT and 91.2–93.8 % for PET/MRI, respectively (see Fig. 2). Both combined diagnostic modalities showed no statistically significant differences in diagnostic capability for both reader groups (see Table 5).

Table 4 True-positive, true-negative, false-positive and false-negative diagnoses [of 23 malignant (positive) and 55 non-malignant (negative) lesions] of the single MRI and CT part of radiologists A and B, of the combined PET/CT and PET/MRI evaluation of the two reader groups I and II as well as of the single PET part from PET/CT and PET/MRI of the nuclear medicine physicians 1 and 2, respectively.

	True-positive	True-negative	False-positive	False-negative
CT A	19	48	7	4
CT B	21	39	16	2
MRI A	17	53	2	6
MRI B	17	47	8	6
PET (CT) 1	22	40	15	1
PET (CT) 2	18	43	12	5
PET (MRI) 1	19	42	13	4
PET (MRI) 2	20	42	13	3
PET/CT I	18	49	6	5
PET/CT II	20	47	8	3
PET/MRI I	18	52	3	5
PET/MRI II	19	45	10	4

Sensitivity (%)

Specificity (%)

PPV (%)

NPV (%)
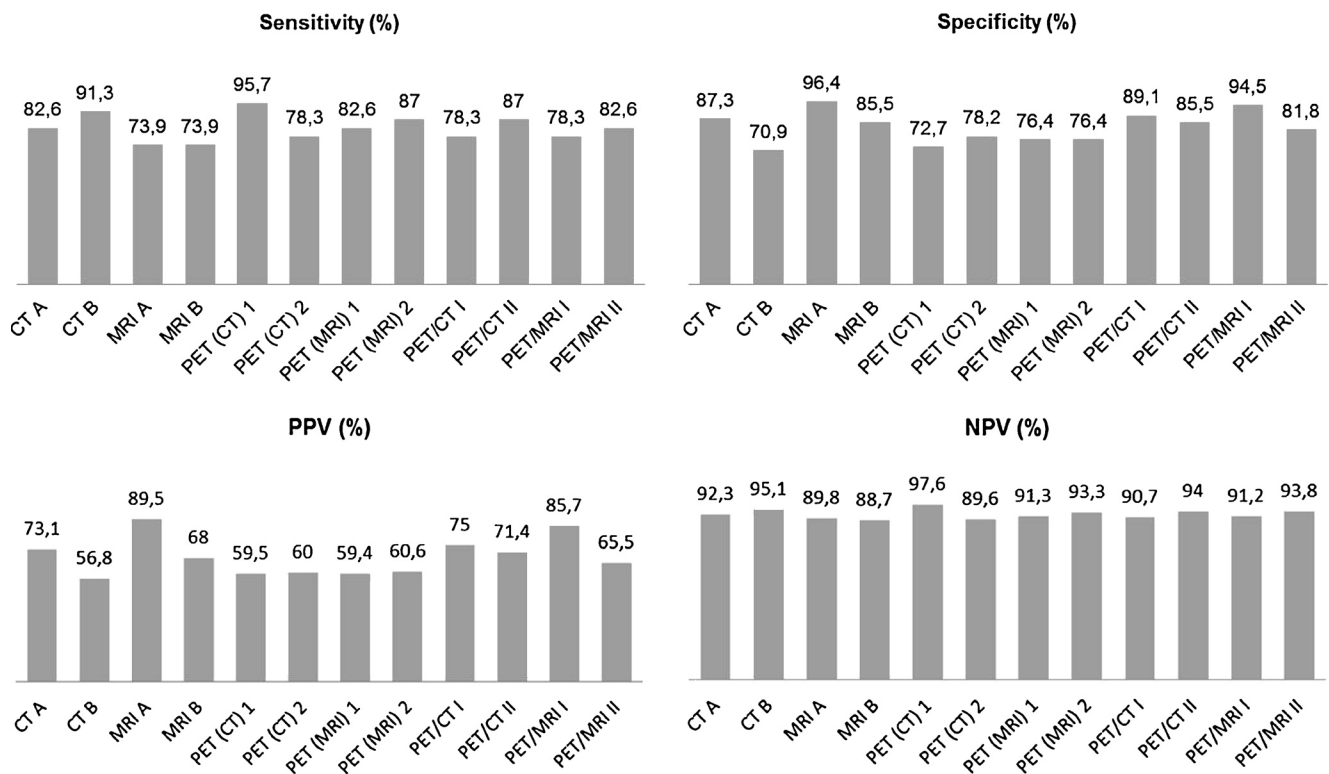
Fig. 2 Sensitivity, specificity, positive predictive value (PPV) and negative predictive value (NPV) of the single MRI and CT part of radiologists A and B, of the single PET part from PET (CT) and PET (MRI) of nuclear medicine physicians 1 and 2 as well as of the combined PET/CT and PET/MRI evaluation of the two reader groups I and II, respectively

The two radiological readers A and B detected slightly fewer malignant lesions on MRI as compared to the other single or combined modalities, which resulted in a sensitivity of 73.9 % and a NPV from 88.7 to 89.8 %. For instance, the laryngeal tumour of one patient was overlooked by both investigators, because only a very slight asymmetry in the vocal cord was present (see Fig. 3).

In contrast, both nuclear medicine physicians found more false-positive lesions (12–15) with both single PET parts from PET/CT and PET/MRI than all the other reader groups, resulting in a lower specificity from 72.7 to 78.2 %, associated with a PPV of 59.4–60.6 %. For example, the elevated ^{18}F-FDG uptake (SUV values between 5.3 and 10.8) in multiple mediastinal lymph nodes of a patient with histologically confirmed tuberculosis were falsely considered to be caused by tumoural growth by all single PET evaluations and the PET/CT as well as PET/MRI observer group I. In contrast, all single CT and MRI evaluations plus PET/CT and PET/MRI reader group II correctly categorized these lymph nodes as benign or inflammatory changes (see Fig. 4).

Similarly, there were also false-positive and false-negative diagnoses in difficult cases, which could be observed by almost every single investigator or reader group. For instance, in one patient a histopathologically confirmed nodular fibrosis with anthracosis in the left lung was falsely declared as intrapulmonary tumour or metastasis by all investigators and

modalities except the single MRI evaluation. In the combined evaluation these false-positive diagnoses were based on elevated radiotracer accumulation within the lesion (SUV=9).

The highest sensitivity of 95.7 % was reached by the single PET evaluation of nuclear physician 1. The best result for specificity was 96.4 % for the sole MRI evaluation of radiologist A.

The McNemar test revealed a statistically significant difference of the diagnostic capability between the single CT and MRI evaluation by radiologist B (p value=0.007). No statistically significant differences were shown between all the other single or combined modalities (Table 5).

Table 5 The p values and resulting statistical significance of the differences in diagnostic capability between all single or combined modalities [CT, MRI, PET (CT), PET (MRI), PET/CT and PET/MRI] by the same investigator or within the same observer group (A and B, 1 and 2, I and II).

Observer group	p value	Statistically significant
CT A and MRI A	0.065	No
CT B and MRI B	0.007	Yes
PET (CT) 1 and PET (MRI) 1	0.063	No
PET (CT) 2 and PET (MRI) 2	0.508	No
PET/CT I and PET/MRI I	0.549	No
PET/CT II and PET/MRI II	1.0	No

Fig. 3 A 52-year-old female patient with right glottic carcinoma and a nodal metastasis at level V on the right side (same patient as Fig. 1). TM seen on PET and CT, but missed on MRI by both examiners. **a** CT shows thickened vocal chord with slightly pronounced enhancement (*arrows*) and necrotic nodal metastasis (*open arrow*). **b** Fat-saturated T2-weighted TSE with only slight asymmetry of the vocal chord (*arrow*). **c** Inverted PET (CT) image with asymmetrically increased glucose metabolism at the level of the vocal chord (*arrow*). **d** Fusion of simultaneously acquired PET and T2-weighted TSE MR image
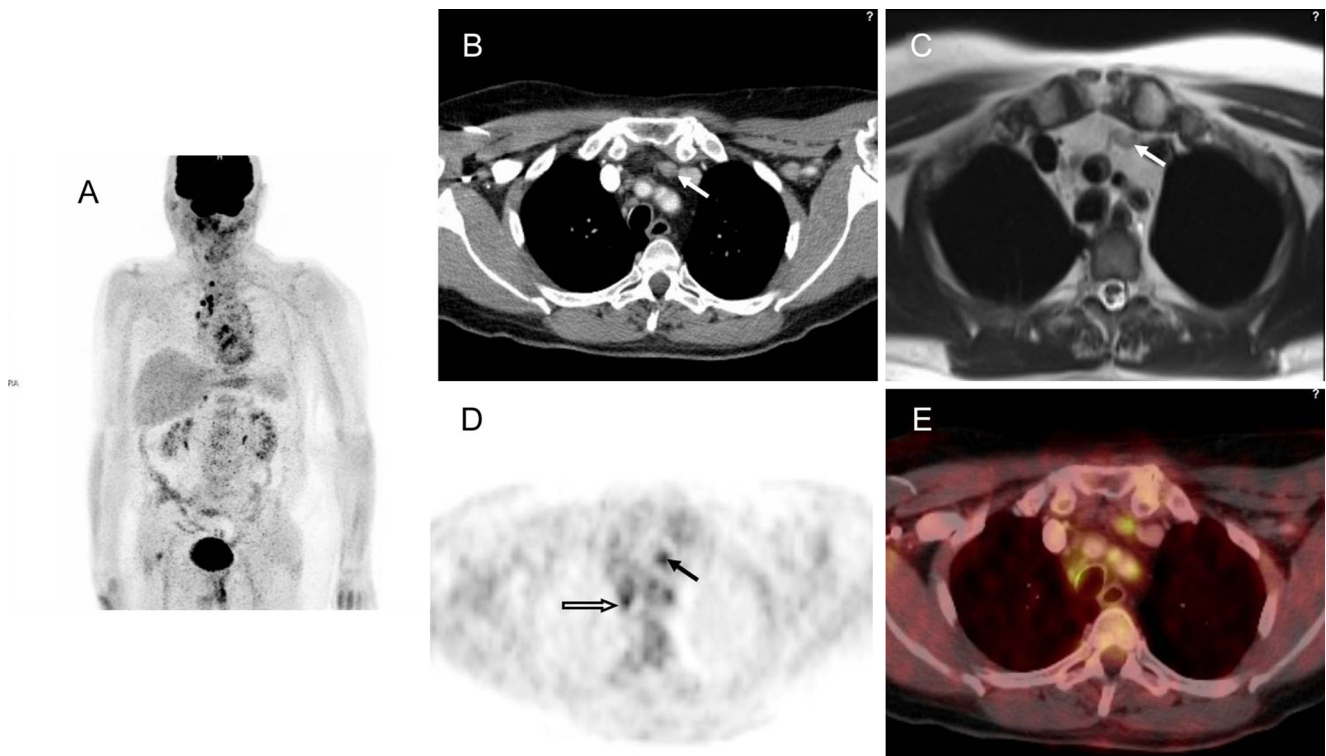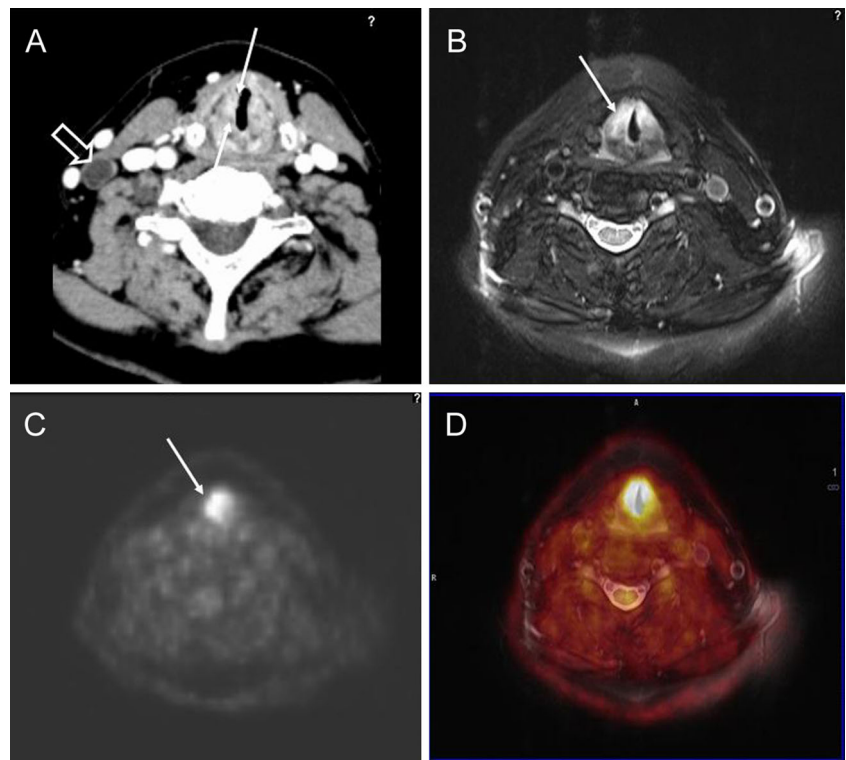
Fig. 4 A 70-year-old male patient with CUP (squamous cell carcinoma within the resected submandibular gland). PET/CT and consecutive PET/MRI for search of primary tumour and further metastases. Several lymph nodes were initially suspicious for metastasis due to increased glucose metabolism on ¹⁸F-FDG PET; however, pathohistology of the lymph node at level Vll (see **b** and **c**) showed tuberculosis. **a** MIP reconstruction of PET data with several suspicious lymph nodes in mediastinum and abdomen. **b** CT with only slightly enlarged lymph node in upper mediastinum/level VII (*arrow*). **c** MRI (whole-body T2-weighted HASTE) of the same lymph node (*arrow*). **d**) PET image with increased glucose metabolism in the same node (*arrow*) and in a lymph node further right (*open arrow*). **e**) Fused PET/CT image

Finally, in this study very good inter-rater agreement was found between both nuclear physicians concerning the single PET evaluation of PET/MRI with a Cohen's kappa coefficient of 0.82. For the remaining observer groups, good agreement with Cohen's kappa coefficients between 0.61 and 0.78 could be determined (Table 6).

Discussion

Prior studies in head and neck cancer patients so far concentrated on the feasibility of simultaneous [11] or sequential [12] PET/MRI acquisition and the resulting image quality. This study provides results of the first 17 patients with suspected cancer of the head and neck region undergoing simultaneous ^{18}F-FDG PET/MRI after routine PET/CT imaging at our institution. No statistically significant differences in sensitivity, specificity, PPV and NPV could be found between the two hybrid imaging modalities in these patients. This proves the diagnostic capabilities of the newly developed, integrated PET/MRI scanner, although the high expectations concerning superior performance of this method could not yet be verified [7, 8, 10]. This might be due to the high sensitivity of the PET examination, which helps to overcome limitations of tumour detection on CT and thus levels out the advantages of MRI in soft tissue tumour detection.

Evaluations concerning the image fusion from MRI and PET recently indicated that synchronous assessment of morphological (MRI) and functional (PET) data sets can be expected to reach a higher diagnostic accuracy in the evaluation of head and neck malignancies, compared to both imaging modalities applied solely. In the study conducted by Nakamoto et al. image fusion showed a slightly higher sensitivity (100 %) in diagnosing the primary tumour in comparison to MRI alone (98 %). Notably, in cases of recurrent tumour growth or occurrence of second malignancies, fused images were highly superior to MRI with an overall sensitivity of 92 instead of 67 %, respectively. In one patient with cancer of unknown origin the primary tumour and in other cases eight

Table 6 Inter-rater agreement between the different observer groups (radiologists A and B, nuclear medicine physicians 1 and 2, observer teams I and II) within the corresponding single or combined diagnostic modality [CT, MRI, PET (CT), PET (MRI), PET/CT and PET/MRI] derived from Cohen's kappa coefficient.

Observer group	Kappa coefficient	Inter-rater agreement
CT A and CT B	0.61	Good
MRI A and MRI B	0.78	Good
PET (CT) 1 and PET (CT) 2	0.77	Good
PET (MRI) 1 and PET (MRI) 2	0.82	Very good
PET/CT I and PET/CT II	0.65	Good
PET/MRI I and PET/MRI II	0.67	Good

further lesions were correctly identified by image fusion only [16]. This assumption is confirmed by the results of our study with an overall sensitivity of 74 % for the MRI part, not distinguishing between primary and recurrent tumours.

Another comparative study aimed to investigate suspected masticator space invasion of advanced buccal squamous cell carcinoma by using different imaging modalities, namely 3 T MRI, CT, PET/CT and retrospectively fused ^{18}F-FDG PET/MRI [17]. Seventeen patients were included in this prospective study. Eventually, fused PET/MRI was superior to the other imaging tools with its sensitivity and specificity of 90.0% and 90.9 %. Moreover, concerning the maximal tumour size, there was better agreement between fused PET/MR images and pathological findings compared to the other three modalities, which all showed overestimation in delineation of lesion diameter. The results of our study did not show such a high sensitivity for the simultaneous PET/MRI in detection of head and neck cancers; in fact they were comparable to PET/CT. However, PET/MRI is an upcoming diagnostic modality and so far there are no standards concerning imaging protocols or interpretation of the resulting images, whereas at our institution there already is a 6-year experience with PET/CT imaging, which might bias the results somewhat towards this modality. Furthermore, these patients represent the first sample of an ongoing, prospective study, so in a larger number of patients the PET/MRI might well prove to have superior diagnostic capability due to its better soft tissue contrast, especially in difficult cases of suspected tumour recurrence.

The MRI investigation on its own showed lower sensitivity in comparison to the other single or combined modalities. This finding emphasizes that the criteria of size, morphology and contrast enhancement are not always sufficient for correct classification of findings. In this study, several times the elevated radiotracer uptake was the only suggestive finding to indicate tumour growth or metastatic spread. This can be seen by the highest sensitivity achieved in the PET evaluation of the PET/CT by reader 1 (95.7 %). On the other hand, this evaluation resulted in the lowest specificity of all modalities in this study (72.7 %). Sensitivity and specificity of the PET evaluation of PET/MRI and PET/CT were comparable for both readers, although PET/MRI was constantly performed as the second examination. One can conclude that the order of the examinations does not influence detection of focal lesions on PET, although its influence on SUV is well known. SUV cut-off levels to distinguish benign from malignant lesions were not used since there is only a trend to higher SUV in malignant lesions. Furthermore, as Boellaard et al. described, SUV depends strongly on several parameters (e.g. effects of noise, image resolution and region of interest definition) and it can only be used for diagnostic purposes when data acquisition and processing are performed in a standardized way [18].

One reason for the lower specificity of PET can be the blinded diagnostic evaluation, as clinical information plays an

influential role in difficult cases. In the clinical setting of restaging and the corresponding question regarding presence or absence of vital tumour tissue, it is more than helpful to be aware of all information about the clinical history of a patient. This information eases differentiation between elevated tracer uptake as an effect of radiochemotherapy or as a sign of vital tumour tissue and will diminish false-positive and false-negative diagnoses. Additionally, nuclear medicine physicians at our institution routinely evaluate PET data in combination with CT instead of the PET component only. For this study, the restriction to PET images only could have had a negative effect on specificity. However, a study by Guenzel et al. compared MR with PET imaging in 120 patients suffering from malignant head and neck tumours and found no difference in sensitivity and specificity with regard to diagnosis of primary tumours, tumour recurrence or CUP [19]. Still they conclude that "a combination of both techniques is likely to be the future of diagnostic imaging".

Limitations of the study presented here comprise the small size of the study group, the inhomogeneity of the study group and the incomplete histopathological confirmation of suspected tumours. The strict order of PET/CT first followed by PET/MRI might also bias the results of glucose-avid findings.

Although the sample size is quite small, this is the first report about the performance of simultaneous PET/MRI in patients with head and neck cancer. As great expectations have been imposed on this method, especially in this patient group, the results help in forming a realistic view of the capabilities of PET/MRI. It will be interesting to investigate whether PET/MRI proves to be advantageous in more specific questions, e.g. detection of tumour recurrence, T staging of primary head and neck cancer or lymph node assessment.

Use of different CT protocols can be explained by different requirements of different chemotherapy studies, for which some of our patients were evaluated. Three patients received only dedicated PET/MRI sequences for the neck region and no whole-body protocol, as they did not agree to a procedure of more than 1 h duration. However, the differences in examined regions did not have any influence on the results of our study, because none of these patients showed a finding in the region not covered by one of the two modalities.

The strict order of the examinations can lead to bias; however, this study was planned keeping the standard PET/CT workflow for two reasons. First, it should give comparable results to earlier examinations. Second, it was not clear what the results of the PET/MRI would be like. As comparable sensitivity and specificity were found in this work, future studies can confidently use alternating strategies or place PET/MRI prior to PET/CT.

After all, these are the first results of patients with head and neck tumours examined in an integrated whole-body PET/MRI scanner and they prove both the technical possibility of a whole-body PET/MRI scan plus an additional, dedicated PET/MRI of the head and neck region as well as the diagnostic capability of the PET/MRI, which is comparable to PET/CT. Whether the new hybrid imaging technology is actually superior to PET/CT will have to be shown by comparisons of PET/CT versus PET/MRI in a larger cohort of patients and also in subgroup analyses (primary cancer staging—tumour recurrence—CUP).

References

1. Wippold FJ. Head and neck imaging: the role of CT and MRI. J Magn Reson Imaging 2007;25:453–65.
2. de Bondt RBJ, Nelemans PJ, Bakers F, Casselman JW, Peutz-Kootstra C, Kremer B, et al. Morphological MRI criteria improve the detection of lymph node metastases in head and neck squamous cell carcinoma: multivariate logistic regression analysis of MRI features of cervical lymph nodes. Eur Radiol 2009;19:626–33.
3. Castelijns JA, van den Brekel MWM. Imaging of lymphadenopathy in the neck. Eur Radiol 2002;12:727–38.
4. Nakamura T, Sumi M. Nodal imaging in the neck: recent advances in US, CT and MR imaging of metastatic nodes. Eur Radiol 2007;17: 1235–41.
5. Yoon DY, Hwang HS, Chang SK, Rho YS, Ahn HY, Kim JH, et al. CT, MR, US,18F-FDG PET/CT, and their combined use for the assessment of cervical lymph node metastases in squamous cell carcinoma of the head and neck. Eur Radiol 2009;19:634–42.
6. Ghanooni R, Delpierre I, Magremanne M, Vervaet C, Dumarey N, Remmelink M, et al. 18F-FDG PET/CT and MRI in the follow-up of head and neck squamous cell carcinoma. Contrast Media Mol Imaging 2011;6:260–6.
7. Beyer T, Freudenberg LS, Czernin J, Townsend DW. The future of hybrid imaging-part 3: PET/MR, small-animal imaging and beyond. Insights Imaging 2011;2:235–46.
8. Antoch G, Bockisch A. Combined PET/MRI: a new dimension in whole-body oncology imaging? Eur J Nucl Med Mol Imaging 2009;36 Suppl 1:S113–20.
9. Klinke T, Daboul A, Maron J, Gredes T, Puls R, Jaghsi A, et al. Artifacts in magnetic resonance imaging and computed tomography caused by dental materials. PLoS One 2012;7:e31766.
10. Castelijns JA. PET-MRI in the head and neck area: challenges and new directions. Eur Radiol 2011;21:2425–6.
11. Boss A, Stegger L, Bisdas S, Kolb A, Schwenzer N, Pfister M, et al. Feasibility of simultaneous PET/MR imaging in the head and upper neck area. Eur Radiol 2011;21:1439–46.
12. Platzek I, Beuthien-Baumann B, Schneider M, Gudziol V, Langner J, Schramm G, et al. PET/MRI in head and neck cancer: initial experience. Eur J Nucl Med Mol Imaging 2013;40:6–11.
13. Pearce T, Philip S, Brown J, Koh DM, Burn PR. Bone metastases from prostate, breast and multiple myeloma: differences in lesion conspicuity at short-tau inversion recovery and diffusion-weighted MRI. Br J Radiol 2012;85:1102–6.
14. Sommer G, Klarhöfer M, Lenz C, Scheffler K, Bongartz G, Winter L. Signal characteristics of focal bone marrow lesions in patients with

multiple myeloma using whole body T1w-TSE, T2w-STIR and diffusion-weighted imaging with background suppression. Eur Radiol 2011;21:857–62.

15. Heusner T, Kuemmel S, Koeninger A, Hamami ME, Hahn S, Quinsten A, et al. Diagnostic value of diffusion-weighted magnetic resonance imaging (DWI) compared to FDG PET/CT for whole-body breast cancer staging. Eur J Nucl Med Mol Imaging 2010;37:1077–86.

16. Nakamoto Y, Tamai K, Saga T, Higashi T, Hara T, Suga T, et al. Clinical value of image fusion from MR and PET in patients with head and neck cancer. Mol Imaging Biol 2009;11:46–53.

17. Huang S, Chien C, Lin W, Fang FM, Wang PW, Lui CC, et al. A comparative study of fused FDG PET/MRI, PET/CT, MRI, and CT imaging for assessing surrounding tissue invasion of advanced buccal squamous cell carcinoma. Clin Nucl Med 2011;36:518–25.

18. Boellaard R, Krak NC, Hoekstra OS, Lammertsma AA. Effects of noise, image resolution, and ROI definition on the accuracy of standard uptake values: a simulation study. J Nucl Med 2004;45:1519–27.

19. Guenzel T, Franzen A, Wiegand S, Kraetschmer S, Jahn JL, Mironczuk R, et al. The value of PET compared to MRI in malignant head and neck tumors. Anticancer Res 2013;33:1141–6.

2.3. In vivo Korrelation von Glukosemetabolismus, Zelldichte und mikrozirkulatorischen Parametern bei Patienten mit Kopf-Hals-Tumoren: erste Ergebnisse von Untersuchungen mittels simultaner PET/MRT

Im Laufe der ersten Jahre nach Einführung der PET/MRT-Diagnostik zeigte sich ein rascher Wandel im Forschungsinteresse der beteiligten Kollegen weltweit. Waren die ersten beiden Jahre noch stark von Machbarkeitsstudien und den direkten Vergleichen zwischen PET/CT und PET/MRT in der Tumordetektion geprägt [41, 131], wurde dann rasch der Fokus auf die zusätzlichen Möglichkeiten der neuen Scanner gelenkt.

Immer mehr wurde das Potential der neuen Methode nicht in der Tumordetektion, sondern in der Tumorcharakterisierung in den Mittelpunkt gestellt [70, 132–134]. Als Fernziel sieht die radiologisch-nuklearmedizinische Gemeinschaft die Möglichkeit, mit non-invasiven Mitteln Tumorherde detektieren und charakterisieren zu können. Damit soll es perspektivisch möglich sein, mittels Bildgebung die biologischen Eigenschaften eines Tumors und dessen Reaktion auf eine Therapie vorherzusagen.

Auch unsere Arbeitsgruppe befasste sich mit diesem Thema und untersuchte zunächst die Zusammenhänge verschiedener funktioneller Parameter, die mit dem neuen Gerät akquiriert werden können. Hierfür wurde ebenfalls ein Kollektiv aus HNO-Patienten zusammengestellt, bei denen der Primärtumor bzw. das lokale Rezidiv in der dedizierten Untersuchung der Kopf-Hals-Region nachgewiesen werden konnte. Zudem mussten die funktionellen Bildgebungen gut auswertbar sein.

Für diese Analyse konnten 17 Patienten identifiziert werden. Bei diesen wurden die Parameter zur Glukoseutilisation (standardized uptake value – SUV), zur Diffusion (apparent diffusion coefficient – ADC) und für verschiedene Perfusionswerte quantifiziert, welche im folgenden Artikel noch näher erläutert werden [135].

Letztlich konnte nachgewiesen werden, dass bei Kopf-Hals-Tumoren der Glukosestoffwechsel mit einzelnen Perfusionsparametern korreliert. Diese Arbeit wird als dritter Teil der Habilitationsschrift eingefügt.

Gawlitza, Matthias; Purz, Sandra; Kubiessa, Klaus; Boehm, Andreas; Barthel, Henryk; Kluge, Regine; Kahn, Thomas; Sabri, Osama; *Stumpp, Patrick* (2015):
In Vivo Correlation of Glucose Metabolism, Cell Density and Microcirculatory Parameters in Patients with Head and Neck Cancer: Initial Results Using Simultaneous PET/MRI.
PloS one 10 (8), S. e0134749.

In Vivo Correlation of Glucose Metabolism, Cell Density and Microcirculatory Parameters in Patients with Head and Neck Cancer: Initial Results Using Simultaneous PET/MRI

Matthias Gawlitza[1]☯*, Sandra Purz[2]☯, Klaus Kubiessa[1], Andreas Boehm[3], Henryk Barthel[2], Regine Kluge[2], Thomas Kahn[1], Osama Sabri[2], Patrick Stumpp[1]

1 Department of Diagnostic and Interventional Radiology, University Hospital of Leipzig, Liebigstraße 20, 04103 Leipzig, Germany, **2** Department of Nuclear Medicine, University Hospital of Leipzig, Liebigstraße 18, 04103 Leipzig, Germany, **3** ENT-Department, University Hospital of Leipzig, Liebigstraße 10–14, 04103 Leipzig, Germany

☯ These authors contributed equally to this work.
* matthias.gawlitza@medizin.uni-leipzig.de

Abstract

Objective

To demonstrate the feasibility of simultaneous acquisition of ^{18}F-FDG-PET, diffusion-weighted imaging (DWI) and T1-weighted dynamic contrast-enhanced MRI (T1w-DCE) in an integrated simultaneous PET/MRI in patients with head and neck squamous cell cancer (HNSCC) and to investigate possible correlations between these parameters.

Methods

17 patients that had given informed consent (15 male, 2 female) with biopsy-proven HNSCC underwent simultaneous ^{18}F-FDG-PET/MRI including DWI and T1w-DCE. SUV$_{max}$, SUV$_{mean}$, ADC$_{mean}$, ADC$_{min}$ and K^{trans}, k_{ep} and v_e were measured for each tumour and correlated using Spearman's ρ.

Results

Significant correlations were observed between SUV$_{mean}$ and K^{trans} (ρ = 0.43; p ≤ 0.05); SUV$_{mean}$ and k_{ep} (ρ = 0.44; p ≤ 0.05); K^{trans} and k_{ep} (ρ = 0.53; p ≤ 0.05); and between k_{ep} and v_e (ρ = -0.74; p ≤ 0.01). There was a trend towards statistical significance when correlating SUV$_{max}$ and ADC$_{min}$ (ρ = -0.35; p = 0.08); SUV$_{max}$ and K^{trans} (ρ = 0.37; p = 0.07); SUV$_{max}$ and k_{ep} (ρ = 0.39; p = 0.06); and ADC$_{mean}$ and v_e (ρ = 0.4; p = 0.06).

Conclusion

Simultaneous ^{18}F-FDG-PET/MRI including DWI and T1w-DCE in patients with HNSCC is feasible and allows depiction of complex interactions between glucose metabolism, microcirculatory parameters and cellular density.

Introduction

^{18}Fluor-fluorodesoxyglucose positron emission tomography combined with magnetic resonance imaging (^{18}F-FDG-PET/MRI) seems to be a promising modality for imaging of head and neck squamous cell carcinoma (HNSCC). In this type of malignancy an accurate diagnosis of infiltration of surrounding structures is important for local staging and for surgical and radiotherapy planning [1–4]. With the high soft-tissue contrast of MRI and the superior ability of ^{18}F-FDG-PET to detect vital tumor tissue prior to morphological changes, the advent of combined PET/MRI will open new perspectives in non-invasive imaging [3]. The combination of PET with MRI also opens up options to acquire multimodal molecular imaging parameters simultaneously. This may contribute to a more detailed characterization of molecular processes *in vivo* [5]. We report about the first study in which glucose metabolism (assessed by ^{18}F-FDG-PET), tumor cellularity (measured by diffusion-weighted imaging, DWI) and microcirculatory parameters (estimated by T1-weighted dynamic contrast-enhanced MRI, T1w-DCE) were simultaneously acquired in patients with HNSCC. Not only are these parameters known to be correlated with molecular markers for angiogenesis, proliferation or cell density [6–8]; first and foremost they are of special interest for prediction of patient outcome and response to chemotherapy or combined radiochemotherapy. For the future, the combination of these parameters may further facilitate treatment planning and prognostic stratification [9–12].

Materials and Methods

Patients

From October 2011 to September 2013, 82 consecutive patients with suspected malignancy of the head and neck or a cancer of unknown primary with cervical lymphadenopathy were scheduled to undergo ^{18}F-FDG-PET computed-tomography (^{18}F-FDG-PET/CT) for staging and treatment planning and, without additional radiopharmaceutical administration, an integrated simultaneous PET/MRI study. This study was IRB-approved and all patients gave their written informed consent. Patients were retrospectively included in the current study if they fulfilled the following inclusion criteria: (a) if a de-novo or recurring HNSCC of the upper aerodigestive tract was histopathologically proven either by biopsy or by resection after imaging, (b) if a histopathological report was available for a specimen taken from the area that was suspicious for tumor in imaging, (c) if a dedicated simultaneous PET/MRI of the neck including T1w-DCE and DWI sequences was performed with sufficient image quality not distorted by motion artefacts; (d) if a tumor was delineable in the imaging studies and (e) if there was no ongoing (radio)chemotherapy. Altogether, 17 patients fulfilled all inclusion criteria (see Fig 1).

Imaging preparation

All 17 patients underwent an ^{18}F-FDG-PET/CT protocol on a Siemens Biograph 16 PET/CT scanner and a simultaneous whole-body PET/MR after a fasting period of at least 6 hours. In 15 of 17 patients PET/CT was performed first and then PET/MRI, in two patients PET/MRI was performed prior to PET/CT due to logistic reasons. Administration of ^{18}F-FDG was performed once for both studies, depending on body weight (5 MBq/kg, range 205–396 MBq). Postinjection median uptake time was 83 minutes (range 60–120 minutes) for the first imaging study and 196 minutes (range 150–260 minutes) for the second imaging study.

PET/MRI scanner

All examinations were performed on a simultaneous PET/MRI scanner (Siemens Biograph mMR; Siemens Healthcare, Erlangen, Germany). The system is composed of a PET detector
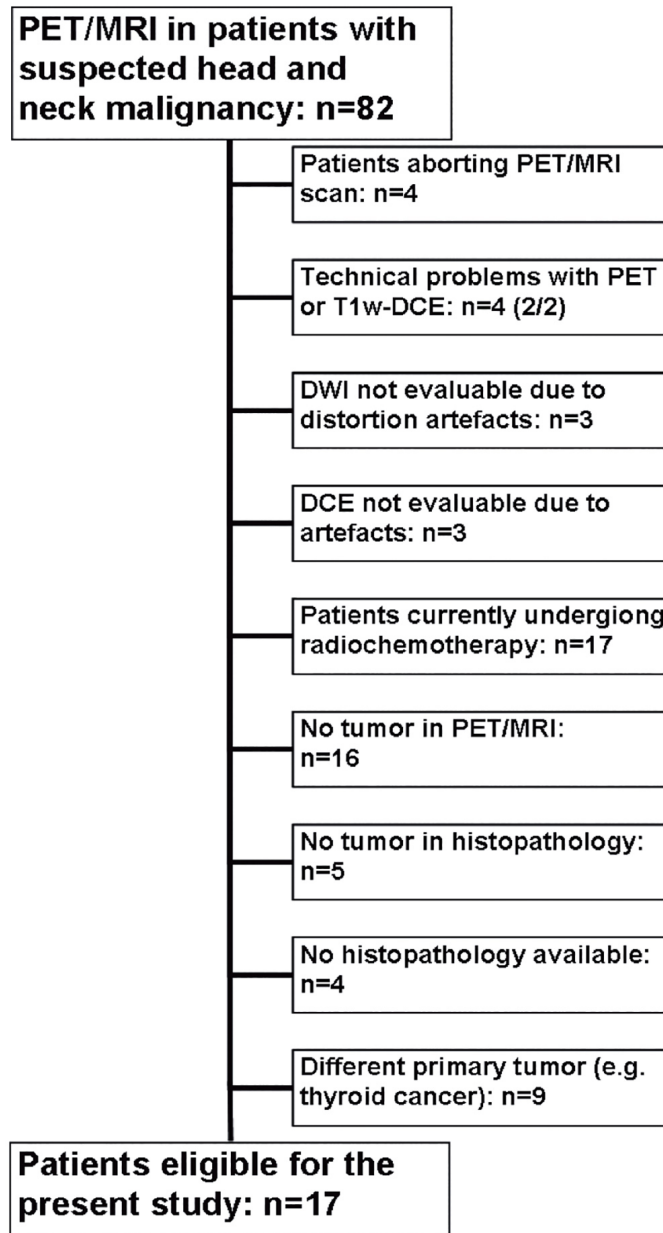
Fig 1. Flowchart of the study population.

doi:10.1371/journal.pone.0134749.g001

ring mounted into a 3.0T whole-body magnetic resonance tomograph, resulting in a hybrid imager with a bore diameter of 60 cm and a magnet length of 163 cm. Maximum gradient strength accounts for 45 mT/m, slew rate for 200 T/m/s in all three spatial directions. The MRI-compatible PET detector ring is implemented inside the bore and consists of 56 LSO-APD (lutetium oxyorthosilicate scintillation crystals combined with avalanche photodiodes) block detectors with 64 detector ring elements arranged on the z-axis. This yields an axial field of view (FOV) of about 60 cm and a FOV of about 26 cm in z-direction. Maximum scan length is about 160 cm without repositioning. More detailed descriptions of the technical aspects were described in previous publications [13,14].

Simultaneous PET/MRI imaging protocol

Patients were placed in supine position with their arms beside the trunk. PET/MRI was conducted in two steps. First, whole-body imaging without contrast medium was performed in six bed positions (head, neck, thorax, abdomen, pelvis and proximal thighs) with a coronal 3D-encoded gradient-echo sequence for attenuation correction (Dixon-VIBE) followed by coronal T2-weighted turbo inversion recovery magnitude (TIRM) and axial T2-weighted half Fourier single shot turbo spin echo (HASTE) sequences as well as axial echoplanar imaging diffusion weighted images (EPI-DWI) with b-values of 0 and 800. Simultaneous to MRI, PET image acquisition was conducted with 5 minutes of scan time per bed position.

Afterwards, a dedicated PET/MRI of the neck using a combined head and neck coil was performed, which also included a coronal Dixon-VIBE sequence for attenuation correction. This was followed by axial T1-weighted turbo spin echo (TSE) and T2-weighted TSE sequences with fat suppression, a coronal T2-weighted TIRM and an axial DWI-EPI sequence with b-values of 0 and 800 (TR/TE 8620/73 ms, slice thickness 4 mm, voxel size 3.2 x 2.6 x 4.0 mm³). Dynamic contrast-enhanced imaging was performed during the administration of 0.1 mmol Gadobutrol per kg of bodyweight (Gadovist, Bayer Healthcare, Leverkusen, Germany) at a rate of 3 ml per second and flushing with 10 ml of normal saline using a power injector (Spectris Solaris, Medrad/Bayer Healthcare, Leverkusen, Germany). T1w-DCE consisted of 40 subsequent scans with a duration of 6 seconds (40 slices per scan), a TR/TE of 2.47/0.97 ms, a slice thickness of 5 mm, a flip angle of 8° and a voxel size of 1.2 x 1.0 x 5.0 mm³; the contrast application was started after the fifth scan. Furthermore axial and coronal fat saturated T1-weighted TSE sequences and an axial contrast enhanced T1-weighted VIBE sequence were conducted after contrast application. Altogether, the dedicated neck protocol accounts for about 30 min of scan time, during which dedicated PET of the neck was conducted for 10 minutes. PET images were reconstructed using the iterative ordered subset expectation maximization algorithm with 3 iterations and 21 subsets, a Gaussian filter with 3 mm full width at half maximum (FWHM), and a 256 x 256 image matrix. Attenuation correction of the PET data was performed using a four-tissue (fat, soft tissue, air, background) model attenuation map which was generated from a Dixon-Vibe MR sequence. A dedicated description of a typical imaging protocol including the complete set of sequence parameters was published recently [1].

Image analysis

PET data sets were reviewed on a commercially available workstation (using Syngo.Via, Siemens Healthcare, Erlangen, Germany) by one resident in diagnostic radiology with 4 years and one board certified nuclear medicine physician with 7 years of experience in head and neck CT, MR and PET/CT imaging. For all tumors, mean and maximum standardized uptake values (SUV) were analyzed in the PET dataset of the neck with the nuclear medicine physician plotting an isocontour volume of interest (VOI) around the tumor (SUV_{max} threshold 40%).

T1w-DCE images were processed with a commercially available software module for tissue perfusion estimation (Tissue 4D, Siemens Medical Systems, Erlangen, Germany) as described previously [15]. The software offers a population based approach for the arterial input function (AIF) and the best of three available AIF-options was chosen according to the result of the chi2-parameter, which serves as an error measure for the model fit. After scaling the AIF in relation to the gadolinium dose and modelling it by the most widely used bi-exponential model by Tofts and Kermode [16], the pharmacokinetic parameters K^{trans}, k_{ep} and v_e were calculated. In this two-compartment model, the volume transfer constant K^{trans} estimates the diffusion of contrast medium from the plasma through the vessel wall into the interstitial space, thus representing vessel permeability. v_e expresses the volume of the extravascular extracellular leakage
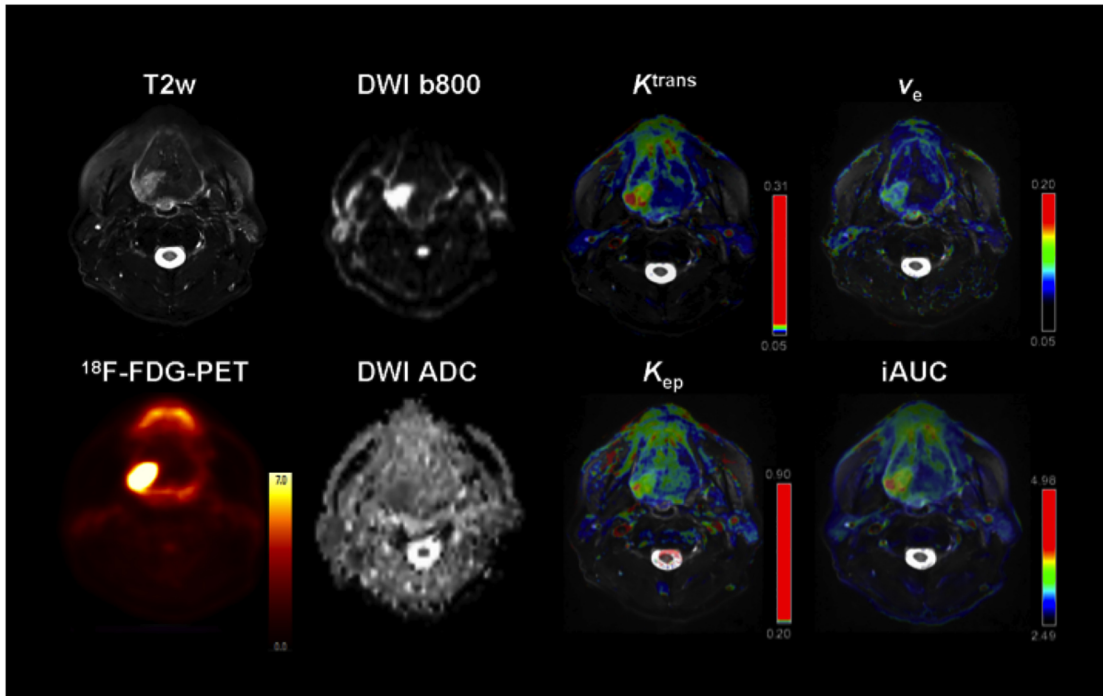
Fig 2. Example of a 59-year old male patient depicting the different molecular parameters obtained by simultaneous PET/MRI. Note the biopsy-proven secondary squamous cell carcinoma of the base of the tongue on the right side. 23 months ago the patient was operated on a squamous cell carcinoma of the soft palate on the same side.

doi:10.1371/journal.pone.0134749.g002

space (EES). k_{ep} is a parameter for diffusion of contrast medium from the EES back to the plasma. It is in close relation with K^{trans} and v_e and is calculated by the formula $k_{ep} = K^{trans} \times v_e^{-1}$. The basic concept of these parameters and their application in patients with HNSCC is described in greater detail in other publications [15,17]. For each patient, these four parameter maps were projected onto the T2-weighted fat-suppressed TSE sequences and the radiologist delineated the tumor manually on each slice, resulting in mean values of K^{trans}, k_{ep} and v_e averaged over the complete tumor. Attention was paid not to include areas of gross necrosis or large feeding vessels in close proximity into the ROI.

DWI images were transferred to a desktop computer with Mac OS X (Apple, Cupertino, California, USA) and an open-source freeware 4D DICOM viewer (OsiriX, Pixmeo, Geneva Switzerland) [18]. ROI's were manually drawn on the apparent diffusion coefficient (ADC) maps along the contours of the tumor on each slice in cognitive fusion with the complete MRI and PET datasets; mean and minimal ADC values (ADC_{mean} and ADC_{min}) were then averaged for the whole tumor volume. Again, necrotic tumor areas were not to be included into the ROI. An example of the combined molecular parameter maps is depicted in Fig 2.

Statistical analysis

Statistical analysis and graphics creation was performed with SPSS 20 (IBM SPSS Statistics, Armonk, New York, USA). Values are presented as mean ± standard deviation (SD). Mean value comparison was carried out using the Mann-Whitney-U test. Spearman's non-parametric rank sum correlation coefficients were calculated between DCE parameters, SUV_{max}, SUV_{mean}, ADC_{mean} and ADC_{min}. Significance level was set at $p \leq 0.05$.

53

Table 1. Patient and Tumor characteristics.

Patient characteristics				Tumor characteristics						
Patient number	Sex	Age (yrs.)	Primary or recurrent cancer	Tumor site	Tumor volume in PET (cm³)	Tumor size in MRI (cmxcm)	Tumor staging (original staging for recurrent cancers)			Tumor grading
1	M	54	primary	Oropharynx	18,0	3,8 x 3,2	cT3	cN2b	cM0	G2
2	M	57	primary	Oropharynx	3,3	2,4 x 1,6	cT2	cN3	cM0	G2
3	M	50	primary	Hypopharynx	12,6	3,4 x 3,3	cT4b	cN3	cM0	G2
4	M	56	primary	Hypopharynx	4,2	1,9 x 1,6	cT3	cN1	cM0	G3
5	M	61	primary	Larynx	8,0	3,5 x 2,6	pT3	pN2c	cM0	G3
6	F	66	primary	Oropharynx	9,5	3,0 x 2,4	cT2	cN2b	cM0	G3
7	M	49	primary	Hypopharynx	22,1	4,2 x 2,5	cT4	cN2c	cM0	G2
8	M	50	primary	Oro-/ Hypopharynx	42,7	3,8 x 3,2	cT4b	cN2b	cM1	G2
9	F	57	primary	Tongue	5,9	3,6 x 1,7	cT4a	cN2c	cM0	G1
10	M	54	primary	Oropharynx	6,9	3,8 x 2,7	cT3	cN2c	cM0	G3
11	M	63	primary	Oro-/ Hypopharynx	17,3	5,0 x 2,3	pT3	pN3	cM0	G3
12	M	59	recurrent	Tongue	4,1	2,3 x 1,4	cT3	cN1	cM0	G2
13	M	59	recurrent	Tongue	13,1	3,4 x 1,4	cT4a	cN2c	cM0	G2
14	M	79	recurrent	Oral diaphragm	44,1	4,7 x 3,2	pT1	pN0	M0	G3
15	M	53	recurrent	Oropharynx	5,1	2,5 x 0,9	pT3	pN0	M0	G3
16	M	52	recurrent	Larynx	2,9	1,7 x 1,0	pT4a	pN2c	M0	G3
17	M	61	recurrent	Tongue / Oral diaphragm	10,6	2,3 x 1,8	pT3	pN0	M0	G2

doi:10.1371/journal.pone.0134749.t001

Results

Of the 17 patients, 15 were male and 2 female. Mean age was 57.7 ± 7.3 years (range 49–79 years). Tumors were 11 primary cancers and 6 recurrent cancers, located in the oral cavity (n = 4), in the oropharynx (n = 8) or in the hypopharynx and larynx (n = 5). In patients with recurrent HNSCC, mean time from the end of therapy to diagnosis of the recurring carcinoma was 46 months (range from 12 to 120 months). Patient and tumor characteristics are shown in Table 1, functional imaging parameters of our patient group are depicted in Table 2.

Significant correlations were observed between SUV_{mean} and K^{trans}, and between SUV_{mean} and k_{ep}. Significant correlations were also present between the microcirculatory parameters K^{trans} and k_{ep}, and between k_{ep} and v_e. Furthermore we noted a trend towards an inverse correlation between SUV_{max} and ADC_{min} and a trend and towards a positive correlation between

Table 2. Functional imaging parameters.

Parameter	All patients (n = 17)
SUV_{max}	20.4 ± 7.78
SUV_{mean}	12.3 ± 5.07
ADC_{mean} (mm²/s)	1287 ± 150
ADC_{min} (mm²/s)	659 ± 175
K^{trans} (min⁻¹)	0.19 ± 0.06
k_{ep} (min⁻¹)	0.41 ± 0.18
v_e	0.53 ± 0.13

doi:10.1371/journal.pone.0134749.t002
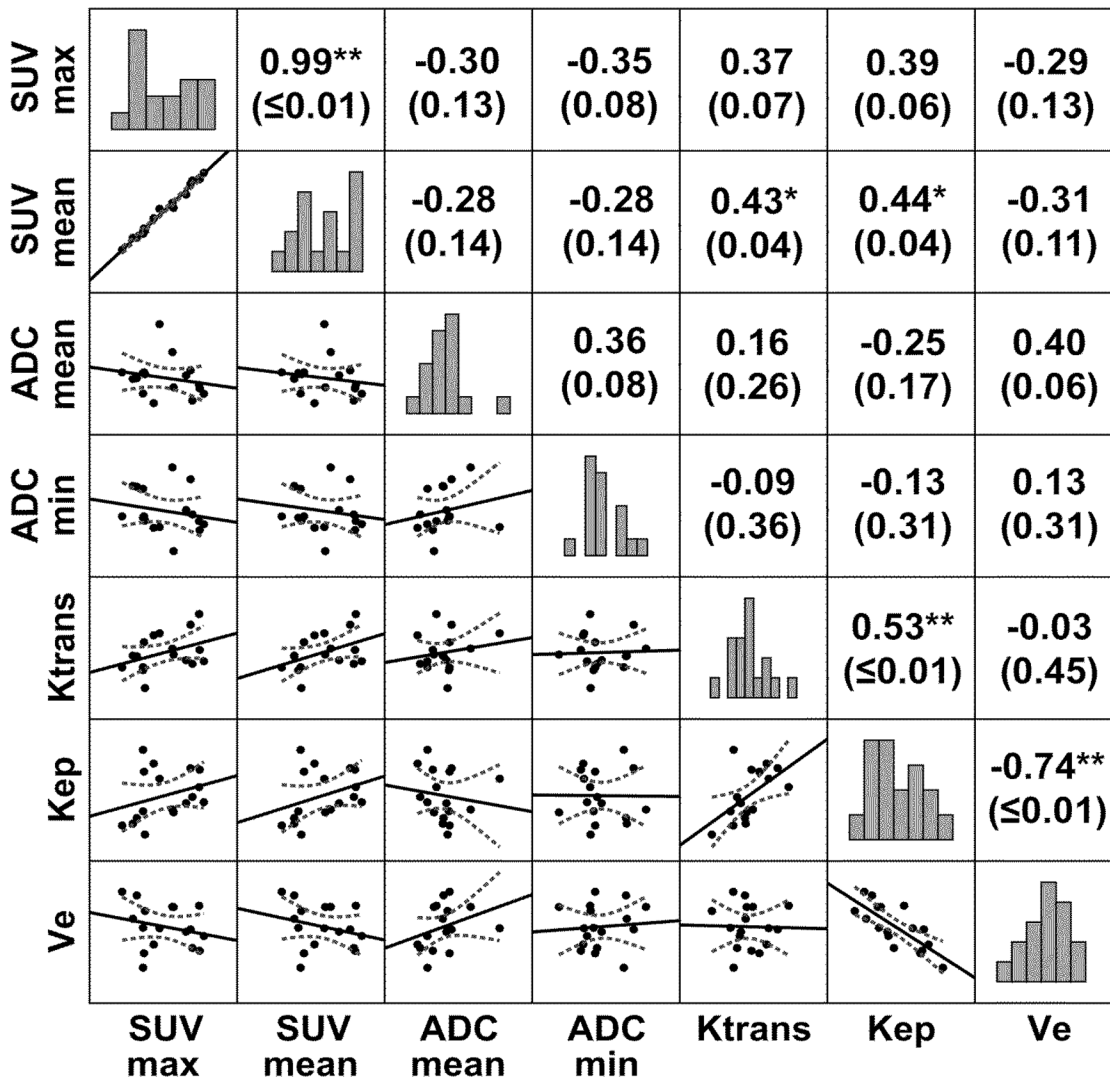
Fig 3. Correlation map of the different molecular imaging parameters in HNSCC. Correlations between ^{18}F-FDG-PET, T1w-DCE and DWI were computed using Spearman's non-parametric rank sum correlation coefficient. Numbers in parentheses represent p-values. * $p \leq 0.05$; ** $p \leq 0.01$. Bar graphs indicate the distribution of values.

doi:10.1371/journal.pone.0134749.g003

SUV_{max} and the DCE parameters K^{trans} and k_{ep}. Also between ADC_{mean} and v_e a trend towards a positive correlation was apparent. Results are depicted in Fig 3.

Discussion

Recently, a study on patients with suspected cancer of the head and neck region undergoing simultaneous ^{18}F-FDG-PET/MRI after routine ^{18}F-FDG-PET/CT was published in which no statistically significant differences regarding sensitivity, specificity, PPV and NPV was found between the two hybrid imaging modalities [1]. The current study demonstrates that the *in vivo* assessment of glucose metabolism, tissue cell density and microcirculatory parameters of HNSCC is feasible with simultaneous PET/MRI. At this point it has to be acknowledged that these analyses can also be performed on sequentially obtained data. However, this work

demonstrates that PET/MRI can display complex interactions between glucose metabolism and microcirculation (expressed by correlations between SUV and K^{trans} / k_{ep}), between glucose uptake and cellular density (depicted by correlations between SUV and ADC) and between cellularity and volume of the extravascular space (estimated by the correlation between ADC and v_e. As all correlations between the different molecular modalities were at best moderate, their combined acquisition seems to provide complementary and not redundant information; yet, they seem to be connected to a certain degree.

We observed a significant correlation and a trend towards a correlation, respectively, between SUV_{mean}/SUV_{max} and K^{trans}. This can be interpreted as an indicator of an elevated neoangiogenesis in tumors with a higher proliferation rate and a higher glucose demand. In these tumors the expression of vascular growth factors might lead to the formation of a primitive vascular plexus. This primitive vascular plexus typically shows an increased leakiness which is represented by the transfer constant K^{trans} in the Tofts model [15]. Our results support the theory of other studies in which relations between the vessel permeability measured by T1w-DCE MRI and the expression of vascular endothelial growth factor were observed in colorectal and breast cancer [19,20]. Furthermore, the correlation between glucose metabolism measured by ^{18}F-FDG-PET and vascular endothelial growth factor (VEGF) expression has already been proven for example in oesophageal squamous cell cancer [21]. After leakage into the tumor's extravascular space, the blood and contrast medium have to be transported back into the plasma, which is expressed by the rate constant k_{ep}. As the latter is closely related to K^{trans}, also its correlation with glucose uptake seems logical. This also supports a previous study in which a correlation between k_{ep} and the FDG dose uptake ratio was reported in patients with breast cancer [22]. For HNSCC Bisdas et al. used CT-perfusion and showed a positive correlation between glucose metabolism and vessel permeability (PS), which is essentially akin to k_{ep} [23]. Nevertheless there are ambiguous results described in the literature concerning the relation between glucose metabolism and vessel permeability estimated by k_{ep} or K^{trans}. In several other studies on HNSCC no correlations between SUV_{max} and k_{ep} and / or K^{trans} were detected [8,15]. In a study on hepatocellular carcinomas the authors even reported on an inverse correlation between SUV values and K^{trans} [24].

In our study a positive correlation was observed between K^{trans} and k_{ep}. This positive correlation was also highlighted in a previous examination of patients with HNSCC using T1w-DCE [15]. That study concluded that the enlarged fenestrae of the immature neovessels, which promote contrast medium extravasation (measured by K^{trans}) in turn also allow for a fast influx back into the capillary plasma, which is estimated by k_{ep}[15]. Moreover, these two parameters are linked by the aforementioned formula $k_{ep} = K^{trans}$ x v_e^{-1}. Another parameter that can be obtained from T1w-DCE analysis is iAUC, the area under the curve. Yet, the interpretation of the correlations for this parameter is difficult and should be treated with caution as iAUC itself is a model-free parameter and is as such prone to variations caused by the length of an acquired T1w-DCE dataset or by different physiological conditions. It was therefore stated by Cheng [25] that conventional iAUC could not be used as a surrogate pharmacokinetic parameter and that pharmacokinetic modelling (e.g. Tofts' and Kermode's model [16]) might be the "ideal approach" for accurate quantification—if several conditions, like a valid AIF, are met. This is also why we decided to exclude iAUC from our analysis.

The strong negative correlation between k_{ep} and v_e supports the results of previous works by Bisdas et al. [15] and Jansen et al. [8] in which similarly strong inverse correlations between these two parameters were observed. The authors ascribed this finding to the smaller interstitial space (expressed by v_e) being responsible for a higher back-flux rate into the plasma (represented by k_{ep}) because diffusion of a molecule usually happens from a region of higher concentration to one with a lower concentration.

The trend towards a positive correlation between ADC_{mean} and v_e that we observed also seems logical. In a tumor with less dense cell complexes the ADC values increase as a measure of less restricted water diffusion; smaller cell density should in turn also result in a larger extravascular space, measured by v_e. Yet, this could not be proven in patients with neoplasms of the brain [26–28] or the breast [29]. Our results therefore give a hint that this assumption might actually be true, at least with regards to HNSCC.

Concerning the associations between SUV_{max} and ADC_{min} we observed a trend towards a weak to moderate inverse correlation in our study. As opposed to the relation between T1w-DCE and DWI and that between T1w-DCE and PET, which have been subject to little research to date, publications about the correlation between ^{18}F-FDG-PET and DWI parameters are numerous and their results partly ambiguous. Since glucose metabolism is known to be positively correlated with the amount of viable tumor cells and growth rate, an inverse correlation between FDG uptake and ADC values, which reflect tumor cellularity, should be expected [7,30]. Nevertheless, whereas this presumption was confirmed for example in rectal [31], cervical [32], lung [33,34] and breast cancer [35], a similar relation could be demonstrated for HNSCC in only one publication [12] whereas in several other studies no such correlation was apparent [36–38]. The trend towards a moderate inverse correlation between SUV_{max} and ADC_{min} in our patient group might indicate that these parameters are not completely independent and support the hypothesis of Nakajo *et al.* who concluded that the glycolytic activity of HNSCC seems to be partly related with their microstructural environment [12].

In the future, simultaneous functional imaging with PET/MRI could be of special interest for treatment planning and prognostic stratification of oncologic patients. DWI and T1-DCE as well as ^{18}F-FDG-PET were proven to be suitable for this purpose in patients with HNSCC prior to radiochemotherapy [9–12]; a satisfactory therapy response and a better prognosis is thought to be related to higher K^{trans} [9], higher ADC_{mean} and lower SUV_{max} values [12]. During successful radiochemotherapy ADC values are increasing [39], whereas ^{18}F-FDG uptake and K^{trans} are known to decrease as a sign to therapy response [40,41]. With PET/MRI and a combined acquisition of these parameters further studies to investigate the most suitable modality for assessment and prediction of therapy response are possible.

Our study has several limitations with its small patient number and its retrospective design being the most important ones. The high exclusion rate attributable to technical reasons shows that such sophisticated examinations are probably not yet ready for clinical routine imaging. As it was a pilot study, our results have to be proven for larger patient series. Higher patient numbers could also compensate for the partial lack of statistical significance. As we only studied the tumors themselves and not lymph nodes, on-going studies are focusing on the question to which extent the results are adaptable to nodal metastases in HNSCC.

Conclusion

Simultaneous ^{18}F-FDG-PET/MRI including DWI and T1w-DCE in patients with HNSCC is feasible and allows depiction of complex interactions between glucose metabolism, microcirculatory parameters and cellular density; in the future this might contribute to the planning and adaptation of treatment plans with the aim of optimizing patient outcomes.

Author Contributions

Conceived and designed the experiments: MG SP PS. Performed the experiments: MG SP PS. Analyzed the data: MG. Contributed reagents/materials/analysis tools: TK OS. Wrote the paper: MG PS SP. Critical revision of the manuscript: MG SP KK AB HB RK TK OS PS.

References

1. Kubiessa K, Purz S, Gawlitza M, Kühn A, Fuchs J, Steinhoff KG, et al. Initial clinical results of simultaneous (18)F-FDG PET/MRI in comparison to (18)F-FDG PET/CT in patients with head and neck cancer. Eur J Nucl Med Mol Imaging. 2013; doi: 10.1007/s00259-013-2633-2

2. Platzek I, Beuthien-Baumann B, Schneider M, Gudziol V, Langner J, Schramm G, et al. PET/MRI in head and neck cancer: initial experience. Eur J Nucl Med Mol Imaging. 2013; 40: 6–11. doi: 10.1007/s00259-012-2248-z PMID: 23053322

3. Von Schulthess GK, Kuhn FP, Kaufmann P, Veit-Haibach P. Clinical Positron Emission Tomography/ Magnetic Resonance Imaging Applications. Semin Nucl Med. 2013; 43: 3–10. PMID: 23178084

4. Loeffelbein DJ, Souvatzoglou M, Wankerl V, Martinez-Möller A, Dinges J, Schwaiger M, et al. PET-MRI Fusion in Head-and-Neck Oncology: Current Status and Implications for Hybrid PET/MRI. J Oral Maxillofac Surg. 2012; 70: 473–483. doi: 10.1016/j.joms.2011.02.120 PMID: 21601338

5. Sauter AW, Wehrl HF, Kolb A, Judenhofer MS, Pichler BJ. Combined PET/MRI: one step further in multimodality imaging. Trends Mol Med. 2010; 16: 508–515. doi: 10.1016/j.molmed.2010.08.003 PMID: 20851684

6. Ginat DT, Mangla R, Yeaney G, Johnson M, Ekholm S. Diffusion-weighted imaging for differentiating benign from malignant skull lesions and correlation with cell density. AJR Am J Roentgenol. 2012; 198: W597–601. doi: 10.2214/AJR.11.7424 PMID: 22623576

7. Minn H, Clavo AC, Grénman R, Wahl RL. In Vitro Comparison of Cell Proliferation Kinetics and Uptake of Tritiated Fluorodeoxyglucose and L-Methionine in Squamous-Cell Carcinoma of the Head and Neck. J Nucl Med. 1995; 36: 252–258. PMID: 7830126

8. Jansen JFA, Schoder H, Lee NY, Stambuk HE, Wang Y, Fury MG, et al. Tumor Metabolism and Perfusion in Head and Neck Squamous Cell Carcinoma: Pretreatment Multimodality Imaging with 1H-Magnetic Resonance Spectroscopy, Dynamic Contrast-Enhanced MRI and 18F-FDG PET. Int J Radiat Oncol Biol Phys. 2012; 82: 299–307. doi: 10.1016/j.ijrobp.2010.11.022 PMID: 21236594

9. Kim S, Loevner LA, Quon H, Kilger A, Sherman E, Weinstein G, et al. Prediction of Response to Chemoradiation Therapy in Squamous Cell Carcinomas of the Head and Neck Using Dynamic Contrast-Enhanced MR Imaging. Am J Neuroradiol AJNR. 2010; 31: 262–268. doi: 10.3174/ajnr.A1817 PMID: 19797785

10. Ng S-H, Lin C-Y, Chan S-C, Yen T-C, Liao C-T, Chang JT-C, et al. Dynamic contrast-enhanced MR imaging predicts local control in oropharyngeal or hypopharyngeal squamous cell carcinoma treated with chemoradiotherapy. PloS One. 2013; 8: e72230. doi: 10.1371/journal.pone.0072230 PMID: 23951300

11. Berrak S, Chawla S, Kim S, Quon H, Sherman E, Loevner LA, et al. Diffusion weighted imaging in predicting progression free survival in patients with squamous cell carcinomas of the head and neck treated with induction chemotherapy. Acad Radiol. 2011; 18: 1225–1232. doi: 10.1016/j.acra.2011.06.009 PMID: 21835649

12. Nakajo M, Nakajo M, Kajiya Y, Tani A, Kamiyama T, Yonekura R, et al. FDG PET/CT and Diffusion-Weighted Imaging of Head and Neck Squamous Cell Carcinoma. Clin Nucl Med. 2012; 37: 475–480. doi: 10.1097/RLU.0b013e318248524a PMID: 22475897

13. Sattler B, Jochimsen T, Barthel H, Sommerfeld K, Stumpp P, Hoffmann K-T, et al. Physical and organizational provision for installation, regulatory requirements and implementation of a simultaneous hybrid PET/MR-imaging system in an integrated research and clinical setting. Magma. 2013; 26: 159–171. doi: 10.1007/s10334-012-0347-2 PMID: 23053713

14. Schwenzer NF, Schraml C, Müller M, Brendle C, Sauter A, Spengler W, et al. Pulmonary lesion assessment: comparison of whole-body hybrid MR/PET and PET/CT imaging—pilot study. Radiology. 2012; 264: 551–558. doi: 10.1148/radiol.12111942 PMID: 22653189

15. Bisdas S, Seitz O, Middendorp M, Chambron-Pinho N, Bisdas T, Vogl TJ, et al. An exploratory pilot study into the association between microcirculatory parameters derived by MRI-based pharmacokinetic analysis and glucose utilization estimated by PET-CT imaging in head and neck cancer. Eur Radiol. 2010; 20: 2358–2366. doi: 10.1007/s00330-010-1803-x PMID: 20443116

16. Tofts PS, Kermode AG. Measurement of the blood-brain barrier permeability and leakage space using dynamic MR imaging. 1. Fundamental concepts. Magn Reson Med. 1991; 17: 357–367. PMID: 2062210

17. Choyke PL, Dwyer AJ, Knopp MV. Functional tumor imaging with dynamic contrast-enhanced magnetic resonance imaging. J Magn Reson Imaging. 2003; 17: 509–520. doi: 10.1002/jmri.10304 PMID: 12720260

18. Rosset A, Spadola L, Ratib O. OsiriX: an open-source software for navigating in multidimensional DICOM images. J Digit Imaging. 2004; 17: 205–216. doi: 10.1007/s10278-004-1014-6 PMID: 15534753

19. Knopp M v., Weiss E, Sinn H p., Mattern J, Junkermann H, Radeleff J, et al. Pathophysiologic basis of contrast enhancement in breast tumors. J Magn Reson Imaging. 1999; 10: 260–266. doi: 10.1002/(SICI)1522-2586(199909)10:3<260::AID-JMRI6>3.0.CO;2-7 PMID: 10508285

20. George ML, Dzik-Jurasz ASK, Padhani AR, Brown G, Tait DM, Eccles SA, et al. Non-invasive methods of assessing angiogenesis and their value in predicting response to treatment in colorectal cancer. Br J Surg. 2001; 88: 1628–1636. doi: 10.1046/j.0007-1323.2001.01947.x PMID: 11736977

21. Kobayashi M, Kaida H, Kawahara A, Hattori S, Kurata S, Hayakawa M, et al. The relationship between GLUT-1 and vascular endothelial growth factor expression and 18F-FDG uptake in esophageal squamous cell cancer patients. Clin Nucl Med. 2012; 37: 447–452. doi: 10.1097/RLU.0b013e31823924bb PMID: 22475893

22. Semple SIK, Gilbert FJ, Redpath TW, Staff RT, Ahearn TS, Welch AE, et al. The relationship between vascular and metabolic characteristics of primary breast tumours. Eur Radiol. 2004; 14: 2038–2045. doi: 10.1007/s00330-004-2454-6 PMID: 15316743

23. Bisdas S, Spicer K, Rumboldt Z. Whole-Tumor Perfusion CT Parameters and Glucose Metabolism Measurements in Head and Neck Squamous Cell Carcinomas: A Pilot Study Using Combined Positron-Emission Tomography/CT Imaging. Am J Neuroradiol AJNR. 2008; 29: 1376–1381. doi: 10.3174/ajnr.A1111 PMID: 18483187

24. Ahn SJ, Park M-S, Kim KA, Park JY, Kim I, Kang WJ, et al. ^{18}F-FDG PET metabolic parameters and MRI perfusion and diffusion parameters in hepatocellular carcinoma: a preliminary study. PloS One. 2013; 8: e71571. doi: 10.1371/journal.pone.0071571 PMID: 23940769

25. Cheng H-LM. Improved correlation to quantitative DCE-MRI pharmacokinetic parameters using a modified initial area under the uptake curve (mIAUC) approach. J Magn Reson Imaging. 2009; 30: 864–872. doi: 10.1002/jmri.21916 PMID: 19787732

26. Mills SJ, Soh C, Rose CJ, Cheung S, Zhao S, Parker GJM, et al. Candidate Biomarkers of Extravascular Extracellular Space: A Direct Comparison of Apparent Diffusion Coefficient and Dynamic Contrast-Enhanced MR Imaging—Derived Measurement of the Volume of the Extravascular Extracellular Space in Glioblastoma Multiforme. Am J Neuroradiol AJNR. 2010; 31: 549–553. doi: 10.3174/ajnr.A1844 PMID: 19850765

27. Chu J-P, Mak HK-F, Yau KK-W, Zhang L, Tsang J, Chan Q, et al. Pilot study on evaluation of any correlation between MR perfusion (Ktrans) and diffusion (apparent diffusion coefficient) parameters in brain tumors at 3 Tesla. Cancer Imaging. 2012; 12: 1–6. doi: 10.1102/1470-7330.2012.0001 PMID: 22275724

28. Choi HS, Kim AH, Ahn SS, Shin N, Kim J, Lee S-K. Glioma grading capability: comparisons among parameters from dynamic contrast-enhanced MRI and ADC value on DWI. Korean J Radiol. 2013; 14: 487–492. doi: 10.3348/kjr.2013.14.3.487 PMID: 23690718

29. Arlinghaus LR, Li X, Rahman AR, Welch EB, Xu L, Gore JC, et al. On the Relationship Between the Apparent Diffusion Coefficient and Extravascular Extracellular Volume Fraction in Human Breast Cancer. Magn Reson Imaging. 2011; 29: 630–638. doi: 10.1016/j.mri.2011.02.004 PMID: 21531106

30. Minn H, Lapela M, Klemi PJ, Grénman R, Leskinen S, Lindholm P, et al. Prediction of Survival with Fluorine-18-Fluoro-deoxyglucose and PET in Head and Neck Cancer. J Nucl Med. 1997; 38: 1907–1911. PMID: 9430467

31. Gu J, Khong P-L, Wang S, Chan Q, LAW W, Zhang J. Quantitative Assessment of Diffusion-Weighted MR Imaging in Patients with Primary Rectal Cancer: Correlation with FDG-PET/CT. Mol Imaging Biol. 2011; 13: 1020–1028. doi: 10.1007/s11307-010-0433-7 PMID: 20872077

32. Ho K-C, Lin G, Wang J-J, Lai C-H, Chang C-J, Yen T-C. Correlation of apparent diffusion coefficients measured by 3T diffusion-weighted MRI and SUV from FDG PET/CT in primary cervical cancer. Eur J Nucl Med Mol Imaging. 2009; 36: 200–208. doi: 10.1007/s00259-008-0936-5 PMID: 18779960

33. Schmidt H, Brendle C, Schraml C, Martirosian P, Bezrukov I, Hetzel J, et al. Correlation of Simultaneously Acquired Diffusion-Weighted Imaging and 2-Deoxy-[18F] fluoro-2-D-glucose Positron Emission Tomography of Pulmonary Lesions in a Dedicated Whole-Body Magnetic Resonance/Positron Emission Tomography System. Invest Radiol. 2013; 48: 247–255. doi: 10.1097/RLI.0b013e31828d56a1 PMID: 23519008

34. Regier M, Derlin T, Schwarz D, Laqmani A, Henes FO, Groth M, et al. Diffusion weighted MRI and 18F-FDG PET/CT in non-small cell lung cancer (NSCLC): Does the apparent diffusion coefficient (ADC) correlate with tracer uptake (SUV)? Eur J Radiol. 2012; 81: 2913–2918. doi: 10.1016/j.ejrad.2011.11.050 PMID: 22197090

35. Nakajo M, Kajiya Y, Kaneko T, Kaneko Y, Takasaki T, Tani A, et al. FDG PET/CT and diffusion-weighted imaging for breast cancer: prognostic value of maximum standardized uptake values and apparent diffusion coefficient values of the primary lesion. Eur J Nucl Med Mol Imaging. 2010; 37: 2011–2020. doi: 10.1007/s00259-010-1529-7 PMID: 20607535

36. Choi SH, Paeng JC, Sohn C-H, Pagsisihan JR, Kim Y-J, Kim KG, et al. Correlation of 18F-FDG Uptake with Apparent Diffusion Coefficient Ratio Measured on Standard and High b Value Diffusion MRI in Head and Neck Cancer. J Nucl Med. 2011; 52: 1056–1062. doi: 10.2967/jnumed.111.089334 PMID: 21680692

37. Fruehwald-Pallamar J, Czerny C, Mayerhoefer ME, Halpern BS, Eder-Czembirek C, Brunner M, et al. Functional imaging in head and neck squamous cell carcinoma: correlation of PET/CT and diffusion-weighted imaging at 3 Tesla. Eur J Nucl Med Mol Imaging. 2011; 38: 1009–1019. doi: 10.1007/s00259-010-1718-4 PMID: 21465255

38. Varoquaux A, Rager O, Lovblad K-O, Masterson K, Dulguerov P, Ratib O, et al. Functional imaging of head and neck squamous cell carcinoma with diffusion-weighted MRI and FDG PET/CT: quantitative analysis of ADC and SUV. Eur J Nucl Med Mol Imaging. 2013; 40: 842–852. doi: 10.1007/s00259-013-2351-9 PMID: 23436068

39. Vandecaveye V, Dirix P, De Keyzer F, Op de Beeck K, Vander Poorten V, Hauben E, et al. Diffusion-weighted magnetic resonance imaging early after chemoradiotherapy to monitor treatment response in head-and-neck squamous cell carcinoma. Int J Radiat Oncol Biol Phys. 2012; 82: 1098–1107. doi: 10.1016/j.ijrobp.2011.02.044 PMID: 21514067

40. Powell C, Schmidt M, Borri M, Koh D-M, Partridge M, Riddell A, et al. Changes in functional imaging parameters following induction chemotherapy have important implications for individualised patient-based treatment regimens for advanced head and neck cancer. Radiother Oncol. 2013; 106: 112–117. doi: 10.1016/j.radonc.2012.09.009 PMID: 23089306

41. Kostakoglu L, Goldsmith SJ. PET in the assessment of therapy response in patients with carcinoma of the head and neck and of the esophagus. J Nucl Med. 2004; 45: 56–68. PMID: 14734674

2.4. Simultane 18F-FDG PET/MRT: Korrelation von scheinbarem Diffusionskoeffizient (ADC) und standardisiertem Aufnahmewert (SUV) beim primären und rezidivierten Zervixkarzinom

Derartige Analysen wurden nicht nur im Bereich der Kopf-Hals-Tumoren durchgeführt. In unserer Klinik wurden auch zahlreiche Patientinnen mit Zervixkarzinom untersucht. Bei einem Kollektiv von 14 Patientinnen mit primärem Zervixkarzinom und 17 Patientinnen mit einem lokalen Rezidiv wurden die funktionellen Daten zum Glukosestoffwechsel mit den Diffusionseigenschaften des Tumorgewebes verglichen und auf Korrelationen getestet.

Die Frage, ob diese beiden Eigenschaften von Tumorgewebe gleichsinnige oder sich ergänzende Informationen liefert, wurde in bisherigen Studien, die meist mit sequentiellen Untersuchungen durchgeführt worden waren, für verschiedene Tumorarten unterschiedlich beantwortet [136–139].

In unserer Patientinnengruppe konnten wir mit der simultanen Akquisition von Daten zur Glukoseutilisation und zur Diffusionsrestriktion eine inverse Korrelation der Parameter zeigen. Insgesamt wurden dafür 92 Läsionen ausgewertet, in diesem Fall waren also sowohl Primärtumoren als auch Lymphknotenmetastasen in die Auswertung eingegangen [140].

Der Artikel wird als vierter Teil der Habilitationsschrift beigefügt.

Brandmaier, Philipp; Purz, Sandra; Bremicker, Kristina; Höckel, Michael; Barthel, Henryk; Kluge, Regine; Kahn, Thomas; Sabri, Osama; *Stumpp, Patrick* (2015):
Simultaneous [18F]FDG-PET/MRI: Correlation of Apparent Diffusion Coefficient (ADC) and Standardized Uptake Value (SUV) in Primary and Recurrent Cervical Cancer.
PloS one 10 (11), S. e0141684.

Simultaneous [18F]FDG-PET/MRI: Correlation of Apparent Diffusion Coefficient (ADC) and Standardized Uptake Value (SUV) in Primary and Recurrent Cervical Cancer

P. Brandmaier[1☯]*, S. Purz[2☯], K. Bremicker[1], M. Höckel[3], H. Barthel[2], R. Kluge[2], T. Kahn[1], O. Sabri[2], P. Stumpp[1]

1 Department of Diagnostic and Interventional Radiology, University Hospital Leipzig, Leipzig, Germany,
2 Department of Nuclear Medicine, University Hospital Leipzig, Leipzig, Germany, 3 Department of Gynecology and Obstetrics, University Hospital Leipzig, Leipzig, Germany

☯ These authors contributed equally to this work.
* philipp.brandmaier@medizin.uni-leipzig.de

Abstract

Objectives

Previous non–simultaneous PET/MR studies have shown heterogeneous results about the correlation between standardized uptake values (SUVs) and apparent diffusion coefficients (ADCs). The aim of this study was to investigate correlations in patients with primary and recurrent tumors using a simultaneous PET/MRI system which could lead to a better understanding of tumor biology and might play a role in early response assessment.

Methods

We included 31 patients with histologically confirmed primary (n = 14) or recurrent cervical cancer (n = 17) who underwent simultaneous whole-body ^{18}F-FDG-PET/MRI comprising DWI. Image analysis was performed by a radiologist and a nuclear physician who identified tumor margins and quantified ADC and SUV. Pearson correlations were calculated to investigate the association between ADC and SUV.

Results

92 lesions were detected. We found a significant inverse correlation between SUV_{max} and ADC_{min} (r = -0.532, $p = 0.05$) in primary tumors as well as in primary metastases (r = -0.362, $p = 0.05$) and between SUV_{mean} and ADC_{min} (r = -0.403, $p = 0.03$). In recurrent local tumors we found correlations for SUV_{max} and ADC_{min} (r = -0.747, $p = 0.002$) and SUV_{mean} and ADC_{min} (r = -0.773, $p = 0.001$). Associations for recurrent metastases were not significant (p>0.05).

Conclusions

Our study demonstrates the feasibility of fast and reliable measurement of SUV and ADC with simultaneous PET/MRI. In patients with cervical cancer we found significant inverse

correlations for SUV and ADC which could play a major role for further tumor characterization and therapy decisions.

Key Point 1

This study investigates the correlation of functional parameters in a simultaneous PET/MRI.

Key Point 2

We found significant inverse correlations between ADC and SUV in cervical carcinoma which could increase knowledge about tumor biology.

Introduction

According to global cancer statistics, cervical carcinoma is one of the most frequent cancers diagnosed in women [1]. Thorough clinical investigations and a precise initial staging are mandatory to assess local tumor extension and possible lymph node infiltration. Currently, sophisticated routine clinical imaging to stage cervical cancer patients is primarily performed with high resolution pelvic magnetic resonance imaging (MRI). According to the European Society for Medical Oncology (ESMO) guidelines [2], positron emission tomography (PET) is an adequate tool with high sensitivity and specificity to accurately delineate the extent of disease, especially in lymph nodes that are not macroscopically enlarged and in distant sites. Both PET and MRI provide functional parameters: standardized uptake value (SUV) for glucose metabolism from PET and apparent diffusion coefficient (ADC) measured with diffusion weighted imaging (DWI) for Brownian motion of water molecules in MRI. These measurements and the quantificiation of their correlation could add valuable information about tumor biology, which may contribute to a more sophisticated tumor characterization and finally could lead to a "tailored" therapy approach by estimating response behavior.

Measurement of SUV is commonly used as a semi-quantitative read-out of ^{18}F-FDG uptake to supplement visual interpretation of the PET images. For example it is described to be correlated with histopathological grade, tumor cellularity and proliferative activity in sarcomas [3]. Regarding cervical cancer correlation with tumor aggressiveness and prognosis is reported in literature [4,5].

Nowadays DWI in MRI serves as a promising tool for the assessment and analysis of cellularity and discrimination of therapy responders in a variety of malignant tumor entities [6,7,8]

Depending on the degree of differentiation, a statistically significant difference between the ADCs of well-/moderately differentiated (G1/2) tumors and poorly differentiated (G3) tumors has been described in previous works [9, 10].

However, there is an ongoing controversy about the correlation of the functional parameters SUV and ADC. This is as some groups reported an inverse correlation, e.g. in head and neck squamous cell carcinoma [11]. Other data, e.g. from breast cancer or head and neck cancer

patients, describe ADC and SUV as independent biomarkers [12,13] in non-simultaneous imaging environments. For cervical cancer, initial integrated PET/MR imaging results in 19 patients recently published by Grueneisen et al. revealed a significant and strong inverse correlation between SUV and ADC in primary tumors and associated primary lymph node metastases, but not in recurrent tumor lesions [14].

As compared to PET/CT simultaneous PET/MRI offers a new quality of hybrid cancer imaging by providing metabolic and high-resolution anatomic imaging with excellent soft tissue contrast. The aim of this study was to analyze a possible correlation of SUVs and ADC values derived from simultaneous PET/MRI in a larger and as such more representative population of patients with primary and recurrent tumors of the cervix uteri.

Materials and Methods

This prospective study was approved by the local ethics committee (Ethic Committee of the Medical Faculty, University of Leipzig, Käthe—Kollwitz—Street 82, 04109 Leipzig, Germany) and all patients gave written informed consent.

a) Patients

A total of 31 patients (range: 33–78y, mean ± sd: 55±13.7y) with primary (n = 14), or recurrent (n = 17) cervical cancer were examined employing a whole-body PET/MRI protocol over a time period of two years. Prior to the PET/MRI, all patients underwent a thorough clinical investigation by an experienced gynecologist. All tumors were histologically classified via tumor biopsy or intraoperative sampling (squamos cell carcinoma n = 25; adeno carcinomas n = 4; neuroendocrine tumors n = 2).

b) Whole-body PET/MRI

The simultaneous PET/MRI system (Magnetom Biograph mMR—Biograph, Siemens Healthcare Sector, Erlangen, Germany) used in this study comprises a 3T whole-body scanner and a PET scanner.

The whole body simultaneous PET/MRI scan was performed from the skull to the upper thigh with 5 minutes per bed position (head, neck, chest, abdomen, pelvis, upper thighs) with simultaneous image acquisition. PET images were reconstructed using the iterative ordered subset expectation maximization algorithm with 3 iterations and 21 subsets, a Gaussian filter with 4 mm full width at half maximum (FWHM), and a 256 x 256 image matrix. Attenuation correction of the PET data was performed using a four-tissue (fat, soft tissue, air, background) model attenuation map which was generated from a Dixon-Vibe MR sequence [15].

Image acquisition started on average 130 minutes after intravenous administration of a body weight-adapted dose of ^{18}F-FDG (4 MBq/kg, 192–442 MBq, mean±sd: 309±70.32 MBq) after a fasting period of at least 6 hours.

For whole-body MRI the following especially designed coils for PET/MRI were used: A spine coil and four body array coils were placed on the patient from the knee to the chest, the bed positions for head and neck imaging were covered using a dedicated head/neck coil. For procedural planning gradient-echo (GRE) localizer scans were used. In each PET bed position, the following four MR sequences were measured consecutively in free breathing (respiratory triggering was only used for the sequences in the abdominal bed position):

1. **T1w 3D GRE (Dixon-VIBE).** This obligatory sequence is used for attenuation correction of the PET images (coronal, TR 3.6 ms, TE 1.23ms, flip angle 10°, 128 slices, Slice thickness 2.6mm, FoV 500 x 500, voxel size 4.1 x 2.6 x 2.6mm, acquisition time 0:19 min/bed position.)

2. **T2w single-shot fast spin echo (HASTE).** For delineation of anatomy and gross pathology (transversal, TR 800 ms, TE 89 ms, flip angle 120°, 40 slices, Slice thickness 4mm, FoV 450 x 450, voxel size 1.8 x 1.4 x 4.0 mm, acquisition time 0:32 min/bed position).

3. **Diffusion-weighted echoplanar imaging (EPI-DWI).** For detection of restricted diffusion (monopolar sequence). B-values of 0 and 800 mm/s^2 were used with diffusion-sensitizing gradients applied in all three orthogonal directions (transversal, TR 6800 ms, TE 73 ms, 30 slices, Slice thickness 6mm, FoV 450 x 450, voxel size 3.1 x 1.6 x 5.0 mm, acquisition time 1:15 min/bed position).

4. **T2w-fat suppressed inversion recovery (TIRM).** As current standard in whole-body MR-based anatomy imaging (coronal, TR 2090 ms, TE 47 ms, flip angle 120°, 40 slices, Slice thickness 5mm, FoV 500 x 500, voxel size 4.3 x 3.5 x 6.0mm, acquisition time 1:00 min/bed position).

With the sequences described, a combined simultaneous whole-body PET/MR scan was realized within an average of 30 minutes examination time. Additionally we performed dedicated high—resolution pelvic MR-sequences to properly evaluate anatomical details and local tumor spread. However, these sequences were not used for image analysis or quantification of SUV or ADC.

c) Image Analysis

An experienced radiological (6 years experience in gynaecological imaging) and nuclear medicine reader (7 years experience in oncological image interpretation) analyzed the images using dedicated viewing software (Syngo.via®; Siemens, Healthcare Sector, Erlangen, Germany). Lesions with focal uptake greater than the surrounding tissue (based on visual qualitative analysis) were considered as suspicious for malignancy (Fig 1).

In 22 patients we could indentify multiple tumor-suspicious lesions. However, we only included tumor lesions, which could be detected in both modalities (SUV/ADC). Lesions that could only be detected in one imaging modality or were too small for reliable ADC measurements (<5mm) were not explicitly documented, so statements concerning interobserver agreement cannot be made. Detection of suspicious lymph nodes was mainly conducted via imaging (MR. PET-CT or PET/MR) according to FDG-uptake, size (>10mm), round shape or visible necrosis. To determine SUV_{max} and SUV_{mean}, margins of tumor lesions were identified in MR images (T2 –sequence) and a volume of interest (VOI) was placed in the attenuation corrected PET dataset around the tumour (SUVmax threshold 40%). Region of interests (ROI) were then manually placed one each slice in the corresponding ADC map by the radiological reader (Fig 2). In order to ensure proper positioning of the ROI, identification of the tumor lesion was first conducted in a fused PET/T2w–Haste sequence, defining target lesions with high FDG uptake. However, analyzing small lesions (<10mm) was conducted via manual adjustment of polygonal ROIs, as the volume based method could not be applied sufficiently here. In some cases, however, minor manual adjustments (due to subtle misregistrations between PET and ADC) needed to be performed to guarantee an optimal ROI placement for the ADC measurement. As previously described in the literature, the main factors for misalignment in echo-planar imaging sequences are eddy current-induced image distortion and nonlinearities of the gradient coils [16].

To investigate a potential correlation between the SUV and ADC values, ADC maps were generated by the scanner software (syngo.via, Siemens, Erlangen, Germany) using two b—values (b = 0 s/mm2, b = 800 s/mm2). The following parameters were defined: ADC_{mean} as average ADC value for all voxels in each analyzed lesion and minimum ADC (ADC_{min}) as the
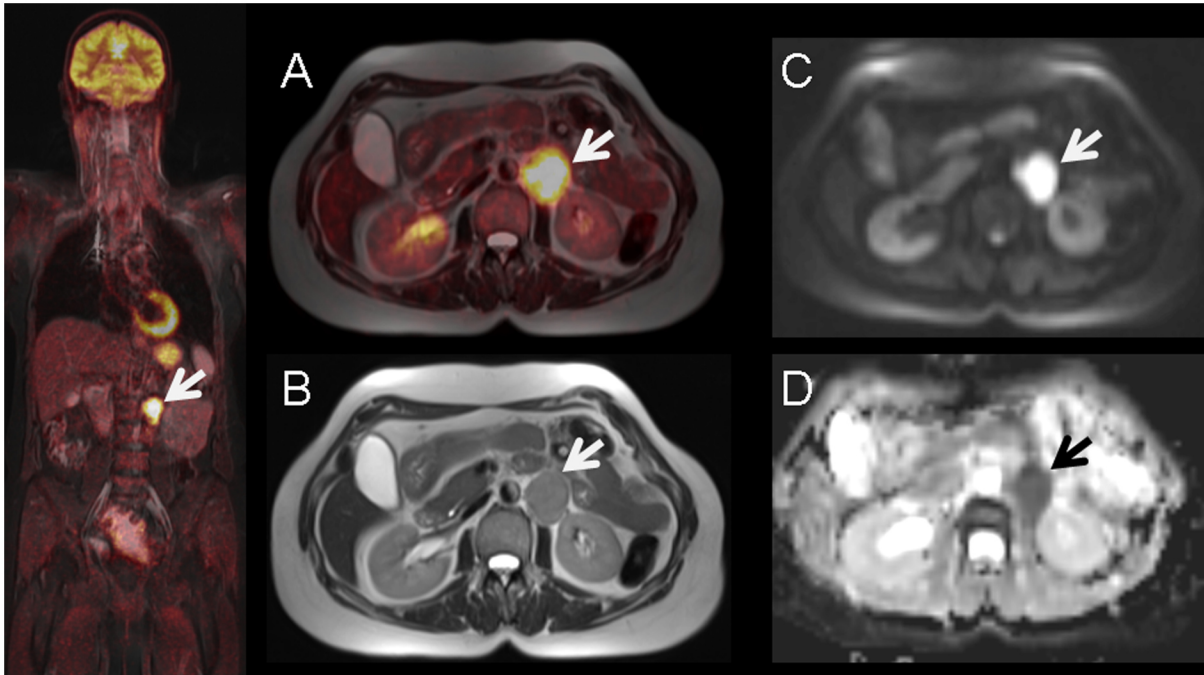
Fig 1. 56-year old female with histology proven recurrent lymph node metastasis of cervical cancer diagnosed 3 years before. Pre-operative simultaneous ^{18}F-FDG-PET/MRI (A) and T2-weighted MR imaging (B) show a hypermetabolic left paraaortal metastastic lymph node (arrow) with corresponding diffusion-restriction in DWI (C) and ADC-map (D).

doi:10.1371/journal.pone.0141684.g001

lowest ADC value among all. For PET maximum SUV (SUV_{max}) and mean SUV (SUV_{mean}) were recorded for all tumor lesions.

d) Statistics

Statistical analysis was performed using IBM SPSS 20™ (SPSS Inc., Chicago, IL, USA). Data are presented as mean +/- standard deviation (SD). Descriptive analysis was used for SUV_{max}, SUV_{mean}, ADC_{mean} and ADC_{min} of primary or recurrent tumor tissue and/or lymph nodes/metastasis separately. To estimate a correlation between ADC and SUV correlation pairs were
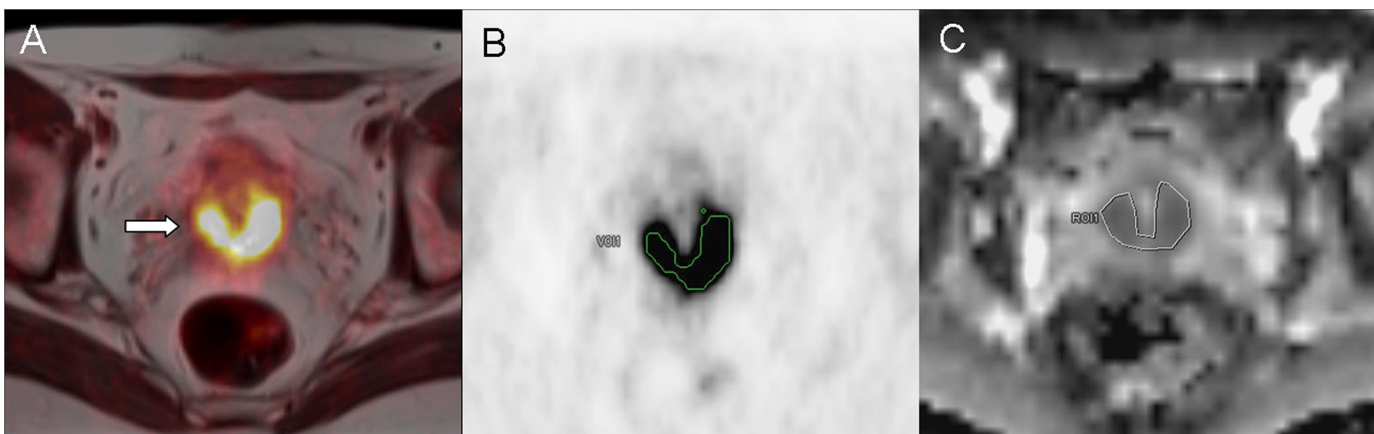
Fig 2. Lesion detection and definition of tumor margins (arrow) of primary cervical cancer in fused PET/MRI T2 –HASTE–sequence (A). Manual placement of a polygonal VOI in attenuation corrected PET images (B). ROI adjustment by manual segmentation on (C) the corresponding MRI ADC—map.
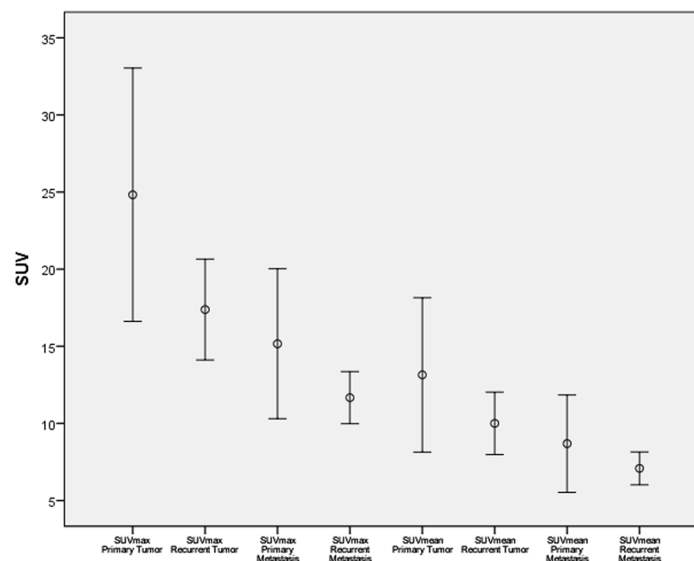
doi:10.1371/journal.pone.0141684.g002

analyzed using Pearson's correlation test. According to the classification system provided by Salkin, r values between 0.8–1.0 represent a very strong correlation, between 0.6 and 0.8 a strong correlation, between 0.4 and 0.6 a moderate correlation and between 0.2 and 0.4 a weak correlation. Values between 0.0 and 0.2 are classified as showing a weak or no relationship [17]. P values ≤ 0.05 were considered as statistically significant.

Results

All 31 patients successfully completed the whole-body PET/MRI examinations without any relevant side effects in an appropriate examination time of 30 minutes on average for whole body imaging. A total of 92 cancerous lesions were detected by simultaneous PET/MRI: primary tumors (n = 14), primary metastasis (n = 29 lymph nodes) recurrent tumors (n = 14) or recurrent metastasis (n = 35; 34 lymph nodes and 1 liver metastasis). Values for SUV and ADC (see S1 File) of these lesions are demonstrated in Figs 3 and 4 respectively. For primary tumors, mean values were 24.8±14.2 for SUV_{max} and 13.1±8.7 for SUV_{mean}, for primary metastasis 13.5 ±6.6 for SUV_{max} and 8.0±4.3 for SUV_{mean}, for recurrent tumors 17.4±5.7 for SUV_{max} and 10.0 ±3.5 for SUV_{mean} and for recurrent metastasis 14.5 ± 5.8 for SUV_{max} and 8.3±3.6 for SUV_{mean}. There was a significant difference between SUVmax of primary tumors and SUVmax of recurrent tumors *(p<0.05)* but not between primary and recurrent metastases *(p = 0.39)*.

Assessment of ADC in primary tumors showed values of 0.62±0.17 x 10^{-3} mm/s² for ADC_{min} and 1.02±0.14 x 10^{-3} mm/s² for ADC_{mean}. In primary metastases values amounted to 0.64±0.16 x 10^{-3} mm/s² for ADC_{min} and 1.22±0.24 x 10^{-3} mm/s² for ADC_{mean}. Analysis of ADC parameters for recurrent tumors revealed average values of 0.62±0.18 x 10^{-3} mm/s² for ADC_{min} and 1.11±0.11 x 10^{-3} mm/s² for ADC_{mean} whereas recurrent metastatic disease showed values for ADC_{min} of 0.68±0.18 x 10^{-3} mm/s² and 1.15±0.23 x 10^{-3} mm/s² for ADC_{mean}. Overall there was no significant difference between ADC values of primary or recurrent disease.
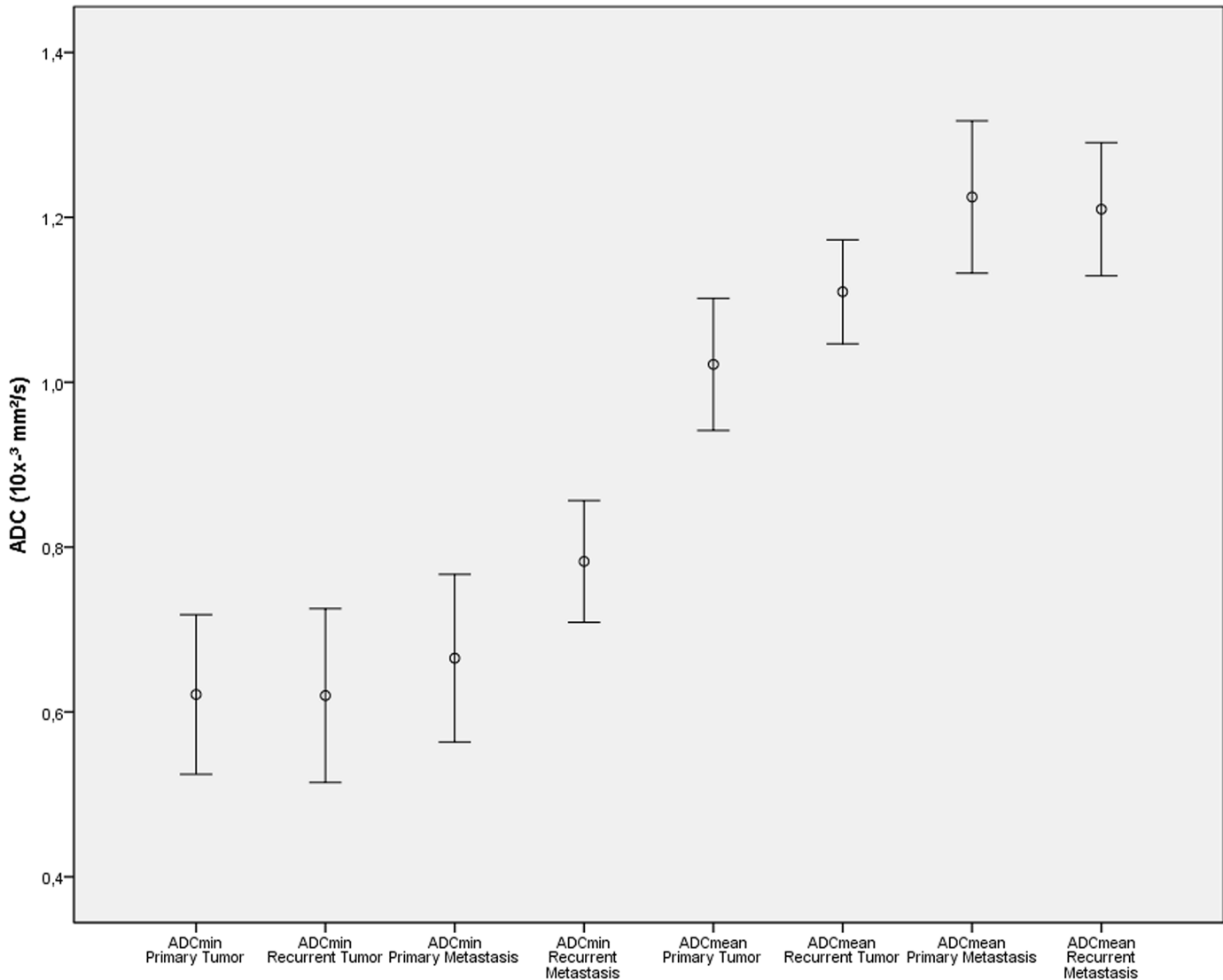
Correlation analysis revealed a moderate significant inverse correlation in primary tumors (see Fig 5) for SUV_{max} versus ADC_{min} (r = -0.532, *p = 0.05*). The association between SUV_{mean}

Fig 3. Absolute SUV of primary and recurrent cervical cancer/metastasis presented through error bars.

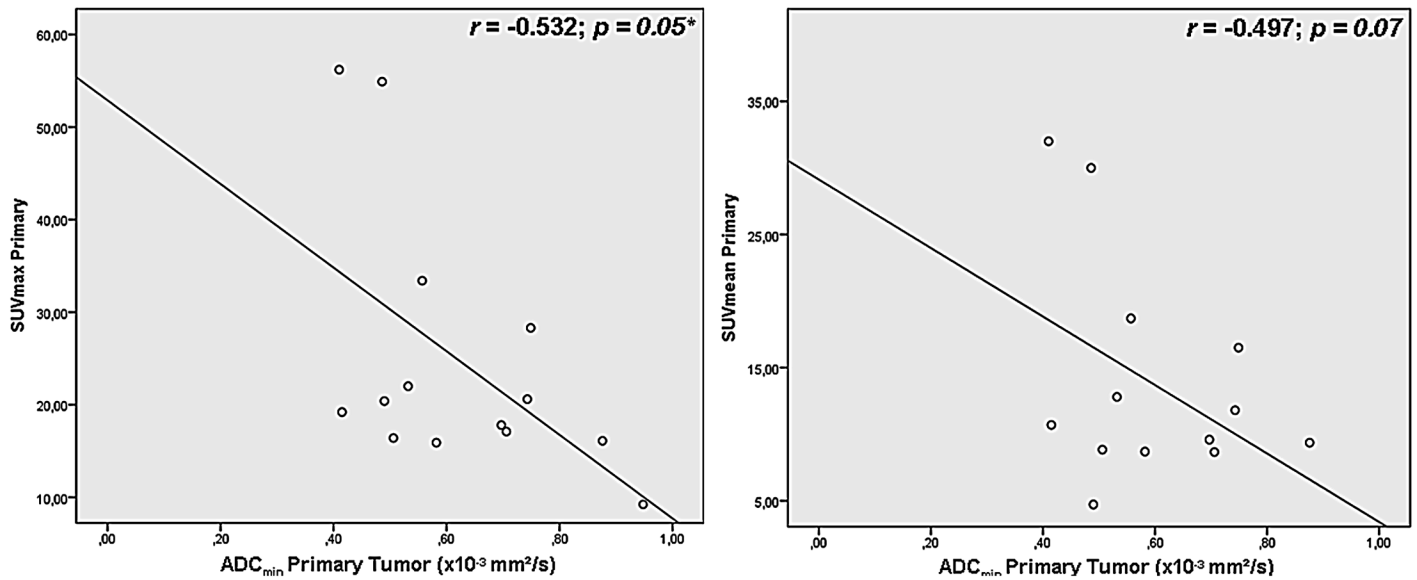doi:10.1371/journal.pone.0141684.g003

Fig 4. Absolute ADC values of primary and recurrent cervical cancer/metastasis presented through error bars.

versus ADC_{min} (see Fig 5), SUV_{mean} versus ADC_{mean} and SUV_{max} versus ADC_{mean} missed the significance threshold and showed weak correlations ($r = -0.497$, $p = 0.07$; $r = -0.011$, $p = 0.09$; $r = 0.077$, $p = 0.79$). Primary metastasis showed weak inverse correlations for SUV_{max} and ADC_{min} ($r = -0.362$, $p = 0.05$, see Fig 6) and moderate correlations for SUV_{mean} and ADC_{min} ($r = -0.403$, $p = 0.03$, see Fig 6)–no inverse correlations were found for SUV_{mean} versus ADC_{mean} and SUV_{max} versus ADC_{mean} ($r = 0.209$ $p = 0.28$; $r = 0.224$, $p = 0.243$).

In recurrent local tumor sites we found strong correlations for SUV_{max} versus ADC_{min} ($r = -0.747$, $p = 0.002$, see Fig 7) and between SUV_{mean} and ADC_{min} ($r = -0.773$, $p = 0.001$, see Fig 7). Weak, non—significant correlations were found for SUV_{mean} versus ADC_{mean} and SUV_{max} versus ADC_{mean} ($r = -0.391$ $p = 0.16$; $r = -0.352$ $p = 0.22$).

In recurrent metastases, SUV_{max} and SUV_{mean} showed no inverse correlation with ADC_{min} ($r = -0.46$, $p = 0.79$ and $r = +0.81$, $p = 0.65$, graphs not shown) nor with ADC_{mean} ($r = 0.20$ $r = 0.229$; $p = 0.25$ $p = 0.19$).

Fig 5. Correlation analysis of different SUV and ADC in primary tumors.

doi:10.1371/journal.pone.0141684.g005

Discussion

With the recent development of integrated PET/MRI scanners, new possibilities for quantitative molecular imaging have emerged. PET/MRI enables multimodal analysis of simultaneously acquired functional parameters which may contribute to a more sophisticated characterization of tumor biology and may also help to identify markers to predict response to therapy [18, 19].
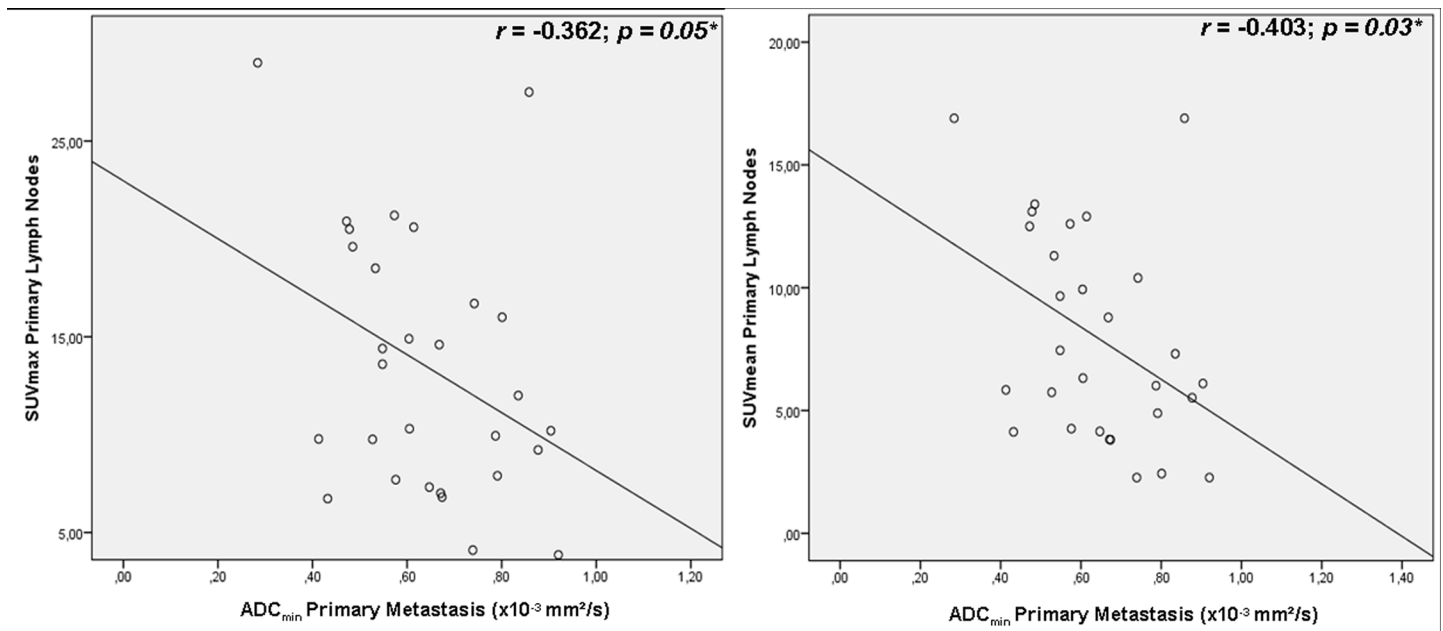
Fig 6. Correlation of SUV and ADC in primary metastasis.

doi:10.1371/journal.pone.0141684.g006
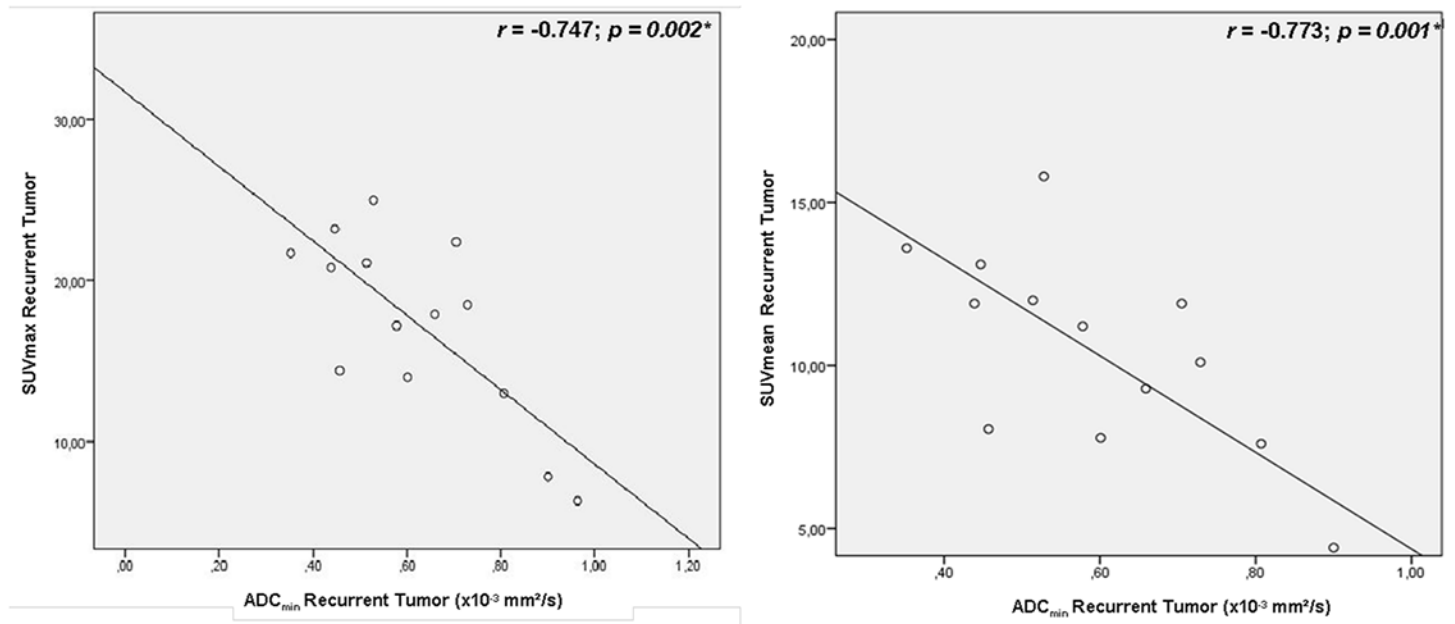
Fig 7. Correlation of SUV and ADC in recurrent tumor sites.

doi:10.1371/journal.pone.0141684.g007

Integration of DWI into diagnostic MR was initially used for stroke detection [20]. DWI hereby provides valuable information about the Brownian motion of water molecules (diffusion). Quantitative ADC values have been demonstrated to be negatively correlated with cellularity, yielding lower ADC values for various malignancies compared to surrounding healthy, inflammatory or scar tissue [21, 22]. In light of that, quantification and assessment of ADC might become a valuable tool for tumor delineation, tumor characterization and evaluation of therapy response [6, 9].

[18F-]FDG uptake correlates with the number of viable tumor cells and the resulting semi-quantitative read-out parameter SUV serves as a key player in oncologic imaging as it is the main non-invasive approach to quantify glucose metabolism. In numerous malignancies, 18F-FDG-PET is a useful tool to predict early response to therapy. A normalization of initial pathological 18F-FDG uptake and a significant SUV-decrease, respectively at an early stage of therapy is associated with an excellent prognosis and may help to identify patients who might benefit from de-escalation of antineoplastic therapy e.g. in lymphoma and non-small-lung cancer [23,24,25].

Both, ADC derived by DWI and SUV from [18 F-] FDG PET are described to be useful parameters for characterization of tumor lesions and for assessments of treatment response [26]. However, the benefit of using both parameters complementary in the diagnosis of malignant tumors and for response assessment remains unclear.

In our study, individual assessment of [18F]FDG SUVs showed significant differences between primary tumors and primary metastases. Kidd et al. [27] evaluated the prognostic significance of SUV_{max} in pelvic lymph node metastases in patients with cervical cancer and found similar results with higher values for primary cervical tumors (average SUV_{max} = 14) in comparison to primary pelvic lymph node metastases (average SUV_{max} = 6.9). Furthermore, SUV of pelvic lymph node metastases was found to be predictive for treatment response in the same study as well as pelvic recurrence risk and disease-specific survival in patients with cervical cancer during a mean follow-up time of 18 months.

Quantitative analysis of ADC has been performed in several studies for characterization and treatment response assessment in cervical cancer. Xue et al. [28] concluded that ADC values are helpful in assessing pathological subtypes and in differentiating cervical cancers by showing significantly different values for ADC_{mean} and ADC_{min} for adenocarcinomas, squamous cell carcinomas or poorly differentiated tumors. Another uni-modal MRI study dealing with the value of DWI in diagnosis of lymph node metastasis in patients with cervical cancer [29] showed a statistically significant difference in ADC_{mean} and ADC_{min} between metastatic and non-metastatic lymph nodes. In our study we could not find significant differences between ADC values of primary/recurrent tumors compared to primary/recurrent metastases.

Our study demonstrated an inverse correlation between SUVs and ADC values in primary and recurrent tumors. This main study finding in the largest cohort of cervical cancer patients so far imaged by integrated PET/MRI is supporting the theory of decreased ADC values which is indicating increased cellularity [9]. Similar findings [5] show that an increased FDG uptake also correlates with high cellularity of viable tumor cells and high tissue metabolism. Regarding the overall correlation of these two distinct parameters, existing literature describes inhomogeneous results for non-simultaneous image acquisition with PET/CT and standalone MRI for assessment of absolute $SUV_{max/mean}$ and $ADC_{min/mean}$ values [30, 13]. However, Ho et al. [30] demonstrated a significant inverse correlation between the $rADC_{min}$, which is the relative ADC defined by ADC_{min}/ADC_{mean}, and SUV_{max} in primary cervical cancer with sequential PET/CT and MR. In a study performed by Nakajo et al. [31], 44 patients with breast cancer received a preoperative PET/CT and MRI (including DWI) within an average of 17 days between both. SUV_{max} and ADC ($r = -0.486$, $p = 0.001$) were significantly associated with histological grade, nodal status and vascular invasion. In another study by Mori et al. [32], a total of 104 patients with malignant pulmonary nodules were examined by PET/CT and MRI within a 2-week period showing an inverse correlation between SUV_{max} and ADC_{min}. Contrary to these results, other data for breast tumor patients examined with PET/CT and MRI indicate only a weak, non-significant inverse association [33]. For head and neck tumors, Varoquaux et al. [13] described ADC and SUV as independent biomarkers. In contrast to these studies, in our study SUV and ADC were determined simultaneously with an integrated PET/MRI resulting in reduced registration artifacts due to an exact image fusion. Recently published data about the correlation of ADC and SUV in simultaneous PET/MRI imaging show significant inverse correlations between the ADC_{mean} and SUV_{max} in non-small cell lung cancer [34, 35] and an inverse correlation between SUV_{max} and ADC_{min} in a patient cohort of 19 women suffering from cervical carcinoma [14]. Compared to the latter study our results indicate almost similar correlations between the SUV and ADC of patients with cervical carcinomas and FDG-avid lymph nodes. This was even though ADC quantification is known to be susceptible to physical alterations depending on the choice of the b-values, which were slightly different in the above study [14]. Compared to the above-mentioned study of Ho et al. [30], where only the rSUV and rADC seemed to correlate inversely, we found a direct inverse correlation of SUV and ADC. Demonstrating an overall inverse correlation we found the highest correlation coefficients for SUV_{max} vs. ADC_{min} and SUV_{mean} vs. ADC_{min} for recurrent cervical cancer and weaker associations for primary cervical tumor sites. These findings might indicate differences within the genomic profile of primary and recurrent cervical cancer. As described by Martin et al. [36] and Hagemann et al. [37] genomic profiling and identification of different biomarkers are important to understand the pathogenesis of cervical cancer. Hagemann et al. tried to identify in both, lymph node micrometastases and recurrent cervical tumours up- or downregulated genes involved in several molecular pathways such as angiogenesis, oncogenic pathways, DNA repair mechanisms, migration, cell proliferation and apoptosis. The authors described, that in lymph node micrometastases most genes were downregulated or showed

expressions equal to the levels found in matched primary cervical cancer. In recurrent cancer, almost all genes were upregulated at least two-fold compared to the expression profiles of primary cervical tumours, according to the authors possibly reflecting their aggressive biological behavior. Only two genes, the proapoptotic gene BAX and the tumour suppressor gene APC has been found to be consistently downregulated in lymph node metastases and recurrent cervical cancer [37]. Regarding our results, the stronger association of glucose metabolism and cellularity in recurrent cervical cancer compared to primary cervical cancer might also be influenced by different levels of gene expression in several molecular pathways.

As also described by Vanderhoek et al. [38], different SUV measures (SUVmax, SUVmean or SUVpeak) assess different tumor characteristics. SUVmax is measuring the tumor region of most intense metabolism, while SUVmean assesses overall metabolism in the tumor. As tumors tend to be heterogeneous, average metabolism and also average response to therapy of the entire tumor might be different from metabolism of one particular subregion within the tumor.

Assessment of tumor characteristics and treatment response using multiple SUV measures may offer a more complete tumor characterization. Furthermore, a combination of SUV measures might provide a more detailed tumor characterization.

SUVmean is described to have better reproducibility than SUVmax, which probably gives a less accurate result since SUVmax is only a single voxel-derived value. Regarding our results, the demonstrated significant inverse correlation between SUVmax and ADCmin in primary cervical cancer (without a significant association between SUVmean and ADCmin) might not be as robust as the significant inverse correlation of both, SUVmax and ADCmin and SUVmean and ADCmin in primary metastases.

This study has limitations that may have impacted the results. A direct histopathological or immunohistochemistry correlation was not performed but possibly would provide even deeper insights into tumor proliferation and thus the correlation of multifunctional PET/MR parameters. Another limitation is that only lesions were included that could be detected on both modalities. However, as we wanted to investigate a potential correlation of these parameters in a simultaneous hybrid system we needed to include only lesion visible in both modalities. Furthermore, due to performance of PET/CT prior to PET/MRI in our patient cohort, the average uptake time for FDG in PET/MRI is approximately 130 minutes, which could probably influence SUV measurements.

Conclusion

The current study demonstrates the feasibility of a fast, reliable and simultaneous measurement of SUV and ADC values in an integrated PET/MRI. We found significant inverse correlations between SUV and ADC values in patients with primary or recurrent cervical cancer and metastases. The correlation of these parameters may contribute to a more sophisticated characterization of tumor biology in cervical cancer.

Supporting Information

S1 File. Datasheet containing Supporting Information for ADC and SUV.
(XLS)

Author Contributions

Conceived and designed the experiments: PB SP PS. Performed the experiments: PB SP KB. Analyzed the data: PB SP PS. Contributed reagents/materials/analysis tools: PB SP KB MH HB RK TK OS PS. Wrote the paper: PB SP KB MH HB RK TK OS PS.

References

1. Jemal A, Bray F, Center MM, Ferlay J, Ward E, Forman D. Global cancer statistics. CA Cancer J Clin 2011; 61: 69–90. doi: 10.3322/caac.20107 PMID: 21296855

2. Colombo N, Carinelli S, Colombo A, Marini C, Rollo D, Sessa C. ESMO Guidelines Working Group. Cervical cancer: ESMO Clinical Practice Guidelines for diagnosis, treatment and follow up. Ann Oncol. 2012; Suppl 7: : vii27–32. PMID: 22997451

3. Folpe AL, Lyles RH, Sprouse JT, Conrad EU 3rd, Eary JF. (F-18) fluorodeoxyglucose positron emission tomography as a predictor of pathologic grade and other prognostic variables in bone and soft tissue sarcoma. Clin Cancer Res. 2000 Apr 6; 4: 1279–1287.

4. Xue F, Lin LL, Dehdashti F, Miller TR, Siegel BA, Grigsby PW. F-18 fluorodeoxyglucose uptake in primary cervical cancer as an indicator of prognosis after radiation therapy. Gynecol Oncol 2006; 101: 147–151. PMID: 16263155

5. Lee YY, Choi CH, Kim CJ, Kang H, Kim TJ, Lee JW, et al. The prognostic significance of the SUVmax (maximum standardized uptake value for F-18 fluorodeoxyglucose) of the cervical tumor in PET imaging for early cervical cancer: preliminary results. Gynecol Oncol. 2009; 115(1): 65–68. doi: 10.1016/j.ygyno.2009.06.022 PMID: 19604567

6. Levy A, Caramella C, Chargari C, Medjhoul A, Rey A, Zareski E, et al. Accuracy of Diffusion-Weighted Echo-Planar MR Imaging and ADC Mapping in the evaluation of residual Cervical Carcinoma after radiation therapy. Gynecol Oncol. 2011; 123(1): 110–115. doi: 10.1016/j.ygyno.2011.06.009 PMID: 21764110

7. Horger M, Claussen C, Kramer U, Fenchel M, Lichy M, Kaufmann S. Very early indicators of response to systemic therapy in lymphoma patients based on alterations in water diffusivity—a preliminary experience in 20 patients undergoing whole-body diffusion-weighted imaging. Eur J Radiol. 2014; 83(9): 1655–1664. doi: 10.1016/j.ejrad.2014.05.027 PMID: 24972451

8. Jung SH, Heo SH, Kim JW, Jeong YY, Shin SS, Soung MG, et al. Predicting response to neoadjuvant chemoradiation therapy in locally advanced rectal cancer: diffusion-weighted 3 Tesla MR imaging. J Magn Reson Imaging. 2012; 35(1):110–116. doi: 10.1002/jmri.22749 PMID: 21989997

9. Kuang F, Jing R, Qun Z, Fu L, Yi H, Ziqian C. The value of apparent diffusion coefficient in the assessment of cervical cancer. Eur Radiol 2013; 23:1050–1058. doi: 10.1007/s00330-012-2681-1 PMID: 23179520

10. Rakheja R, Makis W, Skamene S, Nahal A, Brimo F, Azoulay L, et al. Correlating metabolic activity on 18F-FDG PET/CT with histopathologic characteristics of osseous and soft-tissue sarcomas: a retrospective review of 136 patients. AJR Am J Roentgenol. 2012; 198(6): 1409–1416. doi: 10.2214/AJR.11.7560 PMID: 22623556

11. Nakajo M, Nakajo M, Kajiya Y, Tani A, Kamiyama T, Yonekura R, et al. FDG PET/CT and diffusion-weighted imaging of head and neck squamous cell carcinoma: comparison of prognostic significance between primary tumor standardized uptake value and apparent diffusion coefficient. Clin Nucl Med. 2012; 37(5): 475–480. doi: 10.1097/RLU.0b013e318248524a PMID: 22475897

12. Choi BB, Kim SH, Kang BJ, Lee JH, Song BJ, Jeong SH, et al. Diffusion weighted imaging and FDG PET/CT: predicting the prognoses with apparent diffusion coefficient values and maximum standardized uptake values in patients with invasive ductal carcinoma. World J Surg Oncol. 2012; 10: 126. doi: 10.1186/1477-7819-10-126 PMID: 22741544

13. Varoquaux A, Rager O, Lovblad KO, Masterson K, Dulguerov P, Ratib O, et al. Functional imaging of head and neck squamous cell carcinoma with diffusion-weighted MRI and FDG PET/CT: quantitative analysis of ADC and SUV. Eur J Nucl Med Mol Imaging. 2013; 40(6): 842–852. doi: 10.1007/s00259-013-2351-9 PMID: 23436068

14. Grueneisen J, Beiderwellen K, Heusch P, Buderath P, Aktas B, Gratz M, et al. Correlation of standardized uptake value and apparent diffusion coefficient in integrated whole-body PET/MRI of primary and recurrent cervical cancer. PLoS One. 2014; 9(5): e96751. doi: 10.1371/journal.pone.0096751 PMID: 24804676

15. Martinez-Möller A, Souvatzoglou M, Delso G, Bundschuh RA, Chefd'hotel C, Ziegler SI, et al. Tissue classification as a potential approach for attenuation correction in whole-body PET/MRI: evaluation with PET/CT data. J Nucl Med. 2009; 50(4): 520–526. doi: 10.2967/jnumed.108.054726 PMID: 19289430

16. Rakheja R, DeMello L, Chandarana H, Glielmi C, Geppert C, Faul D, et al. Comparison of the accuracy of PET/CT and PET/MRI spatial registration of multiple metastatic lesions. AJR Am J Roentgenol. 2013; 201(5): 1120–1123. doi: 10.2214/AJR.13.11305 PMID: 24147486

17. Chung M. Correlation Coefficient. In: Salkin NJ, editor. Encyclopedia of Measurement and Statistics London: Sage Publications; 2007. pp. 189–201.

18. Yankeelov TE, Peterson TE, Abramson RG, Izquierdo-Garcia D, Arlinghaus LR, Li X, et al. Simultaneous PET-MRI in oncology: a solution looking for a problem? Magn Reson Imaging. 2012; 30(9): 1342–1356. doi: 10.1016/j.mri.2012.06.001 PMID: 22795930

19. Punwani S, Taylor SA, Saad ZZ, Bainbridge A, Groves A, Daw S, et al. Diffusion-weighted MRI of lymphoma: prognostic utility and implications for PET/MRI? Eur J Nucl Med Mol Imaging. 2013; 40(3): 373–385. doi: 10.1007/s00259-012-2293-7 PMID: 23197155

20. Le Bihan, D. MR Imaging of intravoxel incoherent motions: application to diffusion and perfusion in neurologic disorders. Annual Meeting of the RSNA, Chicago. 1985.

21. Liu Y, Liu H, Bai X, Ye Z, Sun H, Bai R, et al. Differentiation of metastatic from non-metastatic lymph nodes in patients with uterine cervical cancer using diffusion-weighted imaging. Gynecol Oncol. 2011; 122: 19–24. doi: 10.1016/j.ygyno.2011.03.023 PMID: 21497384

22. Kim JK, Kim KA, Park BW, Kim N, Cho KS. Feasibility of diffusion weighted imaging in the differentiation of metastatic from nonmetastatic lymph nodes: early experience. J Magn Reson Imaging. 2008; 28: 714–719. doi: 10.1002/jmri.21480 PMID: 18777531

23. Cheson BD, Pfistner B, Juweid ME, Gascoyne RD, Specht L, Horning SJ, et al. International Harmonization Project on Lymphoma. Revised response criteria for malignant lymphoma. J Clin Oncol. 2007; 25(5): 579–586. PMID: 17242396

24. Hoekstra CJ, Stroobants SG, Smit EF, Vansteenkiste J, van Tinteren H, Postmus PE, et al. Prognostic relevance of response evaluation using [18F]-2-fluoro-2-deoxy-D-glucose positron emission tomography in patients with locally advanced non-small-cell lung cancer. J Clin Oncol. 2005; 23(33): 8362–8370. PMID: 16293866

25. Furth C, Steffen IG, Amthauer H, Ruf J, Misch D, Schönberger S, et al. Early and late therapy response assessment with [18F]fluorodeoxyglucose positron emission tomography in pediatric Hodgkin's lymphoma: analysis of a prospective multicenter trial. J Clin Oncol. 2009; 27(26): 4385–4391. doi: 10.1200/JCO.2008.19.7814 PMID: 19667276

26. Pahk K, Rhee S, Cho J, Seo M, Lee S, Park T, et al. The Role of Interim 18F-FDG PET/CT in Predicting Early Response to Neoadjuvant Chemotherapy in Breast Cancer. Anticancer Res. 2014; 34(8): 4447–4455. PMID: 25075084

27. Kidd EA, Siegel BA, Dehdashti F, Grigsby PW. Pelvic Lymph Node F-18 Fluorodeoxyglucose Uptake as a Prognostic Biomarker in Newly Diagnosed Patients With Locally Advanced Cervical Cancer. Cancer. 2010; 116(6): 1469–1475. doi: 10.1002/cncr.24972 PMID: 20108309

28. Xue H, Ren C, Yang J, Sun Z, Li S, Jin Z, et al. Histogram analysis of apparent diffusion coefficient for the assessment of local aggressiveness of cervical cancer. Arch Gynecol Obstet. 2014; 290(2): 341–348. doi: 10.1007/s00404-014-3221-9 PMID: 24687746

29. Zhang J, Ren C, Xue HD, Zhou HL, Sun ZY, Jin ZY. Value of diffusion-weighted imaging in diagnosis of lymph node metastasis in patients with cervical cancer. Zhongguo Yi Xue Ke Xue Yuan Xue Bao 2014; 36(1): 73–78. doi: 10.3881/j.issn.1000-503X.2014.01.014 PMID: 24581133

30. Ho KC, Lin G, Wang JJ, Lai CH, Chang CJ, Yen TC. Correlation of apparent diffusion coefficients measured by 3T diffusion-weighted MRI and SUV from FDG PET/CT in primary cervical cancer. Eur J Nucl Med Mol Imaging. 2009; 36(2): 200–208. doi: 10.1007/s00259-008-0936-5 PMID: 18779960

31. Nakajo M, Kajiya Y, Kaneko T, Kaneko Y, Takasaki T, Tani A, et al. FDG PET/CT and diffusion-weighted imaging for breast cancer: prognostic value of maximum standardized uptake values and apparent diffusion coefficient values of the primary lesion. Eur J Nucl Med Mol Imaging. 2010; 37(11): 2011–2020. doi: 10.1007/s00259-010-1529-7 PMID: 20607535

32. Mori T, Nomori H, Ikeda K, Kawanaka K, Shiraishi S, Katahira K, et al. Diffusion-weighted magnetic resonance imaging for diagnosing malignant pulmonary nodules/masses: comparison with positron emission tomography. J Thorac Oncol. 2008; 3(4): 358–364. doi: 10.1097/JTO.0b013e318168d9ed PMID: 18379353

33. Baba S, Isoda T, Maruoka Y, Kitamura Y, Sasaki M, Yoshida T, et al. Diagnostic and Prognostic Value of Pretreatment SUV in 18F-FDG/PET in Breast Cancer: Comparison with Apparent Diffusion Coefficient from Diffusion-Weighted MR Imaging. J Nucl Med. 2014; 55(5): 736–742. doi: 10.2967/jnumed.113.129395 PMID: 24665089

34. Schmidt H, Brendle C, Schraml C, Martirosian P, Bezrukov I, Hetzel J, et al. Correlation of simultaneously acquired diffusion-weighted imaging and 2-deoxy-[18F] fluoro-2-D-glucose positron emission tomography of pulmonary lesions in a dedicated whole-body magnetic resonance/positron emission tomography system. Invest Radiol 2013; 48(5): 247–255. doi: 10.1097/RLI.0b013e31828d56a1 PMID: 23519008

35. Heusch P, Buchbender C, Köhler J, Nensa F, Beiderwellen K, Kühl H, et al. Correlation of the apparent diffusion coefficient (ADC) with the standardized uptake value (SUV) in hybrid 18F-FDG PET/MRI in

non-small cell lung cancer (NSCLC) lesions: initial results. Röfo. 2013; 185(11): 1056–1062. doi: 10.1055/s-0033-1350110 PMID: 23860802

36. Martin CM, Astbury K, O'Leary JJ. Molecular profiling of cervical neoplasia. Expert Rev Mol Diagn. 2006; 6(2):217–229. PMID: 16512781

37. Hagemann T, Bozanovic T, Hooper S, Ljubic A, Slettenaar VI, Wilson JL, et al. Molecular profiling of cervical cancer progression. Br J Cancer. 2007; 96(2): 321–328. PMID: 17242701

38. Vanderhoek M, Perlman SB, Jeraj R. Impact of different standardized uptake value measures on PET-based quantification of treatment response. J Nucl Med. 2013; 54(8):1188–1194. doi: 10.2967/jnumed.112.113332 PMID: 23776199

2.5. Simultane 18F-FDG PET/MRT: Assoziationen zwischen Diffusion, Glukosemetabolismus und histopathologischen Parametern bei Patienten mit Plattenepithelkarzinomen der Kopf-Hals-Region

In Fortführung unserer Untersuchungen bei Kopf-Hals-Tumoren war der nächste Schritt, nicht nur die Parameter der hybriden Bildgebung miteinander zu korrelieren, sondern deren Übereinstimmung mit histopathologischen Parametern zu testen. Hierfür wurden Patienten mit primären Plattenepithelkarzinomen eingeschlossen. Bei diesen wurden aus den PET/MRT-Untersuchungen die funktionellen Parameter der Diffusion und des Glukosestoffwechsels im Tumor ermittelt. In Zusammenarbeit mit der Pathologie wurden aus den histopathologischen Untersuchungen diverse Parameter ermittelt, unter anderem die Zellzahl, die Kernfläche und der Proliferationsindex im Tumor.

In den folgenden Analysen zeigte sich, dass die Diffusionseigenschaften im Tumorgewebe, die mit dem ADC-Wert quantifiziert werden können, mit dem Proliferationsindex korrelieren. Eine Kombination der Parameter Diffusion und Glukosestoffwechsel (SUVmax/ADCmin) korreliert mit der durchschnittlichen Kernfläche im Tumor.

Künftige Untersuchungen an größeren Patientenkollektiven müssen zeigen, wie zuverlässig solche Vorhersagen zum Tumorverhalten aus der Bildgebung abzuleiten sind. Sollten sich diese Ergebnisse reproduzieren lassen, kommt man dem Ziel näher, auf Gewebeentnahmen zu verzichten und Therapieentscheidungen alleine anhand der Bildgebung treffen zu können.

Die genannte Studie wird als fünfter Teil der Habilitationsschrift aufgelistet [141].

Surov, Alexey; **Stumpp, Patrick;** *Meyer, Hans Jonas; Gawlitza, Matthias; Höhn, Anne-Kathrin; Boehm, Andreas; Sabri, Osama; Kahn, Thomas; Purz, Sandra* (2016):
Simultaneous [18F]FDG-PET/MRI: Associations between diffusion, glucose metabolism and histopathological parameters in patients with head and neck squamous cell carcinoma
Oral Oncology, http://dx.doi.org/10.1016/j.oraloncology.2016.04.009

Contents lists available at ScienceDirect

Oral Oncology
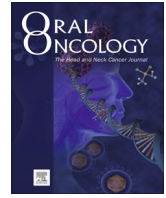
Simultaneous 18F-FDG-PET/MRI: Associations between diffusion, glucose metabolism and histopathological parameters in patients with head and neck squamous cell carcinoma

Alexey Surov [a,*], Patrick Stumpp [a], Hans Jonas Meyer [b], Matthias Gawlitza [a], Anne-Kathrin Höhn [c], Andreas Boehm [d], Osama Sabri [e], Thomas Kahn [a], Sandra Purz [e]

[a] Department of Diagnostic and Interventional Radiology, University Hospital of Leipzig, Liebigstrasse 20, 04103 Leipzig, Germany
[b] Department of Radiology, Martin-Luther-University Halle-Wittenberg, Ernst-Grube-Str. 40, 06097 Halle, Germany
[c] Department of Pathology, University Hospital of Leipzig, Liebigstrasse 20, 04103 Leipzig, Germany
[d] ENT Department, University Hospital of Leipzig, Liebigstrasse 10-14, 04103 Leipzig, Germany
[e] Department of Nuclear Medicine, University Hospital of Leipzig, Liebigstraße 18, 04103 Leipzig, Germany

ARTICLE INFO

SUMMARY

Objectives: To analyze possible associations between functional simultaneous 18F-FDG-PET/MR imaging parameters and histopathological parameters in head and neck squamous cell carcinoma (HNSCC).
Material and Methods: 11 patients (2 female, 9 male; mean age 56.0 years) with biopsy-proven primary HNSCC underwent simultaneous 18F-FDG-PET/MRI with a dedicated head and neck protocol including diffusion weighted imaging. For each tumor, glucose metabolism was estimated with standardized uptake values (SUV) and diffusion restriction was calculated using apparent diffusion coefficients (ADC). The tumor proliferation index was estimated on Ki 67 antigen stained specimens. Cell count, total nucleic area, and average nucleic area were estimated in each case. Pearson's correlation coefficient was used to analyze possible associations between the estimated parameters.
Results: The mean SUV_{max} value was 24.41 ± 6.51, and SUV_{mean} value 15.01 ± 4.07. Mean values ($\times 10^{-3}$ mm^2 s^{-1}) of ADC parameters were as follows: ADC_{min}: 0.65 ± 0.20; ADC_{mean}: 1.28 ± 0.18; and ADC_{max}: 2.16 ± 0.35. Histopathological analysis identified the following results: cell count 1069.82 ± 388.66, total nucleic area 150771.09 ± 61177.12 µm^2, average nucleic area 142.90 ± 57.27 µm^2 and proliferation index $49.09 \pm 22.67\%$. ADC_{mean} correlated with Ki 67 level ($r = -0.728$, $p = 0.011$) and total nucleic area ($r = -0.691$, $p = 0.019$) and tended to correlate with average nucleic area ($r = -0.527$, $p = 0.096$). ADC_{max} correlated with Ki 67 level ($r = -0.633$, $p = 0.036$). SUV_{max} also tended to correlate with average nucleic area ($r = 0.573$, $p = 0.066$). Combined parameter SUV_{max}/ADC_{min} correlated with average nucleic area ($r = 0.627$, $p = 0.039$).
Conclusion: ADC and SUV values showed significant correlations with different histopathological parameters and can be used as biological markers in HNSCC.

© 2016 Elsevier Ltd. All rights reserved.

Introduction

Nowadays, magnetic resonance imaging (MRI) and 18F-fluorodesoxyglucose positron emission tomography/computed tomography (18F-FDG-PET/CT) are integrated in the work-up of head and neck cancer patients [1–3]. Regarding the use of PET/MRI in these patients there are discrepant findings reported in literature. Partovi et al. [1] reported that 18F-FDG-PET/MRI and

18F-FDG-PET/CT provide comparable results in the detection of primary tumor, lymph node and distant metastases. Other authors found similar results [2,3]. However, Loffelbein et al. found that PET/MRI showed some advantages in comparison to PET/CT in the head and neck region [4]. They recently published a retrospective study comparing the diagnostic accuracy of retrospective PET–MRI fusion with MRI alone and 18F-FDG PET/CT. The authors suggested that for morphologic imaging multimodal PET/MRI is beneficial because of the superior soft tissue contrast and fewer artifacts from dental implants [4]. In addition, MRI allows functional imaging, such as the assessment of perfusion with dynamic contrast-enhanced MRI [4]. Furthermore, MRI can be

* Corresponding author.
E-mail addresses: alex.surow@medizin.uni-halle.de, Alexey.Surov@medizin.uni-leipzig.de (A. Surov).

completed by diffusion weighted imaging (DWI), which provides additional information regarding tumor texture [5–7]. For example in HNSCC, DWI correlated with cell density [7]. However, according to Queiroz et al. the use of DWI as part of PET/MRI to evaluate head and neck cancers does not provide diagnostically relevant information [8]. The authors also stated that the use of DWI might not be needed in clinical PET/MRI protocols for the staging or restaging of head and neck cancers [8].

Similarly, Grueneisen et al. reported that DWI in PET/MR imaging has no diagnostic benefit for whole-body staging of women with pelvic malignancies [9].

Varoquaux et al. [10] mentioned that HNSCC causes a decreased apparent diffusion coefficient (ADC) on DWI and an increased standardized uptake value (SUV) on ^{18}F-FDG-PET/CT, so ADC and SUV may be used as independent biomarkers in HNSCC. Furthermore, a statistical not significant trend towards higher SUV and lower ADC was observed with increasing tumor dedifferentiation [10]. In addition, Nakajo et al. reported a significant inverse correlation of pretreatment primary tumor ADC and SUV with a similar potential to predict disease free survival of patients with HNSCC [11]. Baba et al. [12] investigated breast tumors and indicated that SUV and ADC were helpful parameters in differentiating benign from malignant breast tumors. The authors observed significant differences in ADC and SUV between benign and malignant breast tumors [12]. Moreover, a new parameter SUV/ADC was introduced by the authors [12]. Using SUV/ADC produced better results than SUV or ADC alone in differentiating benign from malignant tumors [12]. In addition, high SUV was found to correlate with larger tumor size, higher nuclear grade, and the triple-negative hormonal receptor profile [12]. High ADC was revealed to be correlated with negative progesterone receptor and positive human epidermal growth factor receptor 2 profiles [12].

These controversial findings regarding the role of glucose metabolism and DWI in tumor diagnosis and characterization may be related to the fact that both parameters may be associated with different tumor tissue features.

The purpose of this study was to analyze possible associations between functional parameters derived from simultaneous ^{18}F-FDG-PET/MRI and histopathological parameters in patients with HNSCC.

Material and methods

This prospective study was approved by the institutional review board.

Patients

11 patients with primary HNSCC were included into the study. There were 2 women and 9 men with a median age of 56 years mean age 56.0 ± 5.5 years, range 49–66 years (Table 1). In all cases the diagnosis was confirmed by histopathology.

Table 1
Clinical data of the investigated patients.

Case	Age	Sex	T stage	N stage	M stage
1	54	m	3	2b	0
2	57	m	2	2b	0
3	50	m	4	3	0
4	56	m	3	1	1
5	61	m	3	3	0
6	66	f	3	2b	0
7	49	m	4a	2c	0
8	50	m	4b	2b	1
9	57	f	4a	2c	0
10	54	m	3	2c	0
11	63	m	3	3	0

PET/MRI acquisition

All 11 patients underwent an ^{18}F-FDG-PET/CT protocol on a Siemens Biograph 16 PET/CT scanner and a simultaneous whole-body PET/MR after a fasting period of at least 6 h. Detailed descriptions of the technical aspects were reported in previous publications [3,13]. In 14 of 16 patients PET/CT was performed first and then PET/MRI, in two patients PET/MRI was performed prior to PET/CT due to logistic reasons. Administration of ^{18}F-FDG was performed once for both studies, depending on body weight (5 MBq/kg, range 205–396 MBq). Postinjection median uptake time was 84 min (range 60–120 min) for the first imaging study and 194 min (range 150–260 min) for the second imaging study. For attenuation correction a coronal 3D-encoded gradient-echo sequence (Dixon-VIBE) was used.

In addition to a whole-body examination the neck region was investigated by using a combined head-and-neck coil. Additional axial T1-weighted turbo spin echo (TSE), T2-weighted TSE sequences with fat suppression and coronal T2-weighted TIRM sequences were performed. DWI was obtained with an axial DWI-EPI sequence (TR/TE 8620/73 ms, slice thickness 4 mm, voxel size $3.2 \times 2.6 \times 4.0$ mm, b-values of 0 and 800 s/mm^2).

Furthermore axial and coronal fat saturated T1-weighted TSE sequences and an axial contrast enhanced T1-weighted VIBE sequence were conducted after intravenous application of contrast medium (Gadovist®, Bayer Healthcare, Leverkusen, Germany), 0.1 mmol per kg of bodyweight.

Image analysis

PET data sets were reviewed on a commercially available workstation (Syngo.Via, Siemens Healthcare, Erlangen, Germany) by one radiologist (MG) and one board certified nuclear medicine physician (SP) with 4 and 7 years of experience in head and neck CT, MR and PET/CT imaging, respectively. For all tumors, mean and maximum SUV were analyzed in the PET dataset of the neck with the nuclear medicine physician plotting an isocontour volume of interest (VOI) around the tumor (SUV$_{max}$ threshold 40%).

ADC maps were automatically generated by the implemented software. Regions of interest (ROI) were manually drawn on the ADC maps along the contours of the tumor on each slice in cognitive fusion with the complete MRI and PET datasets as reported previously [14].

In all lesions minimal ADC values (ADC$_{min}$), mean ADC values (ADC$_{mean}$), and maximal ADC values (ADC$_{max}$) were estimated (Figs. 1–3).

Furthermore, combined parameters SUV$_{max}$ divided by ADC$_{min}$ (SUV$_{max}$/ADC$_{min}$) and SUV$_{max}$ divided by ADC$_{mean}$ (SUV$_{max}$/ADC$_{min}$) were calculated.

Histopathological analysis

In all cases the diagnosis was confirmed by biopsy. The available pathological specimens were re-analyzed for the current study.

The tumor proliferation index was estimated on Ki 67 antigen stained specimens by using MIB-1 monoclonal antibody (DakoCytomation, Denmark) as reported previously [15,16]. The area with the highest number of positive tumor nuclei was selected for the analysis.

Furthermore, the Ki 67 antigen stained samples were digitalized by using a research microscope Jenalumar (Zeiss, Jena, Germany), with camera Diagnostic instruments 4.2., magnification 400×.

The digital color images (uncompressed TIFF) were analyzed by using ImageJ software 1.48v (National Institutes of Health Image program) with a Windows operating system [14,15]. All images
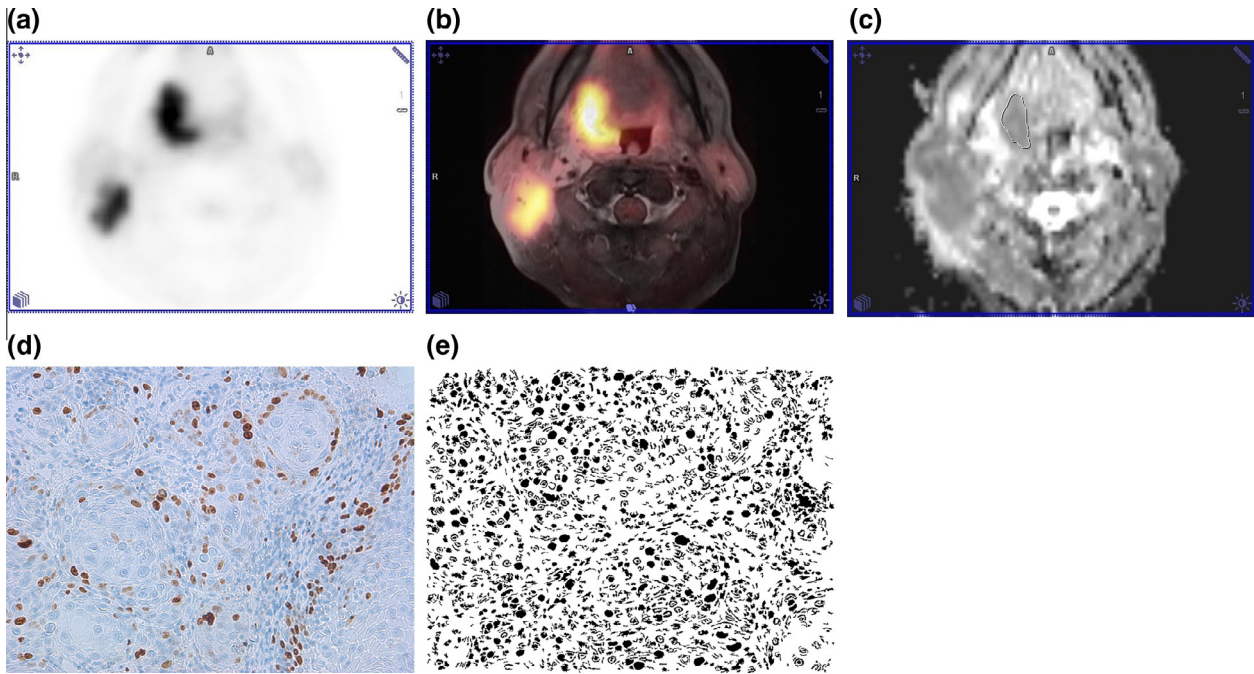
Fig. 1. Simultaneous ^{18}F-FDG-PET/MRI and histopathological findings in a patient with diagnosed squamous cell carcinoma. ^{18}F-FDG-PET imaging (a) and fused ^{18}F-FDG-PET/T1 weighted TSE MR image (b) documenting a large lesion at the right side. $SUV_{max} = 26.62$, $SUV_{mean} = 15.46$. Additionally, large right sided lymph node swelling is also seen. (c) ADC map. The ADC values ($\times 10^{-3}$ mm^2 s^{-1}) of the primary lesion are as follows: $ADC_{min} = 0.67$, $ADC_{mean} = 1.31$, and $ADC_{max} = 2.59$. (d) Immunohistochemical stain (MIB-1 monoclonal antibody). Ki 67 index = 30% and cell count = 1018. (e) "Particles tool" analysis image. The total nucleic area is 130398.75 μm^2, the average nucleic area is 128.47 μm^2.
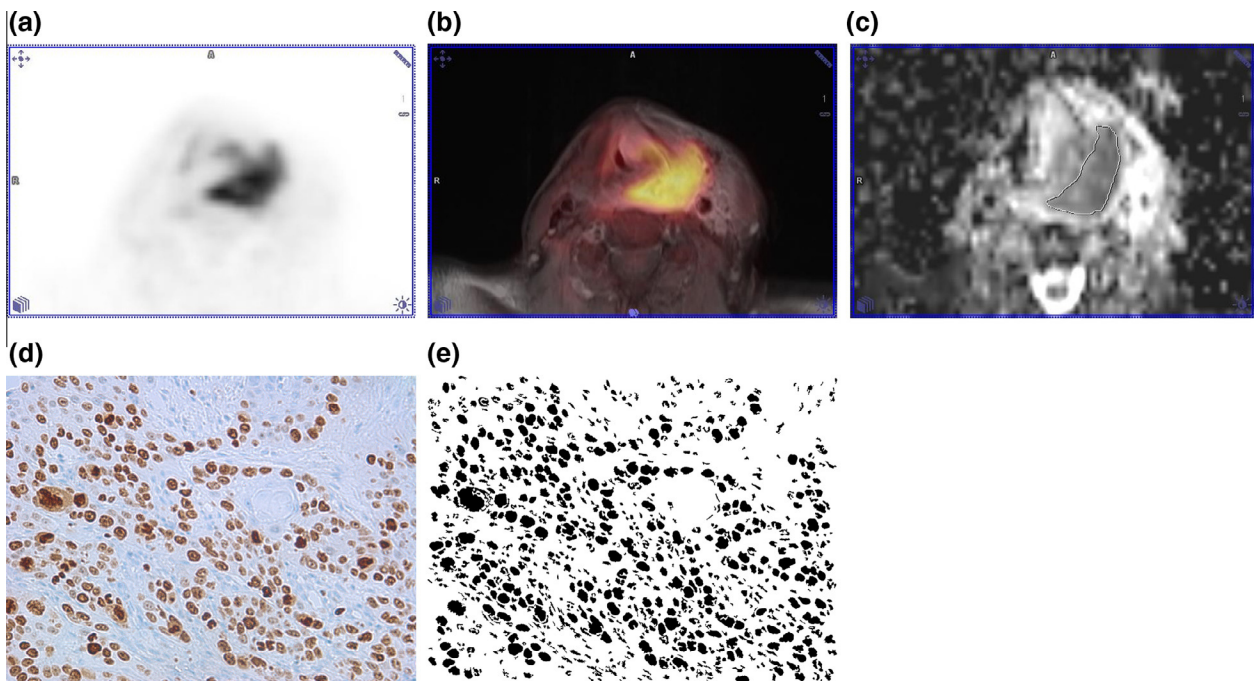
Fig. 2. Imaging and histopathological findings in pharyngeal squamous cell carcinoma. ^{18}F-FDG-PET imaging (a) and fused ^{18}F-FDG-PET/T1 weighted TSE MR image (b) showing a large left sided pharyngeal lesion. $SUV_{max} = 22.97$, $SUV_{mean} = 12.77$. (c) ADC map of the tumor. $ADC_{min} = 0.34 \times 10^{-3}$ mm^2 s^{-1}, $ADC_{mean} = 1.21 \times 10^{-3}$ mm^2 s^{-1}, and $ADC_{max} = 1.94 \times 10^{-3}$ mm^2 s^{-1}. (d) Immunohistochemical stain (MIB-1 monoclonal antibody). Ki 67 index = 75% and cell count = 943. (e) "Particles tool" analysis image. Total nucleic area = 172051.82 μm^2, average nucleic area = 180.34 μm^2.

were converted to a black and white binary image by setting the image threshold as reported previously [17,18]. The threshold selected image parts were further analyzed using the Analyze Particles tool. Nucleic count (cell count), total nucleic area, and average nuclei area were estimated in every case.

Statistical analysis

Statistical analysis and graphics creation was performed using GraphPad Prism (GraphPad Software, La Jolla, CA, USA). All measurements were normally distributed according to
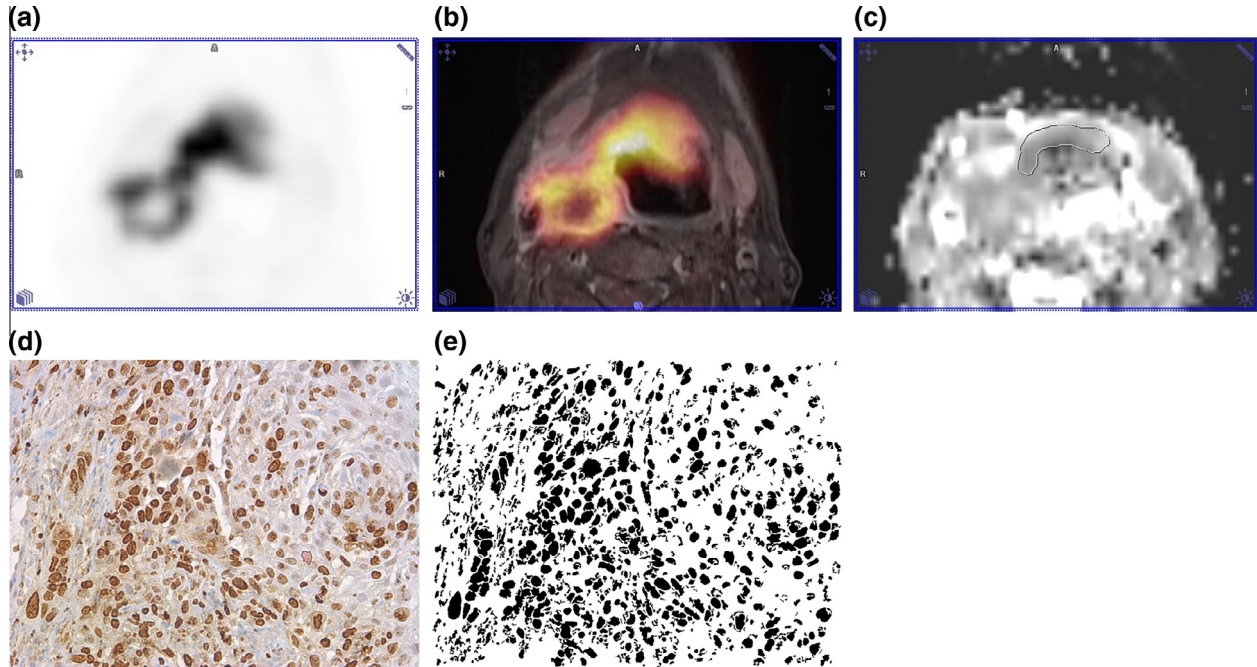
Fig. 3. (a) ^{18}F-FDG-PET imaging documenting a right sided lesion with an intensive tracer accumulation: SUV_{max} = 31.76, SUV_{mean} = 19.85. Additionally, large cervical lymph node metastases are seen. (b) Fused image of simultaneously acquired ^{18}F-FDG-PET and T1 weighted TSE MR images. (c) ADC map. The ADC values ($\times 10^{-3}$ mm^2 s^{-1}) of the primary tumor are as follows: ADC_{min} = 0.55, ADC_{mean} = 1.16, and ADC_{max} = 1.97. (d) Histopathological investigation after biopsy confirmed the diagnosis of squamous cell carcinoma. Immunohistochemical stain (MIB-1 monoclonal antibody). Ki 67 index = 80%, cell count = 789. (e) "Particles tool" analysis image. The total nucleic area is 202356.0 µm^2, the average nucleic area is 256.92 µm^2.

Table 2
Estimated parameters of HNSCC.

Parameters	M ± SD	Median	Range
SUVmax	24.41 ± 6.51	26.62	11.14–31.76
SUVmean	15.01 ± 4.07	15.46	6.780–19.85
ADC_{min}, $\times 10^{-3}$ mm^2 s^{-1}	0.65 ± 0.20	0.58	0.34–1.01
ADC_{mean}, $\times 10^{-3}$ mm^2 s^{-1}	1.28 ± 0.18	1.23	1.08–1.72
ADC_{max}, $\times 10^{-3}$ mm^2 s^{-1}	2.16 ± 0.35	1.99	1.82–3.01
SUV_{max}/ADC_{min}	41.57 ± 16.79	39.73	12.95–67.56
SUV_{max}/ADC_{mean}	19.47 ± 6.23	20.32	8.7–27.38
Cell count	1069.82 ± 388.66	1018	313–1657
Ki 67, %	49.09 ± 22.67	45	20–80
Total nucleic area, µm^2	150771.09 ± 61177.12	144510.33	21,227–252,128
Average nucleic area, µm^2	142.90 ± 57.27	155.16	66.71–256.92

Kolmogorov–Smirnov-test. Collected data were evaluated by means of descriptive statistics (absolute and relative frequencies). Pearson's correlation coefficient was used to analyze the association between ADC/SUV values and histological parameters. P-values <0.05 were taken to indicate statistical significance in all instances.

Table 3
Correlations between ADC and SUV parameters.

Parameters	SUV_{max}	SUV_{mean}
ADC_{mean}	$r = -0.318$ $p = 0.340$	$r = -0.255$ $p = 0.450$
ADC_{min}	$r = -0.155$ $p = 0.650$	$r = -0.027$ $p = 0.937$
ADC_{max}	$r = -0.264$ $p = 0.433$	$r = -0.281$ $p = 0.519$

Results

For all tumors the mean SUV_{max} was 24.41 ± 6.51, the mean SUV_{mean} was 15.01 ± 4.07 (Figs. 1–3).

Mean values of ADC parameters were as follows: ADC_{min}: 0.65 ± 0.20 $\times 10^{-3}$ mm^2 s^{-1}; ADC_{mean}: 1.28 ± 0.18 $\times 10^{-3}$ mm^2 s^{-1}; and ADC_{max}: 2.16 ± 0.35 $\times 10^{-3}$ mm^2 s^{-1} (Figs. 1–3). The mean values of the calculated combined parameters SUV_{max}/ADC_{min} and SUV_{max}/ADC_{mean} were 41.57 ± 16.79 and 19.47 ± 6.23, respectively.

Histopathological analysis identified the following results: mean cell count was 1069.82 ± 388.66, mean total nucleic area was 150771.09 ± 61177.12 µm^2 and mean average nucleic area was 142.90 ± 57.27 µm^2. The mean level of the proliferation index

was 49.09 ± 22.67%. A complete overview of the results including median values and ranges is given in Table 2.

There was no significant correlation between different ADC parameters and SUV_{max} or SUV_{mean} (Table 3). Furthermore, we correlated the estimated histopathological parameters with SUV and ADC values. All relevant correlation parameters are put together in Table 4.

ADC_{mean} inversely correlated with Ki 67 level ($r = -0.728$, $p = 0.011$) and total nucleic area ($r = -0.691$, $p = 0.019$) and had a tendency to correlate with average nucleic area ($r = -0.527$, $p = 0.096$) (Fig. 4).

Table 4
Identified correlations between diffusion, glucose metabolism and histopathological parameters.

Parameter	Cell count	Ki 67, %	Total nucleic area, μm^2	Average nucleic area, μm^2
SUV_{max}	$r = -0.300$	$r = 0.261$	$r = 0.391$	$r = 0.573$
	$p = 0.370$	$p = 0.438$	$p = 0.235$	$p = 0.066$
SUV_{mean}	$r = -0.364$	$r = 0.183$	$r = 0.318$	$r = 0.573$
	$p = 0.272$	$p = 0.590$	$p = 0.340$	$p = 0.066$
ADC_{mean}	$r = -0.418$	$\boldsymbol{r = -0.728}$	$\boldsymbol{r = -0.691}$	$r = -0.527$
	$p = 0.201$	$\boldsymbol{p = 0.011}$	$\boldsymbol{p = 0.019}$	$p = 0.096$
ADC_{min}	$r = 0.055$	$r = -0.416$	$r = -0.273$	$r = -0.155$
	$p = 0.873$	$p = 0.203$	$p = 0.417$	$p = 0.650$
ADC_{max}	$r = -0.496$	$\boldsymbol{r = -0.633}$	$r = -0.753$	$r = -0.549$
	$p = 0.120$	$\boldsymbol{p = 0.036}$	$p = 0.008$	$p = 0.080$
SUV_{max}/ADC_{min}	$r = -0.291$	$r = 0.503$	$r = 0.455$	$r = 0.582$
	$p = 0.385$	$p = 0.114$	$p = 0.160$	$p = 0.060$
SUV_{max}/ADC_{mean}	$r = -0.127$	$r = 0.371$	$r = 0.491$	$\boldsymbol{r = 0.627}$
	$p = 0.709$	$p = 0.262$	$p = 0.125$	$\boldsymbol{p = 0.039}$

Table 5
Comparison of imaging parameters between T3 and T4 tumor stages.

Parameters	T3 stage	T4 stage	*p* values
SUV_{max}	23.42 ± 5.17	29.21 ± 2.36	0.11
SUV_{mean}	14.49 ± 3.27	17.86 ± 1.84	0.17
ADC_{min}, $\times 10^{-3}$ mm^2 s^{-1}	0.60 ± 0.22	0.65 ± 0.18	0.76
ADC_{mean}, $\times 10^{-3}$ mm^2 s^{-1}	1.30 ± 0.24	1.25 ± 0.87	1.0
ADC_{max}, $\times 10^{-3}$ mm^2 s^{-1}	2.20 ± 0.43	2.15 ± 0.29	1.0

Also ADC_{max} inversely correlated with Ki 67 level ($r = -0.633$, $p = 0.036$) and tended to correlate with total and average nucleic areas ($r = -0.753$, $p = 0.008$ and $r = -0.549$, $p = 0.080$, respectively) (Table 4).

Furthermore, SUV_{max} and SUV_{mean} tended to correlate with average nucleic area (in both cases, $r = 0.573$, $p = 0.066$). There was no significant correlation between SUV_{max} or SUV_{mean} and cell count or Ki 67 level (Table 4).

Finally, SUV_{max}/ADC_{mean} correlated well with average nucleic area ($r = 0.627$, $p = 0.039$) and SUV_{max}/ADC_{min} had a tendency to correlate with average nucleic area ($r = 0.582$, $p = 0.060$).

There were no significant differences between the estimated parameters of diffusion and glucose metabolism in T3 and T4 tumor stages (Table 5).

Discussion

Our study identified several significant associations between SUV, ADC and histopathological parameters in HNSCC.

It is well known that malignant tumors have lower ADC values in comparison to benign lesions [5,6]. For instance, Sasaki et al.

showed in their study that sinonasal carcinomas had statistically significant lower ADC values in comparison to benign and inflammatory disorders [6]. Furthermore, some studies found that ADC-values were associated with several histological parameters, such as proliferation marker Ki 67 and cell count [7,19,20]. It has been shown that ADC correlated well with cell count/density in different epithelial malignancies, such as prostatic cancer, and renal cell carcinoma [19,20]. These relationships were also found in head and neck cancers. For example, Driessen et al. identified significant correlations between ADC and cell count, nuclear areas, and nuclear-cytoplasmic ratio in laryngeal and hypopharyngeal carcinomas [7]. However, this does not apply for all tumors. For example, no correlation between ADC and cellularity was found in cervical and mediastinal lymphoma [21].

Some authors reported for HNSCC significant associations between SUV in ^{18}F-FDG-PET and histopathological biomarkers like p53, an important gene in the regulation of apoptosis [22,23]. So Grönroos et al. [22] mentioned that SUV was higher in aggressive HNSCC with low apoptosis rate and high expressions of mutated p53 and Vascular Endothelial Growth Factor (VEGF). Yokobori et al. [23] investigated twenty-seven patients with squamous cell carcinoma and observed a significant correlation between SUV_{max} and the expression of L-type amino acid transporter 1.

In agreement with previous reports, the present study shows significant associations between different ADC parameters and Ki 67. Moreover, statistically relevant correlation between ADC_{mean} and total nucleic area was identified. In addition, our study showed that SUV_{max} and SUV_{mean} tended to correlate with average nucleic area. Furthermore, new parameters SUV_{max}/ADC_{mean} and SUV_{max}/ADC_{min} also showed associations with average nucleic areas. To
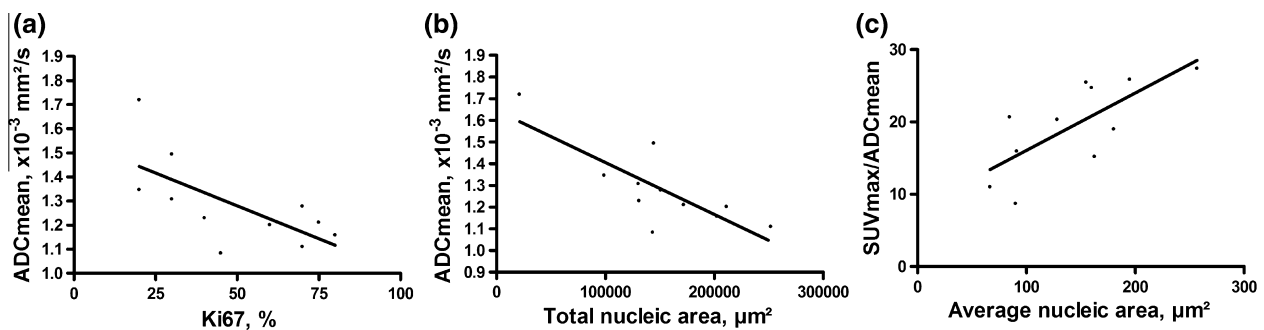
Fig. 4. Correlations between DWI, glucose metabolism and histopathological parameters. Statistical analysis documenting significant correlations between ADC_{mean} and Ki 67 level ($r = -0.728$, $p = 0.011$) (a) and ADC_{mean} and total nucleic area ($r = -0.691$, $p = 0.019$) (b). A significant correlation between SUV_{max}/ADC_{mean} and average nucleic area ($r = 0.627$, $p = 0.039$) is also shown (c).

the best of our knowledge, these results have not been reported previously. No significant correlation between SUV_{max} or SUV_{mean} and Ki 67 was found, indicating that the profliferation pathway is not strongly associated with an increased glucose metabolism. Presumably, SUV should be associated with the proliferation index. However, some previous studies also did not show any correlations between these parameters [24,25]. As mentioned in a review by Deng et al., in cancer patients ^{18}F-FDG uptake showed a moderate positive correlation with tumor cell proliferation [26]. However, different tumor types exhibited varied degrees of correlation [26]. The authors indicated that correlation between ^{18}F-FDG uptake and Ki 67 expression was extremely significant in thymic epithelial tumors, significant in gastrointestinal stromal tumors, moderate in patients with lung, breast, bone and soft tissue, pancreatic, oral, uterine and ovarian cancers, average in brain, esophageal and colorectal cancers, and poor in head and neck, thyroid, gastric tumors and malignant melanoma [26]. These findings are difficult to explain. However, they suggest that several malignancies can show different associations between glucose metabolism and ^{18}F-FDG-uptake in PET, respectively and histopathological parameters.

According to Nakajo et al. [11] DWI and ^{18}F-FDG-PET findings can show different relationships. In addition, the authors reported that SUV_{max} and ADC correlated significantly and negatively and both may have similar potential to predict disease-free survival or disease events of head and neck cancer [11]. However, other authors did not find these associations [27,28]. For example in the analysis of Choi et al., there was no significant correlation between SUV and ADC in HNSCC [27]. Similar results were also reported by Fruehwald-Pallamar et al. [28].

In the present study, also no significant correlation between different ADC parameters and SUV were identified. However, DWI and SUV values seem to reflect different histopathological features of HNSCC. Therefore, it may be postulated that ADC and SUV are independent biomarkers and complement one another. Furthermore, our study showed that new parameters SUV_{max}/ADC_{min} and SUV_{max}/ADC_{mean} can also be used to characterize histopathological features of HNSCC.

Moreover, our results may explain previous findings which suggested that tumors with high SUV values and low ADC had a more aggressive behavior and a poorer prognosis [23]. For other tumors, like breast cancer or gliomas, it has also been reported that nuclear size features were reliable prognostic indicators and lesions with large nuclei had a worse prognosis [29,30].

Some previous reports compared DWI and/or SUV values between different tumor stages in HNSCC. For example, Shi et al. found that the sum of SUVmax of primary tumor and cervical lymph nodes (total SUV_{max}) was an independently predictive factor for distant metastasis in patients of nasopharyngeal carcinoma [31]. In the present study, no significant differences in SUV and ADC values were identified between T3 and T4 tumor stages. Because of the small group of the investigated patients, no other analyses, for example between N or M stages, could be performed.

According to the literature, SUV and/or ADC values can be used as prognosis factors in patients with HNSCC. Recently, Preda et al. reported that patients with SUV_{max} tumor/background ratio $\geqslant 5.75$ had an overall worse prognosis [32]. Additionally, high ADC_{min} also significantly predicted a worse prognosis, with adjusted hazard ratio = 3.11 [32]. Furthermore, Ng et al. identified $SUV_{max} > 19.44$ as independent risk factor for progression-free survival and overall survival rates [33].

Presumably, the possibility to use of the reported imaging findings as prediction factors may be due to associations of them with histological features of neck cancer. In fact, our study detected several significant correlations between SUV, ADC and histopathological parameters can explain the results of previous investigations.

It has been reported that PET/MRI co-registration might become a useful tool in the planning of image-based surgery and radiotherapy, image-guided radiotherapy, and the determination of the level of follow-up in the treatment of the various cancer types [34]. For instance, Covello et al. showed the feasibility of PET/MR imaging for primary tumors and recurrent tumors evaluations of head/neck malignant lesions [35]. The authors suggested that PET/MR can better characterize HNSCC [35]. Other authors also mentioned that MR imaging and 18F-FDG PET/CT imaging are complementary to each other in the assessment of HNSCC at different stages of the disease [36]. The present analysis provides new information regarding associations between diffusion, glucose metabolism and histopathological parameters in HNSCC and, therefore, emphasizes the potential of PET/MRI in evaluation of neck cancer.

Our study has several limitations. First, results are based on a small number of patients. Second, it focussed on the search of possible associations between ADC, SUV and histomorphological features in HNSCC. Associations with other functional tumor parameters, such as cell cycle regulator and/or apoptosis factors were not analyzed. Additionally, further analyses with more specific PET tracers for imaging hypoxia like ^{18}F-fluoromisonidazole (^{18}F-FMISO), ^{18}F-fluoroazomycin-arabinoside (^{18}F-FAZA) or for imaging proliferation like ^{18}F-fluorothymidine (^{18}F-FLT) could be performed to gain further insight into the molecular pathways underlying tracer uptake and further possible associations of functional parameters in HNSCC.

Clearly, further investigations with more patients are needed to study possible associations between PET/MRI findings and tumor behavior.

In conclusion, the present study identified different associations between ^{18}F-FDG-PET and DWI findings and histopathological parameters in HNSCC. ADC_{mean} showed statistically significant inverse correlations with Ki 67, and total nucleic area of tumors. SUV_{max} tended to correlate with average nucleic area. A new parameter SUV_{max}/ADC_{mean} also correlated well with average nucleic areas.

Therefore, ADC and SUV values can be used as complementary biological markers in HNSCC. In the future, ^{18}F-FDG-PET/MRI might help in non-invasive characterization of tumors and allow a prognostic stratification.

Conflict of interest statement

The author O. Sabri received travel expenses from Siemens Healthcare related to lectures on PET/MRI, grants, travel expenses, speaker honoraria and payment for consultancy for Bayer Healthcare and Piramal Imaging. Apart from this all other authors declare no conflict of interest.

Acknowledgement

References

[1] Partovi S, Kohan A, Vercher-Conejero JL, Rubbert C, Margevicius S, Schluchter MD, et al. Qualitative and quantitative performance of ^{18}F-FDG-PET/MRI versus ^{18}F-FDG-PET/CT in patients with head and neck cancer. Am J Neuroradiol 2014;35:1970–5.

[2] Varoquaux A, Rager O, Poncet A, Delattre BM, Ratib O, Becker CD, et al. Detection and quantification of focal uptake in head and neck tumours: ^{18}F-FDG PET/MR versus PET/CT. Eur J Nucl Med Mol Imaging 2014;41:462–75.

[3] Kubiessa K, Purz S, Gawlitza M, Kühn A, Fuchs J, Steinhoff KG, et al. Initial clinical results of simultaneous ^{18}F-FDG PET/MRI in comparison to ^{18}F-FDG PET/CT in patients with head and neck cancer. Eur J Nucl Med Mol Imaging 2014;41:639–48.

[4] Loeffelbein DJ, Souvatzoglou M, Wankerl V, Dinges J, Ritschl LM, Mücke T, et al. Diagnostic value of retrospective PET–MRI fusion in head-and-neck cancer. BMC Cancer 2014;14:846.

[5] Wang J, Takashima S, Takayama F, Kawakami S, Saito A, Matsushita T, et al. Head and neck lesions: characterization with diffusion-weighted echo-planar MR imaging. Radiology 2001;220:621–30.

[6] Sasaki M, Eida S, Sumi M, Nakamura T. Apparent diffusion coefficient for sinonasal diseases: differentiation of benign and malignant lesions. Am J Neuroradiol 2011;32:1256–62.

[7] Driessen JP, Caldas-Magalhaes J, Janssen LM, Pameijer FA, Kooij N, Terhaard CH, et al. Diffusion-weighted MR Imaging in Laryngeal and Hypopharyngeal Carcinoma: association between apparent diffusion coefficient and histologic findings. Radiology 2014;272:456–63.

[8] Queiroz MA, Hüllner M, Kuhn F, Huber G, Meerwein C, Kollias S, et al. Use of diffusion-weighted imaging (DWI) in PET/MRI for head and neck cancer evaluation. Eur J Nucl Med Mol Imaging 2014;41:2212–21.

[9] Grueneisen J, Schaarschmidt BM, Beiderwellen K, Schulze-Hagen A, Heubner M, Kinner S, et al. Diagnostic value of diffusion-weighted imaging in simultaneous ^{18}F-FDG PET/MR imaging for whole-body staging of women with pelvic malignancies. J Nucl Med 2014;55:1930–5.

[10] Varoquaux A, Rager O, Lovblad KO, Masterson K, Dulguerov P, Ratib O, et al. Functional imaging of head and neck squamous cell carcinoma with diffusion-weighted MRI and FDG PET/CT: quantitative analysis of ADC and SUV. Eur J Nucl Med Mol Imaging 2013;40:842–52.

[11] Nakajo M, Nakajo M, Kajiya Y, Tani A, Kamiyama T, Yonekura R, et al. FDG PET/CT and diffusion-weighted imaging of head and neck squamous cell carcinoma: comparison of prognostic significance between primary tumor standardized uptake value and apparent diffusion coefficient. Clin Nucl Med 2012;37:475–80.

[12] Baba S, Isoda T, Maruoka Y, Kitamura Y, Sasaki M, Yoshida T, et al. Diagnostic and prognostic value of pretreatment SUV in ^{18}F-FDG/PET in breast cancer: comparison with apparent diffusion coefficient from diffusion-weighted MR imaging. J Nucl Med 2014;55:736–42.

[13] Sattler B, Jochimsen T, Barthel H, Sommerfeld K, Stumpp P, Hoffmann KT, et al. Physical and organizational provision for installation, regulatory requirements and implementation of a simultaneous hybrid PET/MR-imaging system in an integrated research and clinical setting. Magma 2013;26:159–71.

[14] Gawlitza M, Purz S, Kubiessa K, Boehm A, Barthel H, Kluge R, et al. In vivo correlation of glucose metabolism, cell density and microcirculatory parameters in patients with head and neck cancer: initial results using simultaneous PET/MRI. PLoS ONE 2015;10:e0134749.

[15] Roser F, Samii M, Ostertag H, Bellinzona M. The Ki-67 proliferation antigen in meningiomas. Experience in 600 cases. Acta Neurochir (Wien) 2004;146:37–44.

[16] Yue Q, Shibata Y, Isobe T, Anno I, Kawamura H, Gong QY, et al. Absolute choline concentration measured by quantitative proton MR spectroscopy correlates with cell density in meningioma. Neuroradiology 2009;51:61–7.

[17] Aoyagi T, Shuto K, Okazumi S, Hayano K, Satoh A, Saitoh H, et al. Apparent diffusion coefficient correlation with oesophageal tumour stroma and angiogenesis. Eur Radiol 2012;22:1172–7.

[18] Guo AC, Cummings TJ, Dash RC, Provenzale JM. Lymphomas and high-grade astrocytomas: comparison of water diffusibility and histologic characteristics. Radiology 2002;224:177–83.

[19] Gibbs P, Liney GP, Pickles MD, Zelhof B, Rodrigues G, Turnbull LW. Correlation of ADC and T2 measurements with cell density in prostate cancer at 3.0 Tesla. Invest Radiol 2009;44:572–6.

[20] Goyal A, Sharma R, Bhalla AS, Gamanagatti S, Seth A, Iyer VK, et al. Diffusion-weighted MRI in renal cell carcinoma: a surrogate marker for predicting nuclear grade and histological subtype. Acta Radiol 2012;53:349–58.

[21] Wu X, Pertovaara H, Dastidar P, Vornanen M, Paavolainen L, Marjomäki V, et al. ADC measurements in diffuse large B-cell lymphoma and follicular lymphoma: a DWI and cellularity study. Eur J Radiol 2013;82:e158–64.

[22] Grönroos TJ, Lehtiö K, Söderström KO, Kronqvist P, Laine J, Eskola O, et al. Hypoxia, blood flow and metabolism in squamous-cell carcinoma of the head and neck: correlations between multiple immunohistochemical parameters and PET. BMC Cancer 2014;14:876.

[23] Yokobori Y, Toyoda M, Sakakura K, Kaira K, Tsushima Y, Chikamatsu K. ^{18}F-FDG uptake on PET correlates with biological potential in early oral squamous cell carcinoma. Acta Otolaryngol 2015;135:494–9.

[24] Linecker A, Kermer C, Sulzbacher I, Angelberger P, Kletter K, Dudczak R, et al. Uptake of ^{18}F-FLT and ^{18}F-FDG in primary head and neck cancer correlates with survival. Nuklearmedizin 2008;47:80–5.

[25] Kaida H, Kawahara A, Hayakawa M, Hattori S, Kurata S, Fujimoto K, et al. The difference in relationship between ^{18}F-FDG uptake and clinicopathological factors on thyroid, esophageal, and lung cancers. Nucl Med Commun 2014;35:36–43.

[26] Deng SM, Zhang W, Zhang B, Chen YY, Li JH, Wu YW. Correlation between the uptake of ^{18}F-Fluorodeoxyglucose (^{18}F-FDG) and the expression of proliferation-associated Antigen Ki-67 in cancer patients: a meta-analysis. PLoS ONE 2015;10:e0129028.

[27] Choi SH, Paeng JC, Sohn CH, Pagsisihan JR, Kim YJ, Kim KG, et al. Correlation of ^{18}F-FDG uptake with apparent diffusion coefficient ratio measured on standard and high b value diffusion MRI in head and neck cancer. J Nucl Med 2011;52:1056–62.

[28] Fruehwald-Pallamar J, Czerny C, Mayerhoefer ME, Halpern BS, Eder-Czembirek C, Brunner M, et al. Functional imaging in head and neck squamous cell carcinoma: correlation of PET/CT and diffusion-weighted imaging at 3 Tesla. Eur J Nucl Med Mol Imaging 2011;38:1009–19.

[29] Abdalla F, Boder J, Markus R, Hashmi H, Buhmeida A, Collan Y. Correlation of nuclear morphometry of breast cancer in histological sections with clinicopathological features and prognosis. Anticancer Res 2009;29:1771–6.

[30] Boruah D, Deb P, Srinivas V, Mani NS. Morphometric study of nuclei and microvessels in gliomas and its correlation with grades. Microvasc Res 2014;93:52–61.

[31] Shi Q, Yang Z, Zhang Y, Hu C. Adding maximum standard uptake value of primary lesion and lymph nodes in ^{18}F-Fluorodeoxyglucose PET helps predict distant metastasis in patients with nasopharyngeal carcinoma. PLoS ONE 2014;9:e103153.

[32] Preda L, Conte G, Bonello L, Giannitto C, Travaini LL, Raimondi S, et al. Combining standardized uptake value of FDG-PET and apparent diffusion coefficient of DW-MRI improves risk stratification in head and neck squamous cell carcinoma. Eur Radiol 2016. http://dx.doi.org/10.1007/s00330-016-4284-8.

[33] Ng SH, Liao CT, Lin CY, Chan SC, Lin YC, Yen TC, et al. Dynamic contrast-enhanced MRI, diffusion-weighted MRI and ^{18}F-FDG PET/CT for the prediction of survival in oropharyngeal or hypopharyngeal squamous cell carcinoma treated with chemoradiation. Eur Radiol 2016. http://dx.doi.org/10.1007/s00330-016-4276-8.

[34] Loeffelbein DJ, Souvatzoglou M, Wankerl V, Martinez-Möller A, Dinges J, Schwaiger M. PET–MRI fusion in head-and-neck oncology: current status and implications for hybrid PET/MRI. J Oral Maxillofac Surg 2012;70:473–83.

[35] Covello M, Cavalierea C, Aielloa M, Cianellia MS, Mesolellab M, Ioriob B, et al. Simultaneous PET/MR head–neck cancer imaging: preliminary clinical experience and multiparametric evaluation. Eur J Radiol 2015;84:1269–76.

[36] Lai V, Khong PL. Updates on MR imaging and ^{18}F-FDG PET/CT imaging in nasopharyngeal Carcinoma. Oral Oncol 2014;50:539–48.

3. Ausblick mit Übersichtsartikel
„Molekulare Bildgebung bei Kopf-Hals-Tumoren"

Das Feld der Hybriddiagnostik mit PET/MRT wurde gerade erst betreten und es bleiben noch sehr viele Fragen offen. Bereits nach den ersten Jahren wird jedoch deutlich, dass die PET/MRT nicht einfach die „bessere" PET/CT ist. Alle bisherigen Untersuchungen, die einen direkten Vergleich der diagnostischen Genauigkeit vornahmen, konnten bei den hierfür klassischerweise herangezogenen Parametern (Sensitivität, Spezifität, positiver und negativer Prädiktivwert) lediglich eine Vergleichbarkeit der Methoden konstatieren, jedoch keine Vorteile der PET/MRT [142]. Stattdessen rücken immer mehr die Fragestellungen in den Fokus, die nur mit einer multiparametrischen Bildgebung wie der PET/MRT beantwortet werden können. Hierunter fallen Fragen wie: Gibt es funktionelle Bildgebungsparameter, die miteinander korrelieren? Oder sind die Daten komplementär in ihrer Aussagekraft zur Charakterisierung des (Tumor-)Gewebes? Können die Parameter aus der Bildgebung das histopathologische Bild des Tumors vorhersagen? Können Sie Ergebnisse liefern zur Charakterisierung des biologischen Verhaltens des Tumors? Können Sie Therapieerfolge vorhersagen?

Eine Übersichtsarbeit zum aktuellen Stand der molekularen Bildgebung bei Kopf-Hals-Tumoren mit einem entsprechenden Blick auf die Perspektiven wird an dieser Stelle als letzter Teil der Habilitationsschrift eingefügt [143].

CrossMark

P. Stumpp[1] · S. Purz[2] · O. Sabri[2] · T. Kahn[1]

[1] Klinik und Poliklinik für Diagnostische und Interventionelle Radiologie, Universitätsklinikum Leipzig AöR, Leipzig, Deutschland

[2] Klinik und Poliklinik für Nuklearmedizin, Universitätsklinikum Leipzig, Leipzig, Deutschland

Molekulare Bildgebung bei Kopf-Hals-Tumoren

Perspektive der PET-MRT

Schon während der Entwicklung der ersten Positronenemissionstomographie-Magnetresonanztomographie-Systeme (PET-MRT) wurden Hoffnungen geäußert, dass diese neue Bildgebungsmodalität Fortschritte auf dem Gebiet der Tumordiagnostik bringen könnte. Häufig wurde dabei insbesondere der Bereich der Kopf-Hals-Tumoren benannt. Hier weist die bisher etablierte Diagnostik mit Computertomographie (CT), MRT und PET-CT aufgrund der komplexen Anatomie, verschiedener Artefakte und der Lagerungsvariabilität noch Einschränkungen auf. Dieser Artikel fasst die bisherigen Ergebnisse der PET-MRT-Diagnostik bei Kopf-Hals-Tumoren zusammen und gibt einen Ausblick auf kommende Entwicklungen.

Hintergrund

Tumoren der Kopf-Hals-Region rangieren an sechster Stelle der Häufigkeit von Tumorerkrankungen und gehen im Allgemeinen mit einer relativ schlechten Prognose einher [1]. Die Überlebenswahrscheinlichkeit sinkt deutlich bei fortgeschrittenen Tumorstadien und vorhandenen Lymphknotenmetastasen. Laut dem amerikanischen Cancer Report aus dem Jahr 2008 fällt die 5-Jahres-Überlebensrate von 82 % bei einem lokalen Tumorwachstum auf 52 % bei nachgewiesenen Lymphknotenmetastasen und auf 27 % bei Fernmetastasen [2]. Die Detektion des Primärtumors beruht vorwiegend auf der klinischen Untersuchung, die Bildgebung ist jedoch

essenziell für das Tumorstaging. Während Tumoren niedriger Stadien häufig nur operativ behandelt oder bestrahlt werden, ist bei höheren Stadien eine simultane Radiochemotherapie oder eine Kombination aus Operation und adjuvanter Radio(chemo)therapie indiziert [3]. In der Nachsorge der therapierten Patienten hat die Bildgebung einen hohen Stellenwert zur Detektion lokoregionärer Rezidive und hämatogener Metastasen.

Mit den inzwischen verfügbaren sequenziellen oder simultanen PET-MRT-Systemen ist eine neue Bildgebungsmodalität vorhanden, deren zusätzlicher Nutzen in diesem Artikel speziell beleuchtet wird. Vor der Einführung von Ganzkörper-PET-MRT-Systemen wurde im Jahr 2006 ein PET-Insert vorgestellt, das innerhalb eines 3-T-MRT positioniert werden konnte und eine kombinierte, simultane PET-MRT-Diagnostik des Gehirns und der oberen Halsregion erlaubte [4]. Boss et al. [5] beschrieben die Machbarkeit einer kombinierten PET-MRT-Untersuchung mit diesem System bei Tumoren im oberen Halsbereich. Da aber die anatomische Abdeckung der PET mit diesem Insert lediglich bis zum zervikalen Lymphknotenlevel II reichte, war eine Untersuchung von Patienten mit Hypopharynx- und Larynxtumoren nicht möglich. Auch eine lokoregionäre oder gar systemische Beurteilung der Tumorausbreitung konnte damit nicht vorgenommen werden, dies war erst mit Einführung kombinierter Systeme im Jahr 2010 möglich.

Diagnostische Genauigkeit von CT, MRT und PET-CT bei Kopf-Hals-Tumoren

Die ersten Studien zur PET-MRT bei Kopf-Hals-Tumoren widmeten sich vorrangig dem Vergleich der diagnostischen Genauigkeit gegenüber bisherigen Standards. Daher wird hier zunächst eine Übersicht bzgl. der Genauigkeit der bisherigen Modalitäten gegeben.

In einer aktuellen Metaanalyse fassen *Sarrión Pérez et al.* [6] zusammen, dass CT und MRT schon seit Jahren verlässliche Instrumente zum lokalen Staging von Tumoren der Mundhöhle sind mit Vorteilen der MRT aufgrund des höheren Weichgewebskontrasts bei Knochenmarkinfiltration, perineuraler Tumorausbreitung und kleinen Tumoren. Auch die geringere Anfälligkeit gegenüber Zahnfüllungsartefakten ist von Vorteil bei der Detektion von Primärtumoren. Die PET kann in Einzelfällen bei der Detektion hilfreich sein, ist jedoch für eine Bestimmung des T-Stadiums aufgrund der schlechteren Ortsauflösung zu ungenau.

Bezüglich des N-Stagings zitieren die Autoren verschiedene Studien, in denen CT und MRT vergleichbare Ergebnisse erzielen, allerdings mit einer erheblichen Schwankungsbreite in der Sensitivität, die für die CT von 23,8–79 % reicht und für die MRT von 31,4–88,5 %. Der zusätzliche Nutzen der alleinigen PET mit [18]Fluor-Fluordesoxyglukose (^{18}F-FDG) als Radiotracer wird heterogen beurteilt mit mehreren Publikationen, die eine höhere Genauigkeit der Modalität belegen und solchen, in denen die Ergebnisse
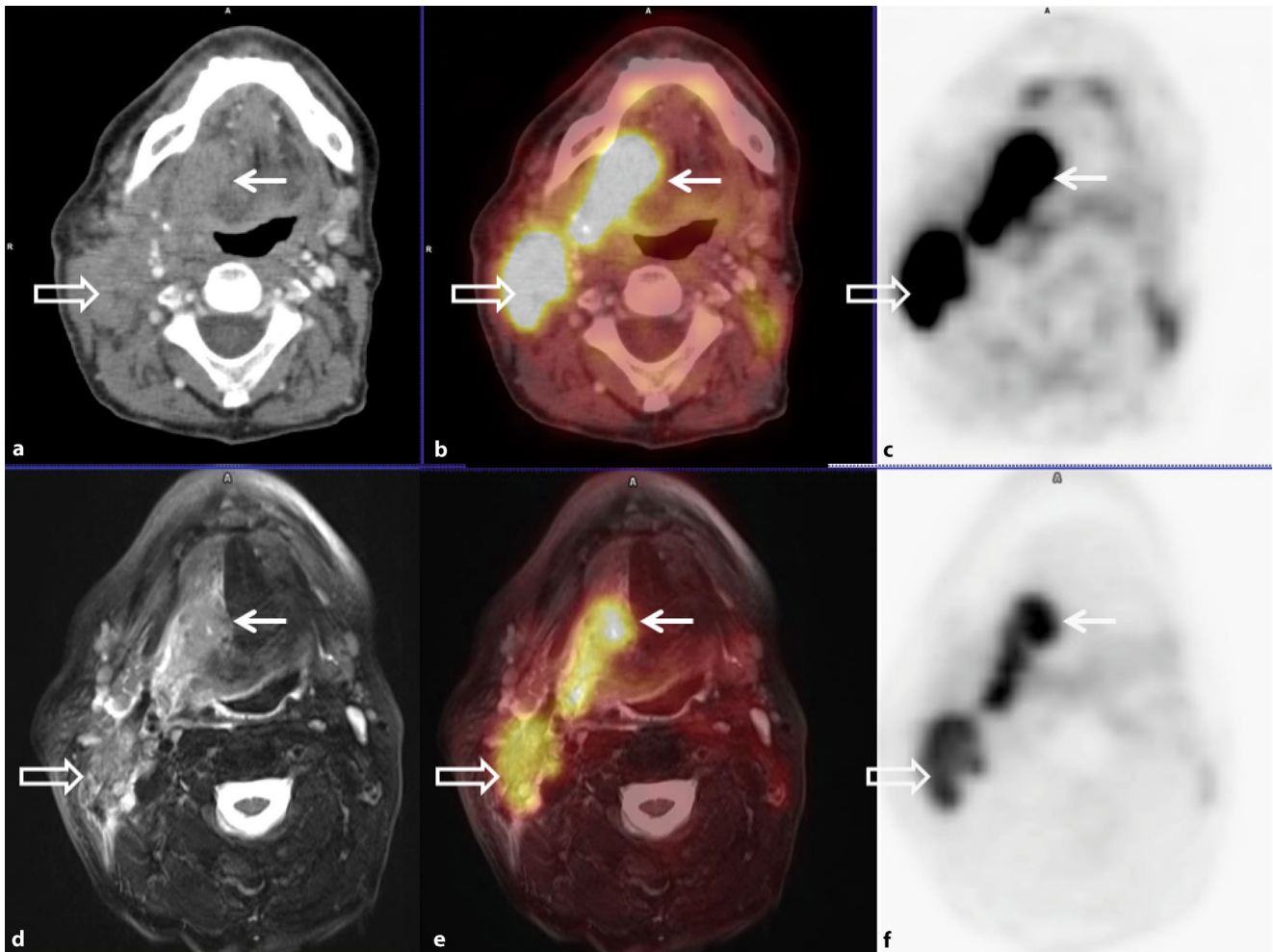
Abb. 1 ▲ 68-jähriger Patient mit rechtsseitigem Oropharynxkarzinom (*Pfeile*) und ipsilateralen Lymphknotenmetastasen (*offene Pfeile*). Vergleichbare Darstellung in der PET-CT (**a** kontrastmittelverstärktes CT-, **b** fusioniertes PET-CT- **c** PET-Bild) und in der PET-MRT (**d** fettgesättigte T2-TSE-, **e** fusionierte PET-MRT-, **f** PET-Bildgebung). *PET* Positronenemissionstomographie, *TSE* Turbospinecho

zum Staging mit CT oder MRT vergleichbar sind. Die hybride Bildgebung mit 18F-FDG-PET-CT liefert kombinierte anatomische und funktionelle Informationen und ermöglicht eine verbesserte Detektion. Einschränkungen bleiben bei Patienten ohne klinisch nachweisbare Lymphknotenmetastasen (cN0-Stadium gemäß TNM-Klassifikation). In einer Studie wurden nur 57 % der letzlich in der histopathologischen Untersuchung nachgewiesenen Lymphknotenmetastasen mit der präoperativen PET-CT erkannt [7]. Dies liegt sicherlich an den oft histologisch nachgewiesenen Mikrometastasen in zervikalen Lymphknoten, die aktuell der Detektion in sämtlichen bildgebenden Methoden entgehen. Die Autoren empfehlen daher aktuell weiter-

hin die „neck dissection" zum korrekten N-Staging.

In einer spezifischeren Metaanalyse bzgl. der Detektion zervikaler Lymphknotenmetastasen zeigten *Li et al.* [8] ebenfalls eine vergleichbare Genauigkeit von CT und MRT. Wurde die Detektion einzelner Lymphknoten als Zielgröße gewertet, wies die CT eine bessere Sensitivität von 77 % auf (MRT 72 %). Bei der Betrachtung der verschiedenen Lymphknoten(LK)-Level hingegen war die Sensitivität vergleichbar, die MRT hatte jedoch mit 81 % eine höhere Spezifität (CT 72 %).

Choi et al. [9] kamen in einer anderen Metaanalyse bereits 2010 zu dem Ergebnis, dass die 18F-FDG-PET oder -PET-CT insgesamt eine höhere diagnostische Genauigkeit als CT und MRT bzgl. der

Detektion zervikaler Lymphknotenmetastasen aufweisen, mit einer gepoolten Sensitivität von 82 % und Spezifität von 95 %.

Hinsichtlich der prognostisch relevanten Vorhersage einer extrakapsulären Tumorausbreitung in Lymphknoten erzielte die MRT eine höhere Genauigkeit im Vergleich zur CT (AUC-Werte [„area under the curve"] in der Receiver-Operating-Characteristic[ROC]-Analyse 0,9454 vs. 0,8615). Insgesamt waren jedoch in einer aktuellen Metaanalyse von *Su et al.* [10] zur extrakapsulären Tumorausbreitung keine allzu großen Unterschiede der Modalitäten feststellbar. Es ergaben sich eine mittlere Sensitivität und Spezifität von 85 bzw. 84 % für die MRT (CT 77 und 85 %, Ultraschall [US] 87 und 75 %, 18F-FDG-PET-CT 86

und 86 %). Der einzig signifikante Unterschied war die niedrigere Sensitivität der CT im Vergleich zum MRT.

Lonneux et al. [11] zeigten 2010 in einer prospektiven Multicenterstudie, dass die Hinzunahme der ^{18}F-FDG-PET zum sonstigen Staging (CT oder MRT der Halsregion plus CT des Thorax) in 13,7 % der Fälle zu einer relevanten Änderung des Therapieregimes bei Patienten mit Plattenepithelkarzinomen der Kopf-Hals-Region führte. Dabei resultierte in 5,2 % der Fälle ein Upstaging durch zusätzlich detektierte Lymphknotenmetastasen bzw. in 8,6 % durch Fernmetastasen. In einzelnen Fällen war die PET-Diagnostik mit ^{18}F-FDG bei sehr kleinen LK-Metastasen falschnegativ.

Bisherige Publikationen zur PET-MRT-Diagnostik bei Kopf-Hals-Tumoren

Die erste Publikation zur PET-MRT-Diagnostik bei Kopf-Hals-Tumoren stammt von *Platzek et al.* [12], die 2013 in einer Machbarkeitsstudie an 20 Patienten demonstrierten, dass der Tumornachweis in deren sequenziellem PET-MRT-System der alleinigen MRT- und der alleinigen PET-Diagnostik überlegen war. Dabei wurden von 20 histologisch gesicherten Tumoren in der MRT lediglich 13 bzw. 14 entdeckt, während in der ^{18}F-FDG-PET-MRT 17 Primärtumoren nachweisbar waren. Im Vergleich zu einer zusätzlich durchgeführten alleinigen ^{18}F-FDG-PET waren zudem deutlich mehr metastasensuspekte Lymphknoten sichtbar.

In einer späteren Studie zur Detektion von Lymphknotenmetastasen berichten die Autoren dann über einen direkten Vergleich der sequenziellen ^{18}F-FDG-PET-MRT zur Pathologie [13]. In dieser Studie wurden bei 38 Tumorpatienten in der PET-MRT 33 der Primärtumoren entdeckt, in der alleinigen MRT lediglich 28. Die meisten übersehenen Tumoren waren pT1-Karzinome von Zungenrand und Mundboden, allerdings wurde auch ein pT3-Tumor des weichen Gaumens in der alleinigen MRT nicht erkannt. Die Lymphknotenmetastasen wurden pro Level ausgewertet. Hierbei waren in der pathohistolo-

P. Stumpp · S. Purz · O. Sabri · T. Kahn

Molekulare Bildgebung bei Kopf-Hals-Tumoren. Perspektive der PET-MRT

Zusammenfassung

Hintergrund. Die ^{18}F-Fluordesoxyglukose-Positronenemissionstomographie-Computertomographie (^{18}F-FDG-PET-CT) hat ihren festen Stellenwert in der Diagnostik von Kopf-Hals-Tumoren. Seit einigen Jahren ist die PET-MRT als weitere hybride Bildgebungsmodalität verfügbar.
Fragestellung. Bringt die PET-MRT Fortschritte bei der Diagnostik von Kopf-Hals-Tumoren?
Material und Methode. Darstellung der diagnostischen Genauigkeit der bisherigen Bildgebungsmethoden CT, MRT und PET-CT anhand von Metaanalysen und Zusammenfassung der bisherigen Publikationen zur PET-MRT auf diesem Gebiet.
Ergebnisse. Die PET-MRT zeigt in allen bisherigen Studien keine Überlegenheit bzgl. der diagnostischen Genauigkeit von Kopf-Hals-Tumoren. Sie kann jedoch durch die multiparametrische Diagnostik perspektivisch Beiträge zur Tumorcharakterisierung und damit möglicherweise Voraussagen zum Therapieansprechen liefern.
Schlussfolgerungen. Derzeit wird die ^{18}F-FDG-PET-CT in der diagnostischen Genauigkeit bei Kopf-Hals-Tumoren von der PET-MRT nicht übertroffen. Der additive Wert der PET-MRT durch die multiparametrische Bildgebung muss weiter erforscht werden.

Schlüsselwörter

Metaanalysen · Multiparametrische Diagnostik · Tumorcharakterisierung · Therapieansprechen · Hybridbildgebung

Molecular imaging of head and neck cancers. Perspectives of PET/MRI

Abstract

Background. The ^{18}F-fluorodeoxyglucose positron emission tomography-computed tomography (^{18}F-FDG-PET/CT) procedure is a cornerstone in the diagnostics of head and neck cancers. Several years ago PET-magnetic resonance imaging (PET/MRI) also became available as an alternative hybrid multimodal imaging method.
Objective. Does PET/MRI have advantages over PET/CT in the diagnostics of head and neck cancers?
Material and methods. The diagnostic accuracy of the standard imaging methods CT, MRI and PET/CT is depicted according to currently available meta-analyses and studies concerning the use of PET/MRI for these indications are summarized.
Results. In all studies published up to now PET/MRI did not show superiority regarding the diagnostic accuracy in head and neck cancers; however, there is some evidence that in the future PET/MRI can contribute to tumor characterization and possibly be used to predict tumor response to therapy with the use of multiparametric imaging.
Conclusion. Currently, ^{18}F-FDG-PET/CT is not outperformed by PET/MRI in the diagnostics of head and neck cancers. The additive value of PET/MRI due to the use of multiparametric imaging needs to be investigated in future research.

Keywords

Meta-analyses · Multiparametric diagnostics · Tumor characterization · Therapy response · Multimodal imaging

gischen Untersuchung in 38/391 Leveln Metastasen nachweisbar. In der Bildgebung wurden in der PET-MRT und der alleinigen PET zwar mehr Metastasen erkannt, der Unterschied zur alleinigen MRT war jedoch nicht statistisch signifikant (AUC in der ROC-Analyse 0,96, 0,95 und 0,9).

Eine Studie von *Kubiessa et al.* [14] umfasste 17 konsekutive Patienten mit Kopf-Hals-Tumoren (Primärtumoren und Rezidive). Bei insgesamt 23 detektierten Tumorlokalisationen (Primum und Lymphknoten) war die simultane ^{18}F-FDG-PET-MRT der -PET-CT gleichwertig bei Sensitivität, Spezifität, positivem und negativem Prädiktivwert

Tab. 1 Auflistung der bisher publizierten Studien zur diagnostischen Genauigkeit der 18F-FDG-PET-MRT bei Kopf-Hals-Tumoren

Autor	Jahr	Patienten (n)	Primärtumoren (P) oder Rezidive (R)	PET-MRT-Technik	Kernaussage
Platzek et al. [12]	2013	20	P	Sequenziell	PET-MRT detektiert mehr Tumoren als die alleinige MRT und mehr LK-Metastasen als die alleinige PET
Platzek et al. [13]	2014	38	P	Sequenziell	PET-MRT detektiert mehr Primärtumoren als die alleinige MRT (v. a. pT1-Tumoren), kein signifikanter Unterschied bei LK-Metastasen-Detektion
Kubiessa et al. [14]	2014	17	P + R	Simultan	PET-MRT und PET-CT gleichwertig bzgl. diagnostischer Genauigkeit
Partovi et al. [15]	2014	14	P + R	Sequenziell	PET-MRT und PET-CT gleichwertig bzgl. Tumordetektion
Kuhn et al. [16]	2014	150	P + R	Sequenziell	PET-MRT mit höherer Auffälligkeit von Läsionen und höherer diagnostischer Sicherheit der Auswerter, Vorteile v. a. bei perineuralem Tumorwachstum und Weichteilinfiltration von Epipharynx, Zunge und Larynx
Lee et al. [17]	2014	10	P	Simultan	Kombinierte PET-MRT detektiert deutlich mehr suspekte LK als die alleinige MRT der Halsregion (aber LK-Metastasen nicht verifiziert)
Varoquaux et al. [18]	2014	32	P + R	Sequenziell	PET-MRT und PET-CT vergleichbar bzgl. Anzahl der detektierten Tumorherde
Schaarschmidt et al. [19]	2016	25	P + R	Simultan	Keine Unterschiede zwischen PET-MRT, PET-CT und MRT bei Staging und Restaging
Queiroz et al. [20]	2014	87	R	Sequenziell	PET-MRT und PET-CT mit vergleichbarer diagnostischer Genauigkeit bei Detektion von Tumorrezidiven

FDG Fluordesoxyglukose, *PET* Positronenemissionstomographie, *LK* Lymphknoten

(PPV und NPV) von 80,5, 88,2, 75,6 und 92,5 % (entsprechende Werte der PET-CT 82,7, 87,3, 73,2 und 92,4 %).

Auch *Partovi et al.* [15] fanden bei 14 Patienten keinen Unterschied in der Tumordetektion zwischen 18F-FDG-PET-CT und sequenzieller -PET-MRT. Hier wurden jedoch vorrangig die in der PET detektierten Läsionen verglichen, die entsprechenden CT- und MRT-Datensätze waren hauptsächlich zur Schwächungskorrektur und anatomischen Korrelation angefertigt und nicht zur dezidierten Halsdiagnostik. Detailliert verglichen wurden hier die Standardized-uptake-value(SUV)-Werte der beiden Modalitäten, wobei diese in der PET-MRT konstant höher lagen, insgesamt jedoch eine sehr hohe Korrelation mit den Werten aus der PET-CT aufwiesen (�‌ **Abb. 1**).

Die bisher größte Serie wurde von *Kuhn et al.* [16] aus Zürich publiziert, wo die Kollegen an 150 Patienten einerseits die 18F-FDG-PET-CT und die sequenzielle -PET-MRT verglichen, andererseits aber auch untersuchten, welche Sequenzen für die PET-MRT diagnostisch relevant sind. Typische Kennzahlen zur diagnostischen Genauigkeit

(Sensitivität, Spezifität, PPV und NPV) wurden hier nicht angegeben. Stattdessen berichten die Autoren über eine höhere Auffälligkeit pathologischer Läsionen (insbesondere der Primärtumoren) in der PET-MRT. Auch die diagnostische Sicherheit der Auswerter war bei der kontrastmittel(KM)-gestützten PET-MRT höher im Vergleich zur KM-gestützten PET-CT. Vorteile der kontrastverstärkten PET-MRT ergeben sich hiernach v. a. bei der Beurteilung perineuraler Tumorausbreitung und Infiltration der Weichteile im Bereich von Epipharynx, Zunge und Paralaryngealraum, während das PET-CT-Bild in Einzelfällen hilfreicher war bzgl. knöcherner Arrosionen. Die Autoren folgern daraus, dass ein 18F-FDG-PET-MRT v. a. in präoperativen Situationen sinnvoll ist, in denen die Tumorausdehnung so genau wie möglich angegeben werden sollte. Für Follow-up-Untersuchungen hingegen empfehlen sie ein verkürztes PET-MRT-Protokoll ohne KM-Applikation.

In einer sehr präliminären retrospektiven Studie aus dem Jahr 2014 berichten *Lee et al.* [17] über 10 Patienten, bei denen eine simultane 18F-FDG-PET-MRT zum Tumorstaging durchgeführt wurde. Auffällig war eine deutlich höhere Anzahl an metastasensuspekten Lymphknoten im PET, wobei insbesondere die dedizierte Aufnahme der Halsregion 23 zusätzliche Herde ergab im Vergleich zur alleinigen Interpretation der MRT-Bilder. Eine starke Einschränkung der Studie ist die fehlende Validierung dieser suspekten Lymphknoten, die weder histologisch noch durch ein Follow-up gesichert wurden.

Varoquaux et al. [18] berichteten von 32 Patienten (13 zum Primärstaging, 19 bei Rezidivverdacht), die konsekutiv mit sequenzieller 18F-FDG-PET-MRT und -PET-CT untersucht wurden, wobei sowohl CT als auch MRT ohne Kontrastmittel akquiriert und vorwiegend zur anatomischen Zuordnung von Läsionen genutzt wurden. Die Anzahl an detektierten Läsionen war vergleichbar, interessant erscheint die systematische Unterschätzung der Glukoseutilisation in der zuerst durchgeführten PET-MRT gegenüber der PET-CT bei der Quantifizierung des Glukosestoffwech-
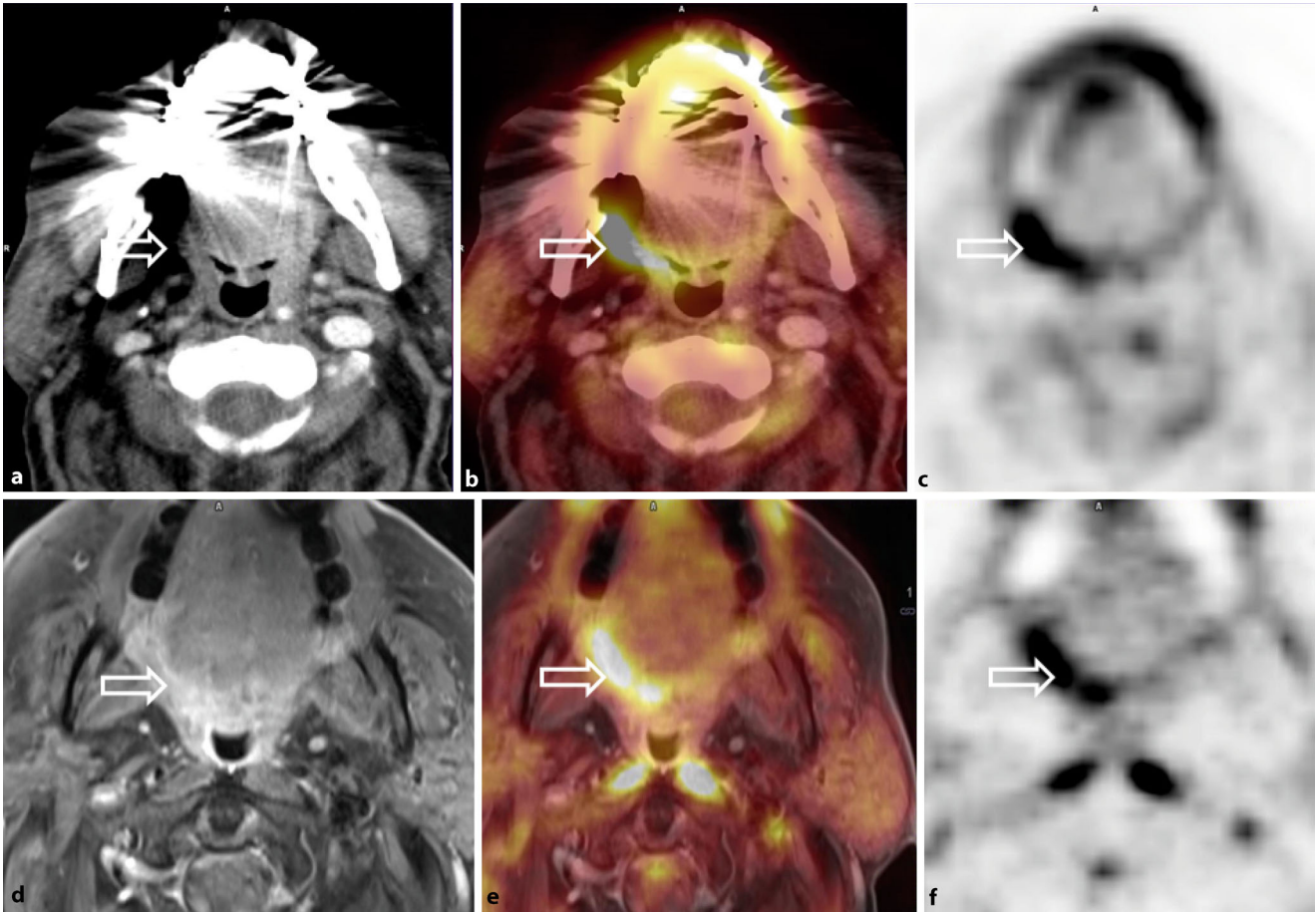
Abb. 2 ▲ 63-jähriger Patient mit rechtsseitigem Tonsillenkarzinom (*offene Pfeile*). Vorteile für die PET-MRT bei ausgeprägten Zahnfüllungsartefakten im CT. PET-CT: **a** kontrastmittelverstärktes CT ohne sicheren Tumornachweis bei Artefakten, **b** fusionierte PET-CT, **c** PET, jeweils mit Darstellung des Tumors. PET-MRT: **d** fettgesättigte T1-TSE mit tumorsuspekter Asymmetrie der Tonsillen, **e** fusionierte PET-MRT, **f** PET, jeweils mit Darstellung des Tumors, die symmetrische Glukosestoffwechselaktivität ventral des Atlas ist physiologisch im M. longus capitis. *PET* Positronenemissionstomographie, *TSE* Turbospinecho

sels mithilfe der SUV-Werte. Nach Ansicht der Autoren kann dies partiell auf einen durch die Tracerkinetik bedingten zeitabhängigen Anstieg der SUV-Werte in malignen Läsionen zurückgeführt werden.

In einer aktuellen Studie von *Schaarschmidt et al.* [19] wurde speziell das T- und N-Staging einer 18F-FDG-PET-CT-, simultanen -PET-MRT- und einer alleinigen MRT-Untersuchung verglichen. Die Unterschiede in der Genauigkeit des T-Stagings erreichten keine statistische Signifikanz, allerdings kann dies auch an der geringen Fallzahl liegen, da nur 12 der 25 Patienten im Rahmen eines Primärstagings untersucht wurden.

Bezüglich der Detektion von Rezidivtumoren kam eine eigene Studie mit 22 Patienten an einem simultanen PET-MRT-System zu dem Ergebnis einer höheren Sensitivität bei reduzierter Spezifität der 18F-FDG-PET-MRT im Vergleich zur PET-CT (Manuskript „under review").

Queiroz et al. [20] fanden mit der sequenziellen PET-MRT bei 87 Patienten keine signifikanten Unterschiede in der diagnostischen Genauigkeit bzgl. der Rezidivdiagnose. Allerdings hatten von diesen Patienten letztlich auch nur 16 ein Rezidiv, dabei war die diagnostische Genauigkeit der 18F-FDG-PET-MRT und der -PET-CT nahezu identisch (91,5 vs. 90,6 %; ◻ **Abb. 2**).

Eine kurze Übersicht der bisher erschienenen Artikel zum Vergleich von 18F-FDG-PET-MRT und -PET-CT gibt ◻ **Tab. 1**.

Insgesamt lässt sich zusammenfassen, dass die 18F-FDG-PET-MRT in den bisherigen Vergleichsstudien zur PET-CT zwar Vorteile in der Tumoranalyse hat, jedoch keine Überlegenheit in der diagnostischen Genauigkeit aufweist. Dies liegt möglicherweise daran, dass ein großer Teil der aktuell nicht entdeckten Tumorherde Mikrometastasen in zervikalen Lymphknoten umfasst, welche derzeit allen Bildgebungsmethoden entgehen. Hierfür sind neue Ansätze mit spezifischen MR-Kontrastmitteln oder spezifischen Radiotracern wie beispielsweise dem 3'-Deoxy-3'-[18F]Fluorthymidin (18F-FLT) als Proliferationsmarker oder dem Hypoxiemarker 18F-Fluormisonidazol (18F-FMISO) nötig.

Zunehmend wird auch bei Kopf-Hals-Tumoren untersucht, welche zusätzlichen Informationen die PET-MRT im Vergleich zur PET-CT bringen kann, dabei rückt insbesondere die multipa-
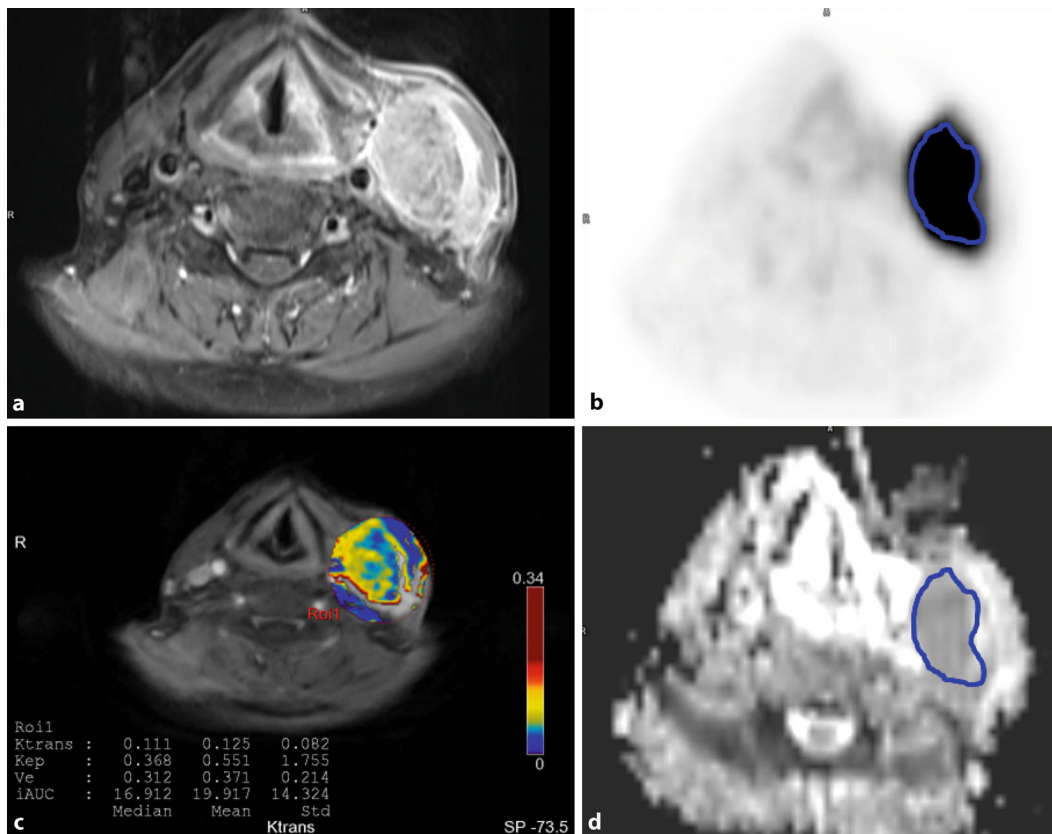
Abb. 3 ◂ 58-jähriger Patient mit linksseitiger Lymphknotenmetastase (LKM). Exemplarische Darstellung der multiparametrischen Bildgebung. **a** Fettgesättigtes T1-TSE-Bild nach Kontrastmittelgabe mit großer Lymphknotenmetastase links im Level III. **b** Ausgeprägte Stoffwechselaktivität der LKM in der ^{18}F-FDG-PET. **c** Parameterkarte für K^{trans} (Rate von Kontrastmittelaustritt aus dem Gefäß in den Extrazellularraum). Die Zahlenwerte im Bild geben auch die Daten für die anderen Parameter K$_{ep}$ und V$_e$ an. **d** Deutliche Signalabsenkung in der ADC-Map aus der diffusionsgewichteten Bildgebung. *TSE* Turbospinecho, *FDG* Fluordesoxyglukose, *PET* Positronenemissionstomographie, *ADC* „apparent diffusion coeffizient"

rametrische Bildgebung in den Mittelpunkt.

Multiparametrische Bildgebung

Die ^{18}F-FDG-PET ermöglicht bekanntermaßen die funktionelle Darstellung der Glukosestoffwechselaktivität von Gewebe [21]. Für die MRT wurde in den vergangenen Jahren die Diffusionswichtung („diffusion-weighted imaging", DWI), mit der die Brown-Molekularbewegung sichtbar gemacht werden kann, zunehmend auch außerhalb der neuroradiologischen Diagnostik angewendet. Eine eingeschränkte Diffusibilität im Extrazellularraum durch zelluläre Ödeme oder eine erhöhte Zelldichte, wie z. B. in manchen Tumoren, führt dabei zu einem erhöhten Signal im b-Bild und einer Absenkung in der ADC-Karte [22]. Eine weitere Möglichkeit, Gewebefunktionen mit der MRT zu charakterisieren, ergibt sich durch die kontrastmittelverstärkte Perfusionsanalyse („dynamic contrast-enhanced MRI", DCE-MRI [23]). Hier können qualitativ Durchblutungscharakteristika angegeben werden, wie die

Anstiegssteilheit der Signalintensität nach KM-Applikation oder die Art des Kurvenverlaufs. Bei Anwendung bestimmter Perfusionsmodelle ist jedoch auch eine quantitative Beschreibung der Gewebeperfusion möglich. Eines der am häufigsten verwendeten Modelle ist das Zwei-Kompartment-Modell von Tofts et al. [24]. Hier werden verschiedene Parameter berechnet: die Rate von Kontrastmittelaustritt aus dem Gefäß in den Extrazellularraum (K^{trans}), die Konstante des Rückstroms von KM in das Gefäß (K$_{ep}$) und das Volumen des Extrazellulärraums (V$_e$).

„Diffusion-weighted imaging"

Queiroz et al. [25] berichteten 2014 von einer prospektiven Studie zur Verwendung der DWI in der Detektion von Kopf-Hals-Tumoren. Dazu werteten sie die ^{18}F-FDG-PET-MRT-Daten von 70 Patienten (16 Primärstaging, 56 Follow-up) aus. Hierbei fanden die Autoren keinen Zusatznutzen der DWI im Vergleich zum PET-MRT-Datensatz. Insgesamt war die diagnostische Genauigkeit der

DWI allein im Vergleich zur PET-MRT ohne DWI signifikant niedriger (60,6 vs. 86,8 %, $p < 0,001$). Auch die einzelnen wenigen, korrekt als Metastasen erkannten Lymphknoten aus der DWI, die in der sequenziellen PET-MRT nicht erkannt worden waren, trugen nicht zu einer Änderung des N-Stagings bei. Die Autoren folgern daraus, dass die DWI keinen Zusatznutzen bringt und bei der Untersuchung von Patienten mit Kopf-Hals-Tumoren nicht eingesetzt werden sollte.

Nakajo et al. [26] postulierten im Gegensatz dazu in einer Studie von 2012 eine signifikante negative Korrelation von SUV und ADC, sodass die DWI bzw. die Bestimmung des ADC-Werts für die frühe Responseevaluation von Bedeutung sein könnte.

Zu einer ähnlichen Aussage kamen 2014 Matoba et al. [27] in einer prospektiven Studie, deren Resultate die frühe Änderung des ADC-Werts als geeigneten Biomarker zur Vorhersage des Therapieansprechens bei radiochemotherapierten Kopf-Hals-Tumoren zeigten.

Tumorcharakterisierung

Aktuell ebenfalls vielversprechend erscheint die Nutzung der multiparametrischen PET-MRT zur genaueren Tumorcharakterisierung [28]. Bei einer genauen Analyse multimodaler Bildgebungsparameter mit Korrelation zur Histopathologie könnten künftig grundlegende Eigenschaften der Tumoren nichtinvasiv mittels kombinierter Bildgebung erkannt und idealerweise eine Vorhersage des Therapieansprechens möglich werden. Aber auch die alleinige Möglichkeit einer genauen Tumorcharakterisierung und der dann eventuell mögliche Verzicht auf eine bioptische Sicherung wäre für die Patienten ein großer Benefit, speziell im Falle schwer zugänglicher Tumoren [28–31].

In diesem Sinne untersuchten Gawlitza et al. [32] im Jahr 2015 die Korrelation multimodaler Parameter mittels simultaner ^{18}F-FDG-PET-MRT. Hierfür wurden 17 Patienten mit Kopf-Hals-Tumoren ausgewertet und die Parameter zur Glukoseutilisation (SUV), zur Diffusion (ADC) und Perfusion (K^{trans}, K_{ep}, V_e) quantifiziert. Moderate, aber signifikante Korrelationen konnten zwischen dem Glukosestoffwechsel und Parametern der Perfusionsmessung einerseits sowie der mittels DWI bestimmten Zelldichte andererseits nachgewiesen werden. Ebenso korrelierte die Zelldichte mit dem Volumen des Extrazellularraums. Dies führte die Autoren zu der Annahme, dass aus solchen Analysen komplementäre Informationen zu gewinnen sind, die für die Tumorcharakterisierung von Nutzen sein könnten. Diese Interpretation wird unterstützt durch eine ähnliche Studie von Covello et al. [33] an 44 Patienten. Hier wurde bei Patienten mit Primärtumoren der Kopf-Hals-Region eine signifikante, inverse Korrelation zwischen dem mittleren SUV-Wert und K^{trans} nachgewiesen (◘ **Abb. 3**).

Unsere Arbeitsgruppe ermittelte in weiteren Untersuchungen (Artikel akzeptiert bei *Oral Oncology*) Zusammenhänge zwischen Parametern der funktionellen Bildgebung und histopathologischen Parametern. Speziell zwischen K_{ep} und der histopathologisch ermittelten Gefäßfläche sowie zwischen dem ADC-Wert und dem Proliferationsmarker Ki-67 konnten dabei Korrelationen demonstriert werden.

Ob mit diesen Methoden tatsächlich eine genaue nichtinvasive Bestimmung von Tumorart und Ansprechverhalten unter Therapie möglich wird, werden künftige Untersuchungen an größeren Patientenkollektiven zeigen müssen. Es deutet sich jedoch an, dass der Vorteil der PET-MRT bei der Diagnostik von Kopf-Hals-Tumoren in diesem Bereich zu finden ist und nicht in einer höheren diagnostischen Genauigkeit im Vergleich zum PET-CT.

Fazit für die Praxis

- ▬ Molekulare Bildgebung mit der ^{18}F-FDG-PET-CT ist bei Kopf-Hals-Tumoren hilfreich beim primären Staging (insbesondere N- und M-Staging), bei der frühen Beurteilung des Therapieansprechens und bei der Differenzierung posttherapeutischer Veränderungen von Tumorrezidiven.
- ▬ Alle bisherigen Studien zur ^{18}F-FDG-PET-MRT bei Kopf-Hals-Tumoren zeigen eine vergleichbare diagnostische Genauigkeit gegenüber der PET-CT. Vorteile werden angegeben bzgl. der perineuralen Tumorausbreitung sowie der Infiltrationsbeurteilung in Epipharynx, Zunge und Larynx.
- ▬ Aktuell zeichnet sich ein Trend zur multiparametrischen Bildgebung mit der PET-MRT ab zur genaueren nichtinvasiven Tumorcharakterisierung, die perspektivisch auch bei Therapieentscheidungen eingesetzt werden könnte.

Korrespondenzadresse

Dr. P. Stumpp
Klinik und Poliklinik für Diagnostische und Interventionelle Radiologie, Universitätsklinikum Leipzig AöR
Liebigstrasse 20, 04103 Leipzig, Deutschland
patrick.stumpp@medizin.uni-leipzig.de

Einhaltung ethischer Richtlinien

Literatur

1. Saman DM (2012) A review of the epidemiology of oral and pharyngeal carcinoma: Update. Head Neck Oncol 4(1):1
2. Jemal A, Siegel R, Ward E, Hao Y, Xu J, Murray T et al (2008) Cancer statistics, 2008. CA Cancer J Clin 58(2):71–96
3. Forastiere A, Koch W, Trotti A, Sidransky D (2001) Head and neck cancer. N Engl J Med 345(26):1890–1900
4. Wehrl HF, Judenhofer MS, Wiehr S, Pichler BJ (2009) Pre-clinical PET/MR: technological advances and new perspectives in biomedical research. Eur J Nucl Med Mol Imaging 36(Suppl 1):S56–S68
5. Boss A, Stegger L, Bisdas S, Kolb A, Schwenzer N, Pfister M et al (2011) Feasibility of simultaneous PET/MR imaging in the head and upper neck area. Eur Radiol 21(7):1439–1446
6. Sarrión PMG, Bagán JV, Jiménez Y, Margaix M, Marzal C (2015) Utility of imaging techniques in the diagnosis of oral cancer. J Craniomaxillofac Surg 43(9):1880–1894
7. Ozer E, Naiboğlu B, Meacham R, Ryoo C, Agrawal A, Schuller DE (2012) The value of PET/CT to assess clinically negative necks. Eur Arch Otorhinolaryngol 269(11):2411–2414
8. Li L, Sun J, Li B, Li C, Li Y, Su F et al (2015) Computed tomography versus magnetic resonance imaging for diagnosing cervical lymph node metastasis of head and neck cancer: a systematic review and meta-analysis. Onco Targets Ther. doi:10.2147/OTT.S73924
9. Choi HJ, Ju W, Myung SK, Kim Y (2010) Diagnostic performance of computer tomography, magnetic resonance imaging, and positron emission tomography or positron emission tomography/computer tomography for detection of metastatic lymph nodes in patients with cervical cancer: Meta-analysis. Cancer Sci 101(6):1471–1479
10. Su Z, Duan Z, Pan W, Wu C, Jia Y, Han B et al (2016) Predicting extracapsular spread of head and neck cancers using different imaging techniques: A systematic review and meta-analysis. Int J Oral Maxillofac Surg 45(4):413–421
11. Lonneux M, Hamoir M, Reychler H, Maingon P, Duvillard C, Calais G et al (2010) Positron emission tomography with [18 F]fluorodeoxyglucose improves staging and patient management in patients with head and neck squamous cell carcinoma: a multicenter prospective study. J Clin Oncol 28(7):1190–1195
12. Platzek I, Beuthien-Baumann B, Schneider M, Gudziol V, Langner J, Schramm G et al (2013) PET/MRI in head and neck cancer: initial experience. Eur J Nucl Med Mol Imaging 40(1):6–11
13. Platzek I, Beuthien-Baumann B, Schneider M, Gudziol V, Kitzler HH, Maus J et al (2014) FDG PET/MR for lymph node staging in head and neck cancer. Eur J Radiol 83(7):1163–1168
14. Kubiessa K, Purz S, Gawlitza M, Kühn A, Fuchs J, Steinhoff KG et al (2014) Initial clinical results of simultaneous 18 F-FDG PET/MRI in comparison to 18 F-FDG PET/CT in patients with head and neck cancer. Eur J Nucl Med Mol Imaging 41(4):639–648
15. Partovi S, Kohan A, Vercher-Conejero JL, Rubbert C, Margevicius S, Schluchter MD et al (2014) Qualitative and quantitative performance of 18 F-FDG-PET/MRI versus 18 F-FDG-PET/CT in patients

with head and neck cancer. Am J Neuroradiol 35(10):1970–1975

16. Kuhn FP, Hüllner M, Mader CE, Kastrinidis N, Huber GF, Schulthess GK von et al (2014) Contrast-enhanced PET/MR imaging versus contrast-enhanced PET/CT in head and neck cancer: how much MR information is needed? J Nucl Med 55(4):551–558

17. Lee SJ, Seo HJ, Cheon GJ, Kim JH, Kim EE, Kang KW et al (2014) Usefulness of integrated PET/MRI in head and neck cancer: A preliminary study. Nucl Med Mol Imaging 48(2):98–105

18. Varoquaux A, Rager O, Poncet A, Delattre BMA, Ratib O, Becker CD et al (2014) Detection and quantification of focal uptake in head and neck tumours: (18)F-FDG PET/MR versus PET/CT. Eur J Nucl Med Mol Imaging 41(3):462–475

19. Schaarschmidt BM, Heusch P, Buchbender C, Ruhlmann M, Bergmann C, Ruhlmann V et al (2016) Locoregional tumour evaluation of squamous cell carcinoma in the head and neck area: a comparison between MRI, PET/CT and integrated PET/MRI. Eur J Nucl Med Mol Imaging 43:92–102

20. Queiroz MA, Hüllner M, Kuhn F, Huber G, Meerwein C, Kollias S et al (2014) PET/MRI and PET/CT in follow-up of head and neck cancer patients. Eur J Nucl Med Mol Imaging 41(6):1066–1075

21. Seemann MD (2004) PET/CT: fundamental principles. Eur J Med Res 9(5):241–246

22. Padhani AR, Liu G, Mu-Koh D, Chenevert TL, Thoeny HC, Takahara T et al (2009) Diffusion-weighted magnetic resonance imaging as a cancer Biomarker: consensus and recommendations. Neoplasia 11(2):102–125

23. Li SP, Padhani AR (2012) Tumor response assessments with diffusion and perfusion MRI. J Magn Reson Imaging 35(4):745–763

24. Tofts PS, Brix G, Buckley DL, Evelhoch JL, Henderson E, Knopp MV et al (1999) Estimating kinetic parameters from dynamic contrast-enhanced t1-weighted MRI of a diffusable tracer: Standardized quantities and symbols. J Magn Reson Imaging 10(3):223–232

25. Queiroz MA, Hüllner M, Kuhn F, Huber G, Meerwein C, Kollias S et al (2014) Use of diffusion-weighted imaging (DWI) in PET/MRI for head and neck cancer evaluation. Eur J Nucl Med Mol Imaging 41(12):2212–2221

26. Nakajo M, Nakajo M, Kajiya Y, Tani A, Kamiyama T, Yonekura R et al (2012) FDG PET/CT and diffusion-weighted imaging of head and neck squamous cell carcinoma: comparison of prognostic significance between primary tumor standardized uptake value and apparent diffusion coefficient. Clin Nucl Med 37(5):475–480

27. Matoba M, Tuji H, Shimode Y, Toyoda I, Kuginuki Y, Miwa K et al (2014) Fractional change in apparent diffusion coefficient as an imaging Biomarker for predicting treatment response in head and neck cancer treated with Chemoradiotherapy. AJNR Am J Neuroradiol 35(2):379–385

28. Bailey DL, Pichler BJ, Gückel B, Barthel H, Beer AJ, Bremerich J et al (2015) Combined PET/MRI: Multi-modality multi-parametric imaging is here: Summary Report of the 4th International Workshop on PET/MR Imaging; February 23–27, 2015, Tübingen, Germany. Mol Imaging Biol 17(5):595–608

29. Yankeelov TE, Peterson TE, Abramson RG, Izquierdo-Garcia D, Garcia-Izquierdo D, Arlinghaus LR et al (2012) Simultaneous PET-MRI in oncology: a solution looking for a problem? Magn Reson Imaging 30(9):1342–1356

30. Punwani S, Taylor SA, Saad ZZ, Bainbridge A, Groves A, Daw S et al (2013) Diffusion-weighted MRI of lymphoma: prognostic utility and implications for PET/MRI? Eur J Nucl Med Mol Imaging 40(3):373–385

31. Bailey DL, Antoch G, Bartenstein P, Barthel H, Beer AJ, Bisdas S et al (2015) Combined PET/MR: The real work has just started. Summary report of the Third International Workshop on PET/MR Imaging; February 17–21, 2014, Tübingen, Germany. Mol Imaging Biol 17(3):297–312

32. Gawlitza M, Purz S, Kubiessa K, Boehm A, Barthel H, Kluge R et al (2015) In vivo correlation of glucose metabolism, cell density and Microcirculatory parameters in patients with head and neck cancer: initial results using simultaneous PET/MRI. PLoS ONE 10(8):e0134749

33. Covello M, Cavaliere C, Aiello M, Cianelli MS, Mesolella M, Iorio B et al (2015) Simultaneous PET/MR head-neck cancer imaging: Preliminary clinical experience and multiparametric evaluation. Eur J Radiol 84(7):1269–1276

4. Literaturverzeichnis

1. Gemeinsamer Bundesausschuss (2015) Richtlinie des Gemeinsamen Bundesausschusses zu Untersuchungs- und Behandlungsmethoden der vertragsärztlichen Versorgung: Richtlinie Methoden vertragsärztliche Versorgung.

2. Reske SN, Kull T (2013) Indikationen der modernen PET/CT-Diagnostik. best practice onkologie 8(3):44–9.

3. Wei J, Pei S, Zhu X (2016) Comparison of (18)F-FDG PET/CT, MRI and SPECT in the diagnosis of local residual/recurrent nasopharyngeal carcinoma: A meta-analysis. Oral oncology 52:11–7.

4. Sheikhbahaei S, Marcus C, Hafezi-Nejad N, Taghipour M, Subramaniam RM (2015) Value of FDG PET/CT in Patient Management and Outcome of Skeletal and Soft Tissue Sarcomas. PET clinics 10(3):375–93.

5. Sheikhbahaei S, Marcus C, Subramaniam RM (2015) 18F FDG PET/CT and Head and Neck Cancer: Patient Management and Outcomes. PET clinics 10(2):125–45.

6. Sheikhbahaei S, Taghipour M, Ahmad R, Fakhry C, Kiess AP, Chung CH et al. (2015) Diagnostic Accuracy of Follow-Up FDG PET or PET/CT in Patients With Head and Neck Cancer After Definitive Treatment: A Systematic Review and Meta-Analysis. AJR. American journal of roentgenology 205(3):629–39.

7. Beadsmoore C, Newman D, MacIver D, Pawaroo D (2015) Positron Emission Tomography Computed Tomography: A Guide for the General Radiologist. Canadian Association of Radiologists journal = Journal l'Association canadienne des radiologistes 66(4):332–47.

8. Perng P, Marcus C, Subramaniam RM (2015) (18)F-FDG PET/CT and Melanoma: Staging, Immune Modulation and Mutation-Targeted Therapy Assessment, and Prognosis. AJR. American journal of roentgenology 205(2):259–70.

9. Shamim SA, Kumar A, Kumar R (2015) PET/Computed Tomography in Neuroendocrine Tumor: Value to Patient Management and Survival Outcomes. PET clinics 10(3):411–21.

10. Brunetti JC (2015) Fludeoxyglucose F 18 PET-Computed Tomography: Management Changes Effecting Patient Outcomes in Gynecologic Malignancies. PET clinics 10(3):395–409.

11. Laurens ST, Oyen WJG (2015) Impact of Fluorodeoxyglucose PET/Computed Tomography on the Management of Patients with Colorectal Cancer. PET clinics 10(3):345–60.

12. Kwee RM, Marcus C, Sheikhbahaei S, Subramaniam RM (2015) PET with Fluorodeoxyglucose F 18/Computed Tomography in the Clinical Management and Patient Outcomes of Esophageal Cancer. PET clinics 10(2):197–205.

13. Goense L, van Rossum PSN, Reitsma JB, Lam MG, Meijer GJ, van Vulpen M et al. (2015) Diagnostic Performance of (18)F-FDG PET and PET/CT for the Detection of Recurrent Esophageal Cancer After Treatment with Curative Intent: A Systematic Review and Meta-Analysis. Journal of Nuclear Medicine 56(7):995–1002.

14. Rohren EM (2015) PET/Computed Tomography and Patient Outcomes in Melanoma. PET clinics 10(2):243–54.

15. Lebron L, Greenspan D, Pandit-Taskar N (2015) PET Imaging of Breast Cancer: Role in Patient Management. PET clinics 10(2):159–95.

16. Pawaskar AS, Basu S (2015) Role of 2-Fluoro-2-Deoxyglucose PET/Computed Tomography in Carcinoma of Unknown Primary. PET clinics 10(3):297–310.

17. Murphy RC, Kawashima A, Peller PJ (2011) The utility of 11C-choline PET/CT for imaging prostate cancer: a pictorial guide. AJR. American journal of roentgenology 196(6):1390–8.

18. Afshar-Oromieh A, Zechmann CM, Malcher A, Eder M, Eisenhut M, Linhart HG et al. (2014) Comparison of PET imaging with a (68)Ga-labelled PSMA ligand and (18)F-choline-based PET/CT for the diagnosis of recurrent prostate cancer. European journal of nuclear medicine and molecular imaging 41(1):11–20.

19. Kitagawa Y, Nishizawa S, Sano K, Ogasawara T, Nakamura M, Sadato N et al. (2003) Prospective Comparison of 18F-FDG PET with Conventional Imaging Modalities (MRI, CT, and 67Ga Scintigraphy) in Assessment of Combined Intraarterial Chemotherapy and Radiotherapy for Head and Neck Carcinoma. Journal of Nuclear Medicine.

20. Loeffelbein DJ, Souvatzoglou M, Wankerl V, Dinges J, Ritschl LM, Mücke T et al. (2014) Diagnostic value of retrospective PET-MRI fusion in head-and-neck cancer. BMC cancer 14:846.

21. Loeffelbein DJ, Souvatzoglou M, Wankerl V, Martinez-Möller A, Dinges J, Schwaiger M et al. (2012) PET-MRI fusion in head-and-neck oncology: current status and implications for hybrid PET/MRI. Journal of oral and maxillofacial surgery 70(2):473–83.

22. Kanda T, Kitajima K, Suenaga Y, Konishi J, Sasaki R, Morimoto K et al. (2013) Value of retrospective image fusion of ^{18}F-FDG PET and MRI for preoperative staging of head and neck cancer: comparison with PET/CT and contrast-enhanced neck MRI. European journal of radiology 82(11):2005–10.

23. Kitajima K, Suenaga Y, Ueno Y, Kanda T, Maeda T, Takahashi S et al. (2013) Value of fusion of PET and MRI for staging of endometrial cancer: comparison with ^{18}F-FDG contrast-enhanced PET/CT and dynamic contrast-enhanced pelvic MRI. European journal of radiology 82(10):1672–6.

24. Kitajima K, Suenaga Y, Ueno Y, Kanda T, Maeda T, Makihara N et al. (2014) Value of fusion of PET and MRI in the detection of intra-pelvic recurrence of gynecological tumor: comparison with 18F-FDG contrast-enhanced PET/CT and pelvic MRI. Annals of nuclear medicine 28(1):25–32.

25. Wang Y, Lim R, Ali Khawaja RD, Blake MA (2015) Improving Concordance of MRI and PET/CT Interpretations With Retrospectively Coregistered MRI and PET/CT Data Sets. Current problems in diagnostic radiology 44(3):232–6.

26. Zaidi H, Montandon M, Alavi A (2010) The clinical role of fusion imaging using PET, CT, and MR imaging. Magnetic resonance imaging clinics of North America 18(1):133–49.

27. Nagamachi S, Nishii R, Wakamatsu H, Mizutani Y, Kiyohara S, Fujita S et al. (2013) The usefulness of (18)F-FDG PET/MRI fusion image in diagnosing pancreatic tumor: comparison with (18)F-FDG PET/CT. Annals of nuclear medicine 27(6):554–63.

28. Pichler BJ, Wehrl HF, Kolb A, Judenhofer MS (2008) Positron emission tomography/magnetic resonance imaging: the next generation of multimodality imaging? Seminars in nuclear medicine 38(3):199–208.

29. Antoch G, Bockisch A (2009) Combined PET/MRI: a new dimension in whole-body oncology imaging? European journal of nuclear medicine and molecular imaging 36 Suppl 1:S113-20.

30. Sauter AW, Wehrl HF, Kolb A, Judenhofer MS, Pichler BJ (2010) Combined PET/MRI: one step further in multimodality imaging. Trends in molecular medicine 16(11):508–15.

31. Pichler BJ, Kolb A, Nägele T, Schlemmer H (2010) PET/MRI: paving the way for the next generation of clinical multimodality imaging applications. Journal of Nuclear Medicine 51(3):333–6.

32. Beyer T, Freudenberg LS, Czernin J, Townsend DW (2011) The future of hybrid imaging-part 3: PET/MR, small-animal imaging and beyond. Insights into imaging 2(3):235–46.

33. Brendle CB, Schmidt H, Fleischer S, Braeuning UH, Pfannenberg CA, Schwenzer NF (2013) Simultaneously acquired MR/PET images compared with sequential MR/PET and PET/CT: alignment quality. Radiology 268(1):190–9.

34. Boss A, Stegger L, Bisdas S, Kolb A, Schwenzer N, Pfister M et al. (2011) Feasibility of simultaneous PET/MR imaging in the head and upper neck area. European radiology 21(7):1439–46.

35. Wehrl HF, Judenhofer MS, Wiehr S, Pichler BJ (2009) Pre-clinical PET/MR: technological advances and new perspectives in biomedical research. European journal of nuclear medicine and molecular imaging 36 Suppl 1:S56-68.

36. Schlemmer HW, Pichler BJ, Schmand M, Burbar Z, Michel C, Ladebeck R et al. (2008) Simultaneous MR/PET imaging of the human brain: feasibility study. Radiology 248(3):1028–35.

37. Schulthess GK von, Schlemmer HW (2009) A look ahead: PET/MR versus PET/CT. European journal of nuclear medicine and molecular imaging 36 Suppl 1:S3-9.

38. Zaidi H, Del Guerra A (2011) An outlook on future design of hybrid PET/MRI systems. Medical physics 38(10):5667–89.

39. Ratib O, Beyer T (2011) Whole-body hybrid PET/MRI: ready for clinical use? European journal of nuclear medicine and molecular imaging 38(6):992–5.

40. Delso G, Ziegler S (2009) PET/MRI system design. European journal of nuclear medicine and molecular imaging 36 Suppl 1:S86-92.

41. Bailey DL, Barthel H, Beyer T, Boellaard R, Gückel B, Hellwig D et al. (2013) Summary report of the First International Workshop on PET/MR imaging, March 19-23, 2012, Tübingen, Germany. Molecular imaging and biology 15(4):361–71.

42. Zaidi H, Ojha N, Morich M, Griesmer J, Hu Z, Maniawski P et al. (2011) Design and performance evaluation of a whole-body Ingenuity TF PET-MRI system. Physics in medicine and biology 56(10):3091–106.

43. Delso G, Fürst S, Jakoby B, Ladebeck R, Ganter C, Nekolla SG et al. (2011) Performance measurements of the Siemens mMR integrated whole-body PET/MR scanner. Journal of Nuclear Medicine 52(12):1914–22.

44. Kinahan PE, Hasegawa BH, Beyer T (2003) X-ray-based attenuation correction for positron emission tomography/computed tomography scanners. Seminars in nuclear medicine 33(3):166–79.

45. Townsend DW (2004) Physical principles and technology of clinical PET imaging. Annals of the Academy of Medicine, Singapore 33(2):133–45.

46. Bailet JW, Sercarz JA, Abemayor E, Anzai Y, Lufkin RB, Hoh CK (1995) The use of positron emission tomography for early detection of recurrent head and neck squamous cell carcinoma in postradiotherapy patients. The Laryngoscope 105(2):135–9.

47. Bailey DL (1998) Transmission scanning in emission tomography. European journal of nuclear medicine 25(7):774–87.

48. Townsend DW, Beyer T, Blodgett TM (2003) PET/CT scanners: a hardware approach to image fusion. Seminars in nuclear medicine 33(3):193–204.

49. Bockisch A, Beyer T, Antoch G, Freudenberg LS, Kuhl H, Debatin JF et al. (2004) Positron emission tomography/computed tomography - imaging protocols, artifacts, and pitfalls. Molecular imaging and biology 6(4):188–99.

50. Seemann MD (2004) PET/CT: fundamental principles. European journal of medical research 9(5):241–6.

51. Dixon WT (1984) Simple proton spectroscopic imaging. Radiology 153(1):189–94.

52. Martinez-Möller A, Souvatzoglou M, Delso G, Bundschuh RA, Chefd'hotel C, Ziegler SI et al. (2009) Tissue classification as a potential approach for attenuation correction in whole-body PET/MRI: evaluation with PET/CT data. Journal of Nuclear Medicine 50(4):520–6.

53. Schulz V, Torres-Espallardo I, Renisch S, Hu Z, Ojha N, Börnert P et al. (2011) Automatic, three-segment, MR-based attenuation correction for whole-body PET/MR data. European journal of nuclear medicine and molecular imaging 38(1):138–52.

54. Steinberg J, Jia G, Sammet S, Zhang J, Hall N, Knopp MV (2010) Three-region MRI-based whole-body attenuation correction for automated PET reconstruction. Nuclear medicine and biology 37(2):227–35.

55. Kim JH, Lee JS, Song I, Lee DS (2012) Comparison of segmentation-based attenuation correction methods for PET/MRI: evaluation of bone and liver standardized uptake value with oncologic PET/CT data. Journal of Nuclear Medicine 53(12):1878–82.

56. Payabvash S, Meric K, Cayci Z (2016) Differentiation of benign from malignant cervical lymph nodes in patients with head and neck cancer using PET/CT imaging. Clinical imaging 40(1):101–5.

57. Rahbar K, Seifarth H, Schafers M, Stegger L, Hoffmeier A, Spieker T et al. (2012) Differentiation of malignant and benign cardiac tumors using 18F-FDG PET/CT. Journal of Nuclear Medicine 53(6):856–63.

58. Takanami K, Hiraide T, Tsuda M, Nakamura Y, Kaneta T, Takase K et al. (2011) Additional value of FDG PET/CT to contrast-enhanced CT in the differentiation between benign and malignant intraductal papillary mucinous neoplasms of the pancreas with mural nodules. Annals of nuclear medicine 25(7):501–10.

59. Cho A, Hur J, Kang WJ, Cho HJ, Lee J, Yun M et al. (2011) Usefulness of FDG PET/CT in determining benign from malignant endobronchial obstruction. European radiology 21(5):1077–87.

60. Ozcan Kara P, Kara T, Kara Gedik G, Kara F, Sahin O, Ceylan Gunay E et al. (2011) The role of fluorodeoxyglucose-positron emission tomography/computed tomography in differentiating between benign and malignant adrenal lesions. Nuclear medicine communications 32(2):106–12.

61. Suzuki R, Watanabe H, Yanagawa T, Sato J, Shinozaki T, Suzuki H et al. (2005) PET evaluation of fatty tumors in the extremity: possibility of using the standardized uptake value (SUV) to differentiate benign tumors from liposarcoma. Annals of nuclear medicine 19(8):661–70.

62. Demura Y, Tsuchida T, Ishizaki T, Mizuno S, Totani Y, Ameshima S et al. (2003) 18F-FDG accumulation with PET for differentiation between benign and malignant lesions in the thorax. Journal of Nuclear Medicine 44(4):540–8.

63. Maffione AM, Marzola MC, Capirci C, Colletti PM, Rubello D (2015) Value of (18)F-FDG PET for Predicting Response to Neoadjuvant Therapy in Rectal Cancer: Systematic Review and Meta-Analysis. AJR. American journal of roentgenology 204(6):1261–8.

64. Schmidt T, Lordick F, Herrmann K, Ott K (2015) Value of functional imaging by PET in esophageal cancer. Journal of the National Comprehensive Cancer Network JNCCN 13(2):239–47.

65. Lordick F (2012) Optimizing neoadjuvant chemotherapy through the use of early response evaluation by positron emission tomography. Recent results in cancer research. Fortschritte der Krebsforschung. Progres dans les recherches sur le cancer 196:201–11.

66. Bai B, Bading J, Conti PS (2013) Tumor quantification in clinical positron emission tomography. Theranostics 3(10):787–801.

67. Wiesmuller M, Quick HH, Navalpakkam B, Lell MM, Uder M, Ritt P et al. (2013) Comparison of lesion detection and quantitation of tracer uptake between PET from a simultaneously acquiring whole-body PET/MR hybrid scanner and PET from PET/CT. European journal of nuclear medicine and molecular imaging 40(1):12–21.

68. Drzezga A, Souvatzoglou M, Eiber M, Beer AJ, Furst S, Martinez-Moller A et al. (2012) First clinical experience with integrated whole-body PET/MR: comparison to PET/CT in patients with oncologic diagnoses. Journal of Nuclear Medicine 53(6):845–55.

69. Varoquaux A, Rager O, Poncet A, Delattre BMA, Ratib O, Becker CD et al. (2014) Detection and quantification of focal uptake in head and neck tumours: (18)F-FDG PET/MR versus PET/CT. European journal of nuclear medicine and molecular imaging 41(3):462–75.

70. Yankeelov TE, Peterson TE, Abramson RG, Izquierdo-Garcia D, Garcia-Izquierdo D, Arlinghaus LR et al. (2012) Simultaneous PET-MRI in oncology: a solution looking for a problem? Magnetic resonance imaging 30(9):1342–56.

71. Johnbeck CB, Knigge U, Kjaer A (2014) PET tracers for somatostatin receptor imaging of neuroendocrine tumors: current status and review of the literature. Future oncology 10(14):2259–77.

72. Brix G, Lechel U, Glatting G, Ziegler SI, Munzing W, Muller SP et al. (2005) Radiation exposure of patients undergoing whole-body dual-modality 18F-FDG PET/CT examinations. Journal of Nuclear Medicine 46(4):608–13.

73. Huang B, Law MW, Khong P (2009) Whole-body PET/CT scanning: estimation of radiation dose and cancer risk. Radiology 251(1):166–74.

74. Hirsch FW, Sattler B, Sorge I, Kurch L, Viehweger A, Ritter L et al. (2013) PET/MR in children. Initial clinical experience in paediatric oncology using an integrated PET/MR scanner. Pediatric radiology 43(7):860–75.

75. Castelijns JA (2011) PET-MRI in the head and neck area: challenges and new directions. European radiology 21(11):2425–6.

76. Tsouana E, Stoneham S, Fersht N, Kitchen N, Gaze M, Bomanji J et al. (2015) Evaluation of treatment response using integrated 18F-labeled choline positron emission tomography/magnetic resonance imaging in adolescents with intracranial non-germinomatous germ cell tumours. Pediatric blood & cancer 62(9):1661–3.

77. Afshar-Oromieh A, Wolf MB, Kratochwil C, Giesel FL, Combs SE, Dimitrakopoulou-Strauss A et al. (2015) Comparison of (6)(8)Ga-DOTATOC-PET/CT and PET/MRI hybrid systems in patients with cranial meningioma: Initial results. Neuro-oncology 17(2):312–9.

78. Barthel H, Schroeter ML, Hoffmann K, Sabri O (2015) PET/MR in dementia and other neurodegenerative diseases. Seminars in nuclear medicine 45(3):224–33.

79. Werner P, Barthel H, Drzezga A, Sabri O (2015) Current status and future role of brain PET/MRI in clinical and research settings. European journal of nuclear medicine and molecular imaging 42(3):512–26.

80. Puttick S, Bell C, Dowson N, Rose S, Fay M (2015) PET, MRI, and simultaneous PET/MRI in the development of diagnostic and therapeutic strategies for glioma. Drug discovery today 20(3):306–17.

81. Nensa F, Beiderwellen K, Heusch P, Wetter A (2014) Clinical applications of PET/MRI: current status and future perspectives. Diagnostic and interventional radiology (Ankara, Turkey) 20(5):438–47.

82. Preuss M, Werner P, Barthel H, Nestler U, Christiansen H, Hirsch FW et al. (2014) Integrated PET/MRI for planning navigated biopsies in pediatric brain tumors. Pediatric Neurosurgery 30(8):1399–403.

83. Werner P, Saur D, Zeisig V, Ettrich B, Patt M, Sattler B et al. (2015) Simultaneous PET/MRI in stroke: a case series. Journal of cerebral blood flow and metabolism 35(9):1421–5.

84. Nekolla SG, Rischpler C (2015) Assessing myocardial metabolism with hybrid PET imaging: instrumentation, concepts, and workflows. Current pharmaceutical design 22:96–104.

85. Nappi C, Altiero M, Imbriaco M, Nicolai E, Giudice CA, Aiello M et al. (2015) First experience of simultaneous PET/MRI for the early detection of cardiac involvement in patients with Anderson-Fabry disease. European journal of nuclear medicine and molecular imaging 42(7):1025–31.

86. Rischpler C, Langwieser N, Souvatzoglou M, Batrice A, van Marwick S, Snajberk J et al. (2015) PET/MRI early after myocardial infarction: evaluation of viability with late gadolinium enhancement transmurality vs. 18F-FDG uptake. European heart journal cardiovascular Imaging 16(6):661–9.

87. Rischpler C, Nekolla SG, Kunze KP, Schwaiger M (2015) PET/MRI of the heart. Seminars in nuclear medicine 45(3):234–47.

88. Glaudemans, Andor W J M, Quintero AM, Signore A (2012) PET/MRI in infectious and inflammatory diseases: will it be a useful improvement? European journal of nuclear medicine and molecular imaging 39(5):745–9.

89. Fahnert J, Purz S, Javers J, Heyde C, Barthel H, Stumpp P et al. (2016) The use of simultaneous 18F-FDG-PET/MRI for the detection of spondylodiscitis. Journal of nuclear medicine official publication, Society of Nuclear Medicine. doi:10.2967/jnumed.115.171561.

90. Yamashita H, Kubota K, Mimori A (2014) Clinical value of whole-body PET/CT in patients with active rheumatic diseases. Arthritis research & therapy 16(5):423.

91. Mihailovic J, Goldsmith SJ (2015) Multiple myeloma: 18F-FDG-PET/CT and diagnostic imaging. Seminars in nuclear medicine 45(1):16–31.

92. Schwenzer NF, Pfannenberg AC (2015) PET/CT, MR, and PET/MR in Lymphoma and Melanoma. Seminars in nuclear medicine 45(4):322–31.

93. Hartung-Knemeyer V, Beiderwellen KJ, Buchbender C, Kuehl H, Lauenstein TC, Bockisch A et al. (2013) Optimizing positron emission tomography image acquisition protocols in integrated positron emission tomography/magnetic resonance imaging. Investigative radiology 48(5):290–4.

94. Luna A, Pahwa S, Bonini C, Alcala-Mata L, Wright KL, Gulani V (2016) Multiparametric MR Imaging in Abdominal Malignancies. Magnetic resonance imaging clinics of North America 24(1):157–86.

95. Chilla GS, Tan CH, Xu C, Poh CL (2015) Diffusion weighted magnetic resonance imaging and its recent trend-a survey. Quantitative imaging in medicine and surgery 5(3):407–22.

96. Mannelli L, Nougaret S, Vargas HA, Do RKG (2015) Advances in diffusion-weighted imaging. Radiologic clinics of North America 53(3):569–81.

97. White NS, McDonald C, Farid N, Kuperman J, Karow D, Schenker-Ahmed NM et al. (2014) Diffusion-weighted imaging in cancer: physical foundations and applications of restriction spectrum imaging. Cancer research 74(17):4638–52.

98. Xu Q, Xian J (2015) Role of quantitative magnetic resonance imaging parameters in the evaluation of treatment response in malignant tumors. Chinese medical journal 128(8):1128–33.

99. Li SP, Padhani AR (2012) Tumor response assessments with diffusion and perfusion MRI. Journal of magnetic resonance imaging JMRI 35(4):745–63.

100. Fernandes JL, Rochitte CE (2015) T1 mapping: technique and applications. Magnetic resonance imaging clinics of North America 23(1):25–34.

101. Andreisek G, Weiger M (2014) T2* mapping of articular cartilage: current status of research and first clinical applications. Investigative radiology 49(1):57–62.

102. Canale S, Vilcot L, Ammari S, Lemery M, Bidault F, Balleyguier C et al. (2014) Whole body MRI in paediatric oncology. Diagnostic and interventional imaging 95(6):541–50.

103. Fowler KJ, McConathy J, Narra VR (2014) Whole-body simultaneous positron emission tomography (PET)-MR: optimization and adaptation of MRI sequences. Journal of magnetic resonance imaging JMRI 39(2):259–68.

104. Appenzeller P, Mader C, Huellner MW, Schmidt D, Schmid D, Boss A et al. (2013) PET/CT versus body coil PET/MRI: how low can you go? Insights into imaging 4(4):481–90.

105. Barbosa FdG, Schulthess G von, Veit-Haibach P (2015) Workflow in Simultaneous PET/MRI. Seminars in nuclear medicine 45(4):332–44.

106. Kuhn FP, Hüllner M, Mader CE, Kastrinidis N, Huber GF, Schulthess GK von et al. (2014) Contrast-enhanced PET/MR imaging versus contrast-enhanced PET/CT in head and neck cancer: how much MR information is needed? Journal of Nuclear Medicine 55(4):551–8.

107. Reiner CS, Stolzmann P, Husmann L, Burger IA, Hüllner MW, Schaefer NG et al. (2014) Protocol requirements and diagnostic value of PET/MR imaging for liver metastasis detection. European journal of nuclear medicine and molecular imaging 41(4):649–58.

108. Schulthess GK von, Veit-Haibach P (2014) Workflow Considerations in PET/MR Imaging. Journal of Nuclear Medicine 55(Supplement 2):19S-24S.

109. Buchbender C, Hartung-Knemeyer V, Beiderwellen K, Heusch P, Kühl H, Lauenstein TC et al. (2013) Diffusion-weighted imaging as part of hybrid PET/MRI protocols for whole-body cancer staging: does it benefit lesion detection? European journal of radiology 82(5):877–82.

110. Schaarschmidt BM, Grueneisen J, Heusch P, Gomez B, Beiderwellen K, Ruhlmann V et al. (2015) Oncological whole-body staging in integrated (18)F-FDG PET/MR: Value of different MR sequences for simultaneous PET and MR reading. European journal of radiology 84(7):1285–92.

111. Afshar-Oromieh A, Haberkorn U, Hadaschik B, Habl G, Eder M, Eisenhut M et al. (2013) PET/MRI with a 68Ga-PSMA ligand for the detection of prostate cancer. European journal of nuclear medicine and molecular imaging 40(10):1629–30.

112. Afshar-Oromieh A, Haberkorn U, Schlemmer HP, Fenchel M, Eder M, Eisenhut M et al. (2014) Comparison of PET/CT and PET/MRI hybrid systems using a 68Ga-labelled PSMA ligand for the diagnosis of recurrent prostate cancer: initial experience. European journal of nuclear medicine and molecular imaging 41(5):887–97.

113. Avanesov M, Karul M, Derlin T (2015) (68)Ga-PSMA als neuer Tracer für die Evaluation des Prostatakarzinoms: Vergleich zwischen PET-CT und PET-MRT beim biochemischen Rezidiv. Der Radiologe 55(2):89–91.

114. Afshar-Oromieh A, Malcher A, Eder M, Eisenhut M, Linhart HG, Hadaschik BA et al. (2013) PET imaging with a 68Gagallium-labelled PSMA ligand for the diagnosis of prostate cancer: biodistribution in humans and first evaluation of tumour lesions. European journal of nuclear medicine and molecular imaging 40(4):486–95.

115. Al-Nahhas A, Win Z, Szyszko T, Singh A, Nanni C, Fanti S et al. (2007) Gallium-68 PET: A New Frontier in Receptor Cancer Imaging. Anticancer research 27:4087-4094.

116. Zech CJ, Herrmann KA, Reiser MF, Schoenberg SO (2007) MR Imaging in Patients with Suspected Liver Metastases. Magnetic resonance in medicine 6(1):43–52.

117. Frydrychowicz A, Lubner MG, Brown JJ, Merkle EM, Nagle SK, Rofsky NM et al. (2012) Hepatobiliary MR imaging with gadolinium-based contrast agents. Journal of magnetic resonance imaging JMRI 35(3):492–511.

118. Sirlin CB, Hussain HK, Jonas E, Kanematsu M, Min Lee J, Merkle EM et al. (2014) Consensus report from the 6th International forum for liver MRI using gadoxetic acid. Journal of magnetic resonance imaging JMRI 40(3):516–29.

119. Palmucci S (2014) Focal liver lesions detection and characterization: The advantages of gadoxetic acid-enhanced liver MRI. World journal of hepatology 6(7):477–85.

120. Sattler B, Jochimsen T, Barthel H, Sommerfeld K, Stumpp P, Hoffmann K et al. (2013) Physical and organizational provision for installation, regulatory requirements and implementation of a

simultaneous hybrid PET/MR-imaging system in an integrated research and clinical setting. Magma 26(1):159–71.

121.   Queiroz MA, Hüllner M, Kuhn F, Huber G, Meerwein C, Kollias S et al. (2014) PET/MRI and PET/CT in follow-up of head and neck cancer patients. European journal of nuclear medicine and molecular imaging 41(6):1066–75.

122.   Queiroz MA, Kubik-Huch RA, Hauser N, Freiwald-Chilla B, Schulthess G von, Froehlich JM et al. (2015) PET/MRI and PET/CT in advanced gynaecological tumours: initial experience and comparison. European radiology 25(8):2222–30.

123.   Nagarajah J, Jentzen W, Hartung V, Rosenbaum-Krumme S, Mikat C, Heusner TA et al. (2011) Diagnosis and dosimetry in differentiated thyroid carcinoma using 124I PET: comparison of PET/MRI vs PET/CT of the neck. European journal of nuclear medicine and molecular imaging 38(10):1862–8.

124.   Partovi S, Kohan A, Vercher-Conejero JL, Rubbert C, Margevicius S, Schluchter MD et al. (2014) Qualitative and quantitative performance of ^{18}F-FDG-PET/MRI versus ^{18}F-FDG-PET/CT in patients with head and neck cancer. AJNR. American journal of neuroradiology 35(10):1970–5.

125.   Wetter A, Lipponer C, Nensa F, Heusch P, Rübben H, Altenbernd J et al. (2014) Evaluation of the PET component of simultaneous [(18)F]choline PET/MRI in prostate cancer: comparison with [(18)F]choline PET/CT. European journal of nuclear medicine and molecular imaging 41(1):79–88.

126.   Kohan AA, Kolthammer JA, Vercher-Conejero JL, Rubbert C, Partovi S, Jones R et al. (2013) N staging of lung cancer patients with PET/MRI using a three-segment model attenuation correction algorithm: initial experience. European radiology 23(11):3161–9.

127.   Brendle C, Schwenzer NF, Rempp H, Schmidt H, Pfannenberg C, La Fougère C et al. (2015) Assessment of metastatic colorectal cancer with hybrid imaging: comparison of reading performance using different combinations of anatomical and functional imaging techniques in PET/MRI and PET/CT in a short case series. European journal of nuclear medicine and molecular imaging. doi:10.1007/s00259-015-3137-z.

128.   Schwenzer NF, Schraml C, Müller M, Brendle C, Sauter A, Spengler W et al. (2012) Pulmonary lesion assessment: comparison of whole-body hybrid MR/PET and PET/CT imaging--pilot study. Radiology 264(2):551–8.

129.   Heusch P, Buchbender C, Köhler J, Nensa F, Gauler T, Gomez B et al. (2014) Thoracic staging in lung cancer: prospective comparison of 18F-FDG PET/MR imaging and 18F-FDG PET/CT. Journal of Nuclear Medicine 55(3):373–8.

130.   Kubiessa K, Purz S, Gawlitza M, Kühn A, Fuchs J, Steinhoff KG et al. (2014) Initial clinical results of simultaneous 18F-FDG PET/MRI in comparison to 18F-FDG PET/CT in patients with head and neck cancer. European journal of nuclear medicine and molecular imaging 41(4):639–48.

131.   Bailey DL, Barthel H, Beuthin-Baumann B, Beyer T, Bisdas S, Boellaard R et al. (2014) Combined PET/MR: Where are we now? Summary report of the second international workshop on PET/MR imaging April 8-12, 2013, Tubingen, Germany. Molecular imaging and biology 16(3):295–310.

132.   Punwani S, Taylor SA, Saad ZZ, Bainbridge A, Groves A, Daw S et al. (2013) Diffusion-weighted MRI of lymphoma: prognostic utility and implications for PET/MRI? European journal of nuclear medicine and molecular imaging 40(3):373–85.

133.   Bailey DL, Antoch G, Bartenstein P, Barthel H, Beer AJ, Bisdas S et al. (2015) Combined PET/MR: The Real Work Has Just Started. Summary Report of the Third International Workshop on PET/MR Imaging; February 17-21, 2014, Tübingen, Germany. Molecular imaging and biology 17(3):297–312.

134. Bailey DL, Pichler BJ, Gückel B, Barthel H, Beer AJ, Bremerich J et al. (2015) Combined PET/MRI: Multi-modality Multi-parametric Imaging Is Here: Summary Report of the 4th International Workshop on PET/MR Imaging; February 23-27, 2015, Tübingen, Germany. Molecular imaging and biology 17(5):595–608.

135. Gawlitza M, Purz S, Kubiessa K, Boehm A, Barthel H, Kluge R et al. (2015) In Vivo Correlation of Glucose Metabolism, Cell Density and Microcirculatory Parameters in Patients with Head and Neck Cancer: Initial Results Using Simultaneous PET/MRI. PloS one 10(8):e0134749.

136. Choi BB, Kim SH, Kang BJ, Lee JH, Song BJ, Jeong SH et al. (2012) Diffusion-weighted imaging and FDG PET/CT: predicting the prognoses with apparent diffusion coefficient values and maximum standardized uptake values in patients with invasive ductal carcinoma. World journal of surgical oncology 10:126.

137. Varoquaux A, Rager O, Lovblad K, Masterson K, Dulguerov P, Ratib O et al. (2013) Functional imaging of head and neck squamous cell carcinoma with diffusion-weighted MRI and FDG PET/CT: quantitative analysis of ADC and SUV. European journal of nuclear medicine and molecular imaging 40(6):842–52.

138. Nakajo M, Nakajo M, Kajiya Y, Tani A, Kamiyama T, Yonekura R et al. (2012) FDG PET/CT and diffusion-weighted imaging of head and neck squamous cell carcinoma: comparison of prognostic significance between primary tumor standardized uptake value and apparent diffusion coefficient. Clinical nuclear medicine 37(5):475–80.

139. Grueneisen J, Beiderwellen K, Heusch P, Buderath P, Aktas B, Gratz M et al. (2014) Correlation of standardized uptake value and apparent diffusion coefficient in integrated whole-body PET/MRI of primary and recurrent cervical cancer. PloS one 9(5):e96751.

140. Brandmaier P, Purz S, Bremicker K, Höckel M, Barthel H, Kluge R et al. (2015) Simultaneous [18F]FDG-PET/MRI: Correlation of Apparent Diffusion Coefficient (ADC) and Standardized Uptake Value (SUV) in Primary and Recurrent Cervical Cancer. PloS one 10(11):e0141684.

141. Surov A, Stumpp P, Meyer HJ, Gawlitza M, Höhn A, Boehm A et al. (2016) Simultaneous 18F-FDG-PET/MRI: Associations between diffusion, glucose metabolism and histopathological parameters in patients with head and neck squamous cell carcinoma. Oral oncology 58:14–20.

142. Spick C, Herrmann K, Czernin J (2016) 18F-FDG PET/CT and PET/MRI Perform Equally Well in Cancer: Evidence from Studies on More Than 2,300 Patients. Journal of Nuclear Medicine 57(3):420–30.

143. Stumpp P, Purz S, Sabri O, Kahn T (2016) Molekulare Bildgebung bei Kopf-Hals-Tumoren: Perspektiven der PET-MRT. Der Radiologe. doi:10.1007/s00117-016-0125-7.

5. Erklärung über die eigenständige Anfertigung der Arbeit und Kenntlichmachung der benutzten Hilfsmittel bzw. Hilfen

Hiermit erkläre ich, die vorliegende Habilitationsschrift selbstständig und ohne unerlaubte fremde Hilfe angefertigt zu haben. Ich habe keine anderen als die im Literaturverzeichnis angeführten Quellen benutzt und sämtliche Textstellen, die wörtlich oder sinngemäß aus veröffentlichten oder unveröffentlichten Schriften entnommen wurden, als solche kenntlich gemacht. Ebenfalls sind alle von anderen Personen bereitgestellten Materialien oder erbrachten Dienstleistungen als solche gekennzeichnet.

Leipzig, den 01.06.2016

Dr. med. Patrick Stumpp

6. Lebenslauf

Dr. med. Patrick Stumpp, MME

Geburtsdatum: 31.08.1973
Geburtsort: Ravensburg

Beruflicher Werdegang
Seit 04/2011   Strahlenschutzbeauftragter
Seit 09/2011   Leitung der Hybridbildgebung (PET/CT und PET/MRT)
Seit 12/2008   Oberarzt mit Verantwortungsbereich CT und MRT
Seit 06/2005   Facharzt für Diagnostische Radiologie, Universität Leipzig
06/2001 – 05/2005   AiW an der Klinik für Diagnostische und Interventionelle Radiologie, Universität Leipzig, davon
06/2003 – 05/2004   Klinisches Jahr in der Klinik und Poliklinik für Strahlentherapie, Universität Leipzig
12/1999 – 05/2001   AiP an der Klinik für Diagnostische Radiologie, Universität Leipzig

Studium
10/2005 – 10/2007   Postgraduales, berufsbegleitendes Aufbaustudium zum Master of Medical Education an der Universität Heidelberg (Verleihung des Masters 2010)
10/1999   3. Staatsexamen (Note 1,6)
10/1993 – 10/1999   Studium der Humanmedizin an der Universität Leipzig, davon
    10/1998 – 2/1999 PJ Innere Medizin in Melbourne, Australien
    8-9/1997 Famulatur Innere Medizin in Inverness, Schottland
    10/1996 Famulatur Radiologie in Augusta, Georgia, USA

Preise
05/2009   Posterpreis der Deutschen Röntgengesellschaft
10/1998   Wolfgang-Natonek-Preis des Vereins der Freunde und Förderer der Universität Leipzig

Promotion
05/2003   „Anwendung von hepatobiliärem Kontrastmittel im Spiral-CT bei Patienten nach Whipple-OP zur verbesserten Darstellung der zuführenden Darmschlinge" Universität Leipzig

Lehre
Seit 11/2010   Prüfer im 2. Medizinischen Staatsexamen
Seit 10/2008   Lehrbeauftragter der Klinik und Poliklinik für Diagnostische und Interventionelle Radiologie
Seit 2003   Dozent beim Leipziger Hochschullehrertraining
Seit 2003   Tutor im Rahmen der POL-Kurse
Seit 2000   Regelmäßige Seminarleitung im Rahmen der Kurse Radiologie / QSB
11
1996 - 2013   Mitglied der Studienkommission

Mitgliedschaften
Deutsche Röntgengesellschaft
Deutsche Gesellschaft für interventionelle Radiologie
Sächsische Radiologische Gesellschaft
European Society of Radiology
Ärzte ohne Grenzen
Gesellschaft für Medizinische Ausbildung (GMA)

Leipzig, den 01.06.2016

Dr. med. Patrick Stumpp

7. Danksagung